UNIVERSITY OF LJUBLJANA
FACULTY FOR MATHEMATICS AND PHYSICS

Marko Bračko

Measurement of the forward-backward asymmetry of bottom quarks at the Z^0 Peak

Doctoral Thesis

SUPERVISOR: Prof Dr G Kernel

Ljubljana, 2000

Marko Bračko

Meritev asimetrije naprej-nazaj pri razpadih Z^0 v kvarkovski par $\mathrm{b}\overline{\mathrm{b}}$

Disertacija

Mentor: prof. dr. G. Kernel

Ljubljana, 2000

Drum hab ich mich der Magie ergeben,
Ob mir durch Geistes Kraft und Mund
Nicht manch Geheimnis würde kund;
Daß ich nicht mehr, mit sauerm Schweiß,
Zu sagen brauche, was ich nicht weiß;
Daß ich erkenne, was die Welt
Im innersten zusammenhält,
Schau alle Wirkenskraft und Samen,
Und tu nicht mehr in Worten kramen.

J. W. Goethe: Faust

Znanosti se ne dela, znanost se živi.

Neznani mislec

Statistika je kao bikini - otkriva sve, a pokazuje ništa.

Neimenovani športni komentator TV Beograd

V eksperimentalni fiziki osnovnih delcev je – še bolj kot v drugih vejah znanosti – prisotna potreba po izmenjavi informacij in sodelovanju. Prispevek posameznika se običajno neločljivo prepleta z delom številnih sodelavcev in prispeva zgolj nekaj kamenčkov k ogromnemu mozaiku. Pri sestavljanju le-tega se je v času podiplomskega študija zato nabralo kar precej ljudi, ki bi se jim želel zahvaliti …

Najprej je tu prof. dr. Gabrijel Kernel, ki je zares zavzeto spremljal moje delo in me vodil tudi takrat, kadar sem zašel z začrtane poti. Imel je razumevanje za raziskovalne, a tudi čisto življenjske težave, na katere sem naletel v vseh teh letih. Po pogovorih z njim sem marsikateri fizikalni problem zagledal v čisto drugačni luči.

Tomaž Podobnik je s svojimi pronicljivimi idejami ter pragmatičnim fizikalnim pristopom začrtal osnovne smernice tega doktorskega dela. Kot delovni mentor je spremljal moje napredovanje in kljub izjemno velikemu številu različnih obveznosti uspeval najti čas za moja vprašanja.

Tudi Boštjan Golob, vodja ljubljanske skupine DELPHI, je bil vedno voljan pomagati iz zagat, ki so se pojavljale na moji poti. Njegov prispevek je bil še posebej dobrodošel v času dela v CERN-u.

Vsem trem naštetim se moram zahvaliti tudi za koristne pripombe in doslednost ob prebiranju nastajajočih različic tega dela.

Le kako bi lahko pozabil vse, s katerimi sem delil usodo v tujini. Borut P. Kerševan, Gregor Kramberger in Matevž Tadel so bili samo nekateri od tistih, s katerimi smo v CERN-u, Ženevi in v Cukrarni prebili precej dni in noči ob delu, razmišljanjih in razpravah, v katerih smo poleg fizikalnih rešitev našli tudi nemalo odgovorov na številna splošna vprašanja o življenju, vesolju in sploh vsem …

I would like to express my gratitude to all members of the DELPHI Collaboration for the effort put into the operation of the detector and into the processing of the collected data.

Za prijetno delovno okolje in tovariško vzdušje se moram zahvaliti tudi vsem sodelavcem Odseka za eksperimentalno fiziko osnovnih delcev Instituta Jožef Stefan v Ljubljani, še posebej pa članom ljubljanske skupine DELPHI.

Posebna zahvala gre brez dvoma Suzani, ki mi je stala ob strani in mi odpustila dneve, ki jih nisva preživela skupaj, poleg tega pa ob meni izvedela o fiziki in o osnovnih delcih verjetno mnogo več, kot si je kdajkoli želela … Suzana, hvala ti za vse.

Seveda so mi bili v veliko pomoč v času študija tudi starši in sestra Vanja, ki so z ogromno mero razumevanja sprejemali moje pomanjkanje časa zanje.

Vidu Bobnarju in Gregorju Krambergerju bi se rad zahvalil za številne kave in za zdrav pogled na življenje in znanost. Iskreno sem hvaležen tudi številnim kolegom in znancem, ki v vsem tem času niso pozabili name.

Anki Polajnar gre zahvala, ker je poskrbela, da so iz slovenskega dela disertacije izginile tako pravopisne kot tudi velika večina tipkarskih napak.

Na koncu se moram zahvaliti še Ministrstvu za znanost in tehnologijo, ki je s financiranjem omogočilo izdelavo tega dela, in Odseku za eksperimentalno fiziko osnovnih delcev Instituta Jožef Stefan v Ljubljani za dobre pogoje pri raziskovalnem delu. Posebno zahvalo sem dolžan še Samu Korparju in Fakulteti za kemijo in kemijsko tehnologijo Univerze v Mariboru, da so mi omogočili kar najlaže združiti pedagoško delo z raziskovalnim.

Abstract

   The forward-backward asymmetry of the process $e^+e^- \rightarrow b\bar{b}$ was measured near the Z^0 peak, using about 3 million hadronic Z^0 decays collected with the DELPHI detector at LEP between the years 1992 and 1995. The measurement was performed on an enriched $b\bar{b}$ sample selected by a b-confidence tag, based on track impact parameters and other kinematic variables. The bottom-quark charge was tagged by inclusively produced charged kaons identified mainly by the RICH detectors in the barrel region of the detector. A dilution factor, comprising probabilities for correct charge determination, was extracted from the measured data by using double-tagged events. With this approach, the estimation of purities and efficiencies of the kaon tagging from the simulated data was avoided. The $b\bar{b}$ forward-backward asymmetries, measured at three different centre-of-mass energies, read:

$$A_{FB}^{b\bar{b}}(89.43~\text{GeV}) = 0.043 \pm 0.033_{\text{stat}} \pm 0.005_{\text{syst}}\,,$$
$$A_{FB}^{b\bar{b}}(91.24~\text{GeV}) = 0.108 \pm 0.010_{\text{stat}} \pm 0.007_{\text{syst}}\,,$$
$$A_{FB}^{b\bar{b}}(92.99~\text{GeV}) = 0.102 \pm 0.035_{\text{stat}} \pm 0.017_{\text{syst}}\,.$$

Combining the three results within the framework of the Standard Model, the bottom-quark pole asymmetry was determined to be:

$$A_{FB}^{0,b\bar{b}} = 0.1068 \pm 0.0089_{\text{stat}} \pm 0.0064_{\text{syst}}\,,$$

yielding the following value of the effective electroweak mixing angle for leptons:

$$\sin^2\theta_{\text{eff}}^{\text{lept}} = 0.2308 \pm 0.0020\,.$$

Keywords:
Standard Model, forward-backward asymmetry, effective lepton mixing angle, $b\bar{b}$ quark pairs, quark-charge tagging, charged kaons, LEP, DELPHI

PACS:
12.15.-y Electroweak interactions
12.15.Ji Applications of electroweak models to specific processes
12.15.Mm Neutral currents
13.65.+i Hadron production by electron-positron collisions
14.65.Fy Bottom quarks
14.70.Hp Z bosons

Izvleček

Asimetrijo naprej-nazaj pri reakciji $\mathrm{e^+e^-} \to \mathrm{b\overline{b}}$ smo merili v bližini težiščne energije bozona $\mathrm{Z^0}$, na vzorcu, ki ga je sestavljalo približno 3 milijone hadronskih razpadov bozona $\mathrm{Z^0}$. Meritve so bile opravljene na podatkih, zbranih med letoma 1992 in 1995 z detektorjem DELPHI, ki je bil postavljen ob elektronsko-pozitronskem pospeševalniku LEP. Izmerjeni vzorec je vseboval visok delež razpadov $\mathrm{Z^0} \to \mathrm{b\overline{b}}$, izbranih na podlagi vpadnih parametrov in ostalih kinematičnih spremenljivk nastalih delcev. Na naboj kvarka b smo sklepali iz naboja nabitih kaonov, ki so nastali v okviru razpadne verige začetnega kvarka. Nabite kaone, uporabljene za označevanje naboja, smo izmerili v centralnem cilindričnem delu detektorja DELPHI. Za identifikacijo smo uporabili predvsem detektor Čerenkovega sevanja. Faktor, ki pove, kako učinkovita je metoda označevanja naboja kvarkov, smo določili iz izmerjenega vzorca dogodkov, v katerih smo izbrali dva nabita kaona v nasprotnih polovicah detektorja. Na ta način smo se izognili ocenam čistosti in izkoristkov kaonskega označevanja na računalniško simuliranih podatkih. Pri treh vrednostih težiščne energije $\mathrm{e^+e^-}$ smo za asimetrijo naprej-nazaj dobili naslednje rezultate:

$$A_{FB}^{\mathrm{b\overline{b}}}(89,43~\mathrm{GeV}) = 0,043 \pm 0,033_{\mathrm{stat}} \pm 0,005_{\mathrm{sist}}\,,$$
$$A_{FB}^{\mathrm{b\overline{b}}}(91,24~\mathrm{GeV}) = 0,108 \pm 0,010_{\mathrm{stat}} \pm 0,007_{\mathrm{sist}}\,,$$
$$A_{FB}^{\mathrm{b\overline{b}}}(92,99~\mathrm{GeV}) = 0,102 \pm 0,035_{\mathrm{stat}} \pm 0,017_{\mathrm{sist}}\,.$$

Ob upoštevanju predpostavk standardnega modela smo vse tri meritve združili, iz izračunane asimetrije na polu $\mathrm{Z^0}$:

$$A_{FB}^{0,\mathrm{b\overline{b}}} = 0,1068 \pm 0,0089_{\mathrm{stat}} \pm 0,0064_{\mathrm{sist}}$$

pa smo izluščili vrednost efektivnega kota elektrošibkega mešanja za leptone:

$$\sin^2 \theta_{\mathrm{eff}}^{\mathrm{lept}} = 0,2308 \pm 0,0020\,.$$

Ključne besede:
standardni model, asimetrija naprej-nazaj, efektivni leptonski mešalni kot, kvarkovski pari $\mathrm{b\overline{b}}$, označevanje naboja kvarkov, nabiti kaoni, LEP, DELPHI

Contents

<center>━━━━━━━━━━ **1** ━━━━━━━━━━</center>

Introduction

A forward-backward asymmetry, $A_{FB}^{f\bar{f}}$, is characteristic for all different $f\bar{f}$ pairs produced in electron-positron annihilation. The asymmetry is manifested as a difference in angular distributions for fermions and antifermions: while the former fly more often in one direction with respect to the incoming electrons, the latter are more common products in the opposite direction. In the Standard Model of the electroweak interactions [1–3], the asymmetry is accounted for by different couplings of *weak neutral current* to particles of left and right chirality. The asymmetry, expected to vanish in case of pure electromagnetic processes, is thus a direct consequence of the parity violation, inherent in the weak interactions [4].

For the time being, the Standard Model of the electroweak and strong interactions is the most complete theory of elementary particles and interactions between them. The theory contains 18 independent parameters, that have to be determined from the measurements. Although a self-consistency of the Standard Model is confirmed by various experimental tests of its predictions, there is still one parameter which is completely unknown: the mass of the hypothetical Higgs boson. In spite of unsuccessful attempts to observe this particle up to now, it is, however, possible to set limits on its mass through the indirect estimates, exploiting radiative corrections to various processes. Such corrections include also exchanges of the virtual Higgs bosons. Precise measurements of the forward-backward asymmetries can be used for this purpose (see Figure 1.1).

Forward-backward asymmetries for different lepton and quark pairs have already been measured at the Large Electron-Positron Collider, LEP. For e^+e^- energies near the Z^0 pole, the asymmetries for quarks are more pronounced than for leptons in the final state. It is therefore advantageous to measure quark asymmetries, although the original quark charge is veiled by fragmentation and hadronisation processes. Charges of original quarks have to be determined from the final-state particles and various methods have so far been developed for this purpose. The thesis describes a measurement of the forward-backward asymmetry of bottom quarks, with the quark charge tagged by charged kaons produced inclusively in the b-quark decay chain. The tagging method of the bottom-quark charge is possible due to unique hadron identification capabilities of the DELPHI detector.

The composition of the present work is as follows. The theoretical background and the

<center>1</center>

Preliminary

$A_{fb}^{0,l}$ 0.23099 ± 0.00053

A_τ 0.23192 ± 0.00053

A_e 0.23117 ± 0.00061

$A_{fb}^{0,b}$ 0.23225 ± 0.00036

$A_{fb}^{0,c}$ 0.23262 ± 0.00082

$<Q_{fb}>$ 0.2321 ± 0.0010

Average(LEP)   0.23184 ± 0.00023
χ^2/d.o.f.: 5.7 / 5

A_l(SLD)   0.23098 ± 0.00026

Average(LEP+SLD)   0.23146 ± 0.00017
χ^2/d.o.f.: 11.9 / 6

M_H [GeV]

10^3

10^2

$\Delta\alpha_{had}^{(5)}$= 0.02804 ± 0.00065
α_s= 0.119 ± 0.002
m_t= 174.3 ± 5.1 GeV

0.23   0.232   0.234
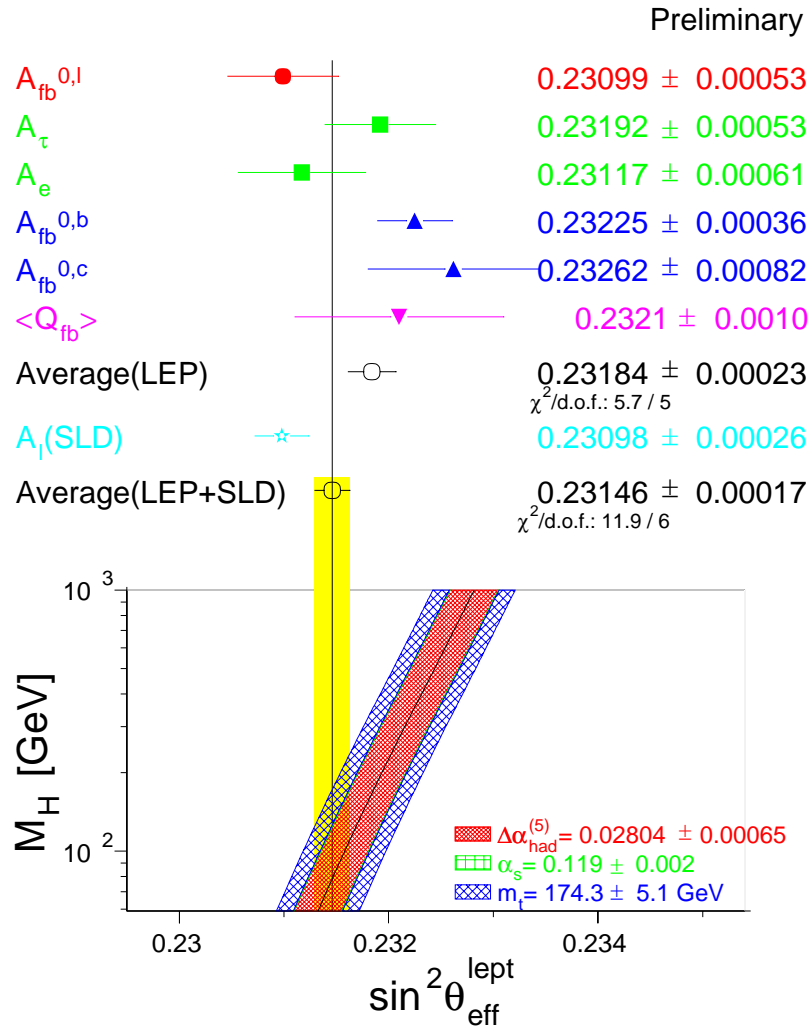
$\sin^2\theta_{eff}^{lept}$

Figure 1.1 : The effective electroweak mixing angle for leptons, $\sin^2\theta_{eff}^{lept}$, as determined from the measured fermion-pair asymmetries [5]. The Standard Model prediction as a function of M_H is also shown (hatched band). The precision of the calculation is determined by the uncertainties on other parameters of the Standard Model.

charge tagging technique are explained in Chapter 2. Chapter 3 provides the necessary information about the experimental setup: the electron-positron collider, the particle detector and its performance are described in a brief way. The selection of the data sample is described in Chapter 4, while the analysis of the selected data is presented in the next chapter. Chapter 5 also includes a discussion about systematic errors. In Chapter 6 the results are listed, combined and compared to the results of previous measurements. Short summery of the thesis in slovene language is added as Chapter 7. Appendices contain derivations of equations used throughout the thesis and a collection of figures illustrating various measured quantities for different data sets.

<div align="center">

2

Theoretical background

</div>

2.1 Standard Model of electroweak interactions in brief

The Standard Model (SM) is a *quantum field theory* describing properties of elementary building blocks of matter and interactions among them. So far, the predictions of the SM have always been in agreement with experimental observations at all available energies, i.e. up to approximately 200 GeV. This makes the model currently the most widely accepted theory in high energy physics.

Quantised fields are used to describe all elementary particles incorporated in the theory. Different fields are combined in the Lagrangian density $\mathcal{L}(x)$, a function of a 4-dimensional space-time x. The Euler-Lagrange equations of motion describing the dynamics for a particular field $\Psi(x)$ are then obtained as:

$$\partial_\mu \left(\frac{\partial \mathcal{L}}{\partial(\partial_\mu \Psi)} \right) - \frac{\partial \mathcal{L}}{\partial \Psi} = 0 \,. \tag{2.1}$$

The main principle of the Standard Model as a *gauge theory* is the invariance of the Lagrangian under gauge transformations. These transformations form different symmetry groups corresponding to different interactions. All the groups are unitary, with continuously varying parameters that determine specific transformations. It turns out that the gauge invariance of $\mathcal{L}$ automatically ensures the renormalizability of the theory [6]. The second important principle the theory is based upon is the *spontaneous symmetry breakdown* mechanism used for the generation of particle masses [7].

The Standard Model that incorporates the above principles is based on the symmetry group $SU(3)_c \times SU(2)_L \times U(1)_Y$. It includes two sub-theories:

- Electroweak theory, describing electromagnetic and weak interactions, combines them through the symmetry group $SU(2)_L \times U(1)_Y$, where L stands for the *left chirality* and Y stands for the *hypercharge*. Up to the currently achievable energies the theory is perfectly perturbative and thus calculable with the Feynman-diagram approach.

- Quantum Chromodynamics (QCD) as the theory of the strong interactions. The symmetry group used here is $SU(3)_c$, where the index c denotes the *colour*. This theory imposes

<div align="center">3</div>

problems for low energy calculations, where the strong coupling constant increases. In such cases, calculations have to be performed using various non-perturbative techniques.

Only the basic concepts of the electroweak theory will be outlined in this chapter, while more thorough overview of the Standard Model and of its sub-theories can be found in several textbooks, e.g. [8–12].
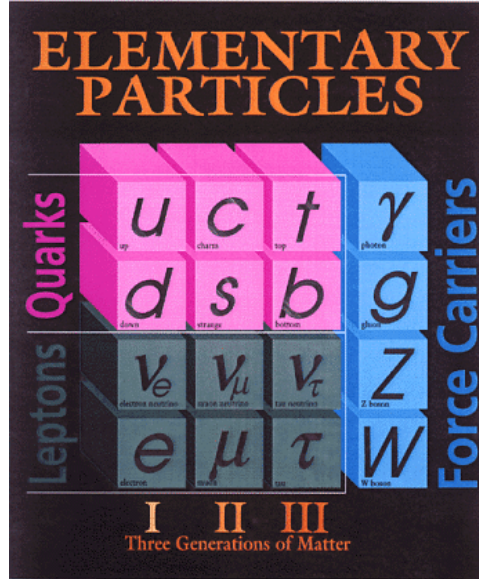
Figure 2.1 : Elementary particles incorporated in the Standard Model.

Particles within the SM

Elementary particles (see Figure 2.1) can be divided into *fermions* of spin $\frac{1}{2}$ and *bosons* of integral-spin value. Fermions are assumed to be the building blocks of matter and are of two types: *leptons*, which can be observed free, and *quarks*, which are always bound within hadrons. Each of these fermions has an anti-fermion partner with the conjugate quantum numbers. Elementary fermions come in three generations:

$$
\begin{bmatrix} \nu_e \\ e \\ u \\ d \end{bmatrix}, \quad
\begin{bmatrix} \nu_\mu \\ \mu \\ c \\ s \end{bmatrix} \quad \text{and} \quad
\begin{bmatrix} \nu_\tau \\ \tau \\ t \\ b \end{bmatrix}, \quad\quad (2.2)
$$

where the second and the third generation are copies of the first one, with same charges, but larger masses.

Elementary bosons incorporated into the theory are mediators of the interactions between the elementary fermions. Four types of interactions are known so far, namely: the *electromagnetic* interactions, the *weak* interactions, the *strong* interactions and the *gravitation*. An incorporation of the gravitation into a global theory has yet to come, but since its coupling constant

Interactions	Bosons	EM charge	Mass [GeV]
Weak	W^+	$+1$	80.419 ± 0.056
	W^-	-1	
	Z^0	0	91.1882 ± 0.0022
Electromagnetic	γ	0	0
Strong	g	0	0

Table 2.1 : List of interactions included in the Standard Model and the mediating bosons. Charges of these particles are shown together with their masses, taken from the reference [13].

is at least 20 orders of magnitude smaller than the coupling constants of other interactions, the SM works well including only the first three interactions mentioned above. The weak interactions are believed to be mediated by the massive *weak bosons* W^+, W^- and Z^0, while massless *photons* and *gluons* are carriers of the electromagnetic and strong interactions, respectively. All these bosons have spin 1 and are listed in Table 2.1, together with their charges[1] and masses[2].

There are two aspects of the association of a certain symmetry group to the gauge theory. The first one associates the number of group generators to the number of gauge bosons responsible for mediating the interactions. There are altogether twelve generators of the group product $SU(3)_c \times SU(2)_L \times U(1)_Y$ and they correspond to gauge bosons, responsible for all three interactions: eight gluons for the $SU(3)_c$ group of the strong interactions and other four bosons, $W^\pm$, Z^0 and γ, for the electroweak $SU(2)_L \times U(1)_Y$ group. The second group aspect of the gauge theory can be expressed through the demand that all fermions are arranged into multiplets forming the representations of a given symmetry group. In the case of the Standard Model symmetry group, each fermion family contains 15 particles, eigenstates of chirality. These states are obtained by chirality projectors $P_{L,R} = \frac{1}{2}(1 \mp \gamma^5)$. The left-handed states then form $SU(2)$-doublets, while the right-handed particles are singlets with respect to $SU(2)$ symmetry. Each of these $SU(2)$-multiplets has a different value of hypercharge Y, as a consequence of the $U(1)_Y$ symmetry. Finally, due to the direct product with the $SU(3)_c$ group, these $SU(2)_L \times U(1)_Y$ fermion multiplets are further recognized also as $SU(3)_c$-singlets in the case of leptons and $SU(3)_c$-triplets in the case of three quark representations. In this way, the total number of fifteen particles is obtained for each family. All of these particles with the corresponding quantum numbers are shown in Table 2.2.

2.1.1 Electroweak interactions

The electroweak sub-sector of the Standard Model is the Glashow-Weinberg-Salam model [1] for leptons, extended to the hadronic sector [2] by incorporating the idea of Cabibbo mixing [3]. The fields present in the electroweak sector of the Standard Model are elementary fermion fields,

---

[1]The charges of particles are expressed in units of the elementary charge, e_0.
[2]Units $\hbar = c = 1$ are used throughout the thesis.

	Fermions			$SU(3)_c$-dim.	q_f	I_W	I_W^3	Y
Leptons	$\begin{pmatrix}\nu_e\\e^-\end{pmatrix}_L$	$\begin{pmatrix}\nu_\mu\\\mu^-\end{pmatrix}_L$	$\begin{pmatrix}\nu_\tau\\\tau^-\end{pmatrix}_L$	1	$\begin{matrix}0\\-1\end{matrix}$	1/2	$\begin{matrix}+1/2\\-1/2\end{matrix}$	-1
	e_R^-	μ_R^-	τ_R^-	1	-1	0	0	-2
Quarks	$\begin{pmatrix}u\\d\end{pmatrix}_L$	$\begin{pmatrix}c\\s\end{pmatrix}_L$	$\begin{pmatrix}t\\b\end{pmatrix}_L$	3	$\begin{matrix}+2/3\\-1/3\end{matrix}$	1/2	$\begin{matrix}+1/2\\-1/2\end{matrix}$	$1/3$
	u_R	c_R	t_R	3	$+2/3$	0	0	$+4/3$
	d_R	s_R	b_R	3	$-1/3$	0	0	$-2/3$

Table 2.2 : List of fermions, grouped into multiplets of the $SU(2)_L \times U(1)_Y$ symmetry group of the combined electroweak interaction. The chirality of the states is denoted by L and R. The dimension of the multiplets according to the $SU(3)_c$ group of the strong interactions is also written. Fermionic quantum numbers given in the table are: the EM charges q_f expressed in the units of elementary charge e_0, the weak isospin I_W with its third component I_W^3 and values of the hypercharge Y. Note that these quantum numbers are connected through the Gell-Mann-Nishijima relation: $q = I_W^3 + \frac{Y}{2}$.

four gauge vector fields and a Higgs field, needed for the generation of masses of elementary particles without destroying the gauge symmetry and renormalizability of the theory.

EW interactions between fermions are introduced by a replacement of the derivative ∂_μ by the covariant derivative D_μ in the Lagrangian describing non-interacting fields. The covariant derivative is constructed as a sum of the $SU(2)$ and $U(1)$ parts:

$$\partial_\mu \to D_\mu = \partial_\mu - ig\frac{\boldsymbol{\tau}}{2} \cdot \boldsymbol{\mathcal{W}}_\mu - ig'\frac{Y}{2}\mathcal{B}_\mu \,, \tag{2.3}$$

where $\boldsymbol{\tau}$ is a vector of the three 2×2 Pauli matrices and Y is the hypercharge. $\mathcal{B}_\mu$ is a $U(1)$-gauge field, while three $SU(2)$-gauge fields are written in the form of a 3-dimensional $SU(2)$-vector $\boldsymbol{\mathcal{W}}_\mu$. Symbols g and g' denote coupling constants of the fields $\mathcal{B}_\mu$ and $\boldsymbol{\mathcal{W}}_\mu$, respectively.

The total electroweak Lagrangian can be written as a sum of three terms:

$$\mathcal{L}_{\mathrm{EW}} = \mathcal{L}_{\mathrm{YM}} + \mathcal{L}_{\mathrm{Higgs}} + \mathcal{L}_{\mathrm{ferm}} \,, \tag{2.4}$$

where each of these terms is constructed in a gauge-invariant form. The first term is the Yang-Mills Lagrangian:

$$\mathcal{L}_{\mathrm{YM}} = -\frac{1}{4}\boldsymbol{\mathcal{W}}_{\mu\nu} \cdot \boldsymbol{\mathcal{W}}^{\mu\nu} - \frac{1}{4}\mathcal{B}_{\mu\nu}\mathcal{B}^{\mu\nu} \,, \tag{2.5}$$

where the field-strength tensors are given as:

$$\boldsymbol{\mathcal{W}}_{\mu\nu} = \partial_\mu\boldsymbol{\mathcal{W}}_\nu - \partial_\nu\boldsymbol{\mathcal{W}}_\mu + g\boldsymbol{\mathcal{W}}_\mu \times \boldsymbol{\mathcal{W}}_\nu \,, \quad \mathcal{B}_{\mu\nu} = \partial_\mu\mathcal{B}_\nu - \partial_\nu\mathcal{B}_\mu \,. \tag{2.6}$$

The term (2.5) includes kinetic and self-interaction terms for the massless gauge bosons. The self-interaction terms, present in the field-strength tensors $\mathcal{W}_{\mu\nu}$, are a consequence of the non-Abelian, i.e. Yang-Mills, nature of the gauge bosons. These terms give rise to triple and quadruple couplings of gauge bosons, which were tested directly at the LEP2 collider (see e.g. [14]). The general expression (2.5), written in the form where the gauge symmetry is transparent, can be rewritten in the form with the observed fields of weak and electromagnetic interactions. This is done by performing the following transformation:

$$\begin{pmatrix} W_\mu^+ \\ W_\mu^- \end{pmatrix} = \begin{pmatrix} 1/\sqrt{2} & -i/\sqrt{2} \\ i/\sqrt{2} & 1/\sqrt{2} \end{pmatrix} \begin{pmatrix} \mathcal{W}_\mu^1 \\ \mathcal{W}_\mu^2 \end{pmatrix} \quad \text{and} \quad \begin{pmatrix} Z_\mu \\ A_\mu \end{pmatrix} = \begin{pmatrix} \cos\theta_W & -\sin\theta_W \\ \sin\theta_W & \cos\theta_W \end{pmatrix} \begin{pmatrix} \mathcal{W}_\mu^3 \\ \mathcal{B}_\mu \end{pmatrix},$$

$$(2.7)$$

where θ_W is the Weinberg mixing angle. Note that the described transformation neither changes the physical content of the Lagrangian (2.5) nor breaks its symmetry under gauge transformations.

Masses of the gauge bosons of the electroweak sector of the SM are generated in a gauge invariant manner by adding the Higgs term $\mathcal{L}_{\text{Higgs}}$ to the Lagrangian:

$$\mathcal{L}_{\text{Higgs}} = (D_\mu\Phi)^\dagger (D^\mu\Phi) - V(\Phi), \tag{2.8}$$

where the covariant derivative D_μ is given in (2.3). The second term in the right-hand side of the above Lagrangian is the Higgs potential:

$$V(\Phi) = \frac{M_{\text{H}}^2}{2} \left[-\Phi^\dagger\Phi + \frac{1}{v^2}(\Phi^\dagger\Phi)^2 \right], \tag{2.9}$$

with a well-known shape of a bottom of a wine bottle. In the minimal realization of the SM, the Higgs field is chosen to be a $SU(2)$-doublet composed of complex scalar fields:

$$\Phi = \begin{pmatrix} \Phi^+ \\ \Phi^0 \end{pmatrix} = \frac{1}{\sqrt{2}} \begin{pmatrix} \Phi_1 + i\Phi_2 \\ \Phi_3 + i\Phi_4 \end{pmatrix}. \tag{2.10}$$

The spontaneous symmetry breakdown occurs due to the minimum of the Higgs potential which is not $SU(2)$-invariant:

$$\Phi_{\text{vac}} = \langle 0|\Phi|0\rangle = \frac{1}{\sqrt{2}} \begin{pmatrix} 0 \\ v \end{pmatrix} \tag{2.11}$$

with v being the so-called *vacuum expectation value* of the Higgs field Φ. In the unitary gauge, three of the four real scalar fields $\Phi_1, ..., \Phi_4$ in (2.10) are used for the longitudinal polarizations of the three gauge bosons, so that the excitations of the scalar field around the vacuum (2.11) are parameterised in the following form:

$$\Phi(x) = \Phi_{\text{vac}} + \Phi'(x) = \frac{1}{\sqrt{2}} \begin{pmatrix} 0 \\ v + H(x) \end{pmatrix}, \tag{2.12}$$

where $H(x)$ is now the only real scalar field left. It is interpreted as the Standard Model *Higgs boson*.

The mass terms for weak gauge bosons are then provided by those parts of the kinetic term in (2.8) that contain the vacuum expectation value:

$$
\begin{aligned}
(D_\mu \Phi_{\text{vac}})^\dagger (D^\mu \Phi_{\text{vac}}) =& \Phi_{\text{vac}}^T \left(g\frac{\boldsymbol{\tau}}{2} \cdot \boldsymbol{\mathcal{W}}_\mu + g'\frac{Y}{2}\mathcal{B}_\mu \right) \left(g\frac{\boldsymbol{\tau}}{2} \cdot \boldsymbol{\mathcal{W}}^\mu + g'\frac{Y}{2}\mathcal{B}^\mu \right) \Phi_{\text{vac}} \\
=& \frac{g^2 v^2}{8} \left(\mathcal{W}_\mu^1 \mathcal{W}^{1\mu} + \mathcal{W}_\mu^2 \mathcal{W}^{2\mu} + \left[g\mathcal{W}_\mu^3 - g'\mathcal{B}_\mu \right]\left[g\mathcal{W}^{3\mu} - g'\mathcal{B}^\mu \right] \right) \quad (2.13) \\
=& \frac{g^2 v^2}{4} \left(W_\mu^+ W^{-\mu} + \frac{1}{2\cos^2\theta_W} Z_\mu Z^\mu \right) .
\end{aligned}
$$

The last row is written in terms of the physical fields $W_\mu^\pm$ and Z_μ given in eq. (2.7), while the ratio of the coupling constants g and g' is expressed by the *weak mixing angle* θ_W as $1 + (g'/g)^2 = 1/\cos^2\theta_W$. Factor $g^2v^2/4$ in equation (2.13) is closely connected to the masses of the gauge bosons $W^\pm$ and Z^0,

$$
M_{\text{W}} = \frac{gv}{2} \quad \text{and} \quad M_{\text{Z}} = \frac{gv}{2\cos\theta_W} = \frac{M_{\text{W}}}{\cos\theta_W} , \tag{2.14}
$$

while for the photons

$$
M_\gamma = 0 . \tag{2.15}
$$

Just to give an impression of the scale, the vacuum expectation value v of the Higgs field is determined to be

$$
v = \frac{2M_{\text{W}}}{g} = \frac{1}{\left(\sqrt{2}G_F \right)^{1/2}} \approx 246 \text{ GeV} ,
$$

where the value $G_F = 1.16639 \cdot 10^{-5}$ GeV^{-2} of the Fermi constant G_F was used [13].

Apart from the mass of the Higgs boson, all parameters used in the construction of the Lagrangian of the SM are determined by independent measurements. Mass of the Higgs boson, M_{H}, used in the parameterisation of the Higgs potential (2.9), is therefore the only unknown parameter of the Standard Model. Despite of the fact that it has not been measured directly so far, certain mass limits can be set by considering the indirect measurements. A few comments on setting such indirect limits will be given at the end of this chapter.

The third term in the electroweak Lagrangian (2.4) describes the fermionic sector of the SM. It is further composed of two terms:

$$
\mathcal{L}_{\text{ferm}} = \mathcal{L}_{\text{Yukawa}} + \mathcal{L}_{\text{kin}} . \tag{2.16}
$$

The first term in (2.16) is the so-called Yukawa term, responsible for the fermion masses through

the Higgs-fermion interactions:

$$
\begin{aligned}
\mathcal{L}_{\text{Yukawa}} =& \mathcal{L}_{\text{Yukawa}}^{\text{lept}} + \mathcal{L}_{\text{Yukawa}}^{\text{quark}} = \\
=& -\frac{\sqrt{2}}{v} \sum_{\ell=\text{e},\mu,\tau} m_\ell \left\{ (\overline{\psi}_{\nu_\ell}, \overline{\psi}_\ell)_L \begin{pmatrix} 0 \\ \frac{v+H}{\sqrt{2}} \end{pmatrix} (\psi_\ell)_R + (\overline{\psi}_\ell)_R \left(0, \frac{v+H}{\sqrt{2}}\right) \begin{pmatrix} \psi_{\nu_\ell} \\ \psi_\ell \end{pmatrix}_L \right\} \\
& - \frac{\sqrt{2}}{v} \sum_{\substack{q_d=\text{d, s, b} \\ q_u=\text{u, c, t}}} \left[m_{q_d} \left\{ (\overline{\psi}_{q_u}, \overline{\psi}_{q_d})_L \begin{pmatrix} 0 \\ \frac{v+H}{\sqrt{2}} \end{pmatrix} (\psi_{q_d})_R + (\overline{\psi}_{q_d})_R \left(0, \frac{v+H}{\sqrt{2}}\right) \begin{pmatrix} \psi_{q_u} \\ \psi_{q_d} \end{pmatrix}_L \right\} \right. \\
& \left. + m_{q_u} \left\{ (\overline{\psi}_{q_u}, \overline{\psi}_{q_d})_L \begin{pmatrix} \frac{v+H}{\sqrt{2}} \\ 0 \end{pmatrix} (\psi_{q_u})_R + (\overline{\psi}_{q_u})_R \left(\frac{v+H}{\sqrt{2}}, 0\right) \begin{pmatrix} \psi_{q_u} \\ \psi_{q_d} \end{pmatrix}_L \right\} \right] \\
=& -\sum_{\ell=\text{e, }\mu,\,\tau} m_\ell\, \overline{\psi}_\ell \psi_\ell \left\{ 1 + \frac{1}{v} H \right\} \quad - \sum_{q=\text{d, u,..., t}} m_q\, \overline{\psi}_q \psi_q \left\{ 1 + \frac{1}{v} H \right\}.
\end{aligned}
$$

$$(2.17)$$

Symbols ψ denote the appropriate fermion fields and $\overline{\psi}$ the corresponding adjoint fields. Couplings of fermions to the Higgs field are proportional to their masses: $g_{\text{Hff}} = \frac{m_{\text{f}}}{v}$. Couplings, however, are quite weak due to the large vacuum expectation value v.

The second term in (2.16) is the kinetic term for the fermions:

$$
\mathcal{L}_{\text{kin}} = \sum_{\text{f}=\ell,\,\text{q}} i\overline{\psi}_{\text{f}} \gamma_\mu D^\mu \psi_{\text{f}}. \tag{2.18}
$$

Due to the covariant derivative (2.3) it includes the terms that describe interactions between fermions and gauge bosons of the electroweak sector of the Standard Model:

$$
\mathcal{L}_{\text{EW}}^{\text{int}} = -g \boldsymbol{\mathcal{W}}_\mu \boldsymbol{\mathcal{J}}^\mu - g' \mathcal{B}_\mu \mathcal{J}_Y^\mu. \tag{2.19}
$$

Here, $\boldsymbol{\mathcal{J}}^\mu$ and $\mathcal{J}_Y^\mu$ are the currents associated to the three generators of the $SU(2)$ group and to the generator of the hypercharge $U(1)$ symmetry group, respectively.

If the expression (2.19) with a transparent gauge symmetry is rewritten in terms of the observed fields of the weak and the electromagnetic interactions, $W_\mu^\pm$, Z_μ and A_μ (see (2.7) again), also the currents have to be rearranged. The so-called charged currents j_{ch}^μ and $j_{\text{ch}}^{\dagger\mu}$ are obtained by the following rotation:

$$
\begin{pmatrix} j_{\text{ch}}^\mu \\ j_{\text{ch}}^{\dagger\mu} \end{pmatrix} = \begin{pmatrix} 1 & i \\ -i & 1 \end{pmatrix} \begin{pmatrix} \mathcal{J}_1^\mu \\ \mathcal{J}_2^\mu \end{pmatrix}. \tag{2.20}
$$

In terms of physical fields and currents, the charged sector of the interaction Lagrangian (2.19) therefore reads:

$$
\mathcal{L}_{\text{EW,charged}}^{\text{int}} = -\frac{g}{\sqrt{2}} \left(W_\mu^+ j_{\text{ch}}^\mu + W_\mu^- j_{\text{ch}}^{\dagger\mu} \right), \tag{2.21}
$$

Explicitly, the charged current j_{ch}^{μ} is given as:

$$j_{\text{ch}}^{\mu} = \sum_{\ell=\text{e},\mu,\tau} \left(\overline{\psi}_{\nu_\ell}, \overline{\psi}_\ell\right)_L \gamma^\mu \tau^+ \begin{pmatrix} \psi_{\nu_\ell} \\ \psi_\ell \end{pmatrix}_L + \sum_{\substack{q'_d=\text{d}',\,\text{s}',\,\text{b}' \\ q_u=\text{u},\,\text{c},\,\text{t}}} \left(\overline{\psi}_{q_u}, \overline{\psi}_{q'_d}\right)_L \gamma^\mu \tau^+ \begin{pmatrix} \psi_{q_u} \\ \psi_{q'_d} \end{pmatrix}_L , \qquad (2.22)$$

with matrices $\tau^\pm = (\tau_1 \pm i\tau_2)/2$ that are linear combinations of the generators τ_1 and τ_2 of the $SU(2)$ group. For the lepton fields, the current contains only terms that correspond to the leptons within the same generation. Contrary to that, terms in the charged current (2.22) containing quark fields, couple also quarks from different generations. Such terms are usually referred to as the *flavour changing currents*. In the SM such currents are a consequence of the fact that the weak eigenstates - fields denoted by primes - do *not* coincide with the fields that describe the mass eigenstates. The two bases are connected via a unitary 3×3 Cabibbo-Kobayashi-Maskawa (CKM) mixing matrix [3]:

$$\begin{pmatrix} \psi_{\text{d}'} \\ \psi_{\text{s}'} \\ \psi_{\text{b}'} \end{pmatrix} = V_{\text{CKM}} \begin{pmatrix} \psi_{\text{d}} \\ \psi_{\text{s}} \\ \psi_{\text{b}} \end{pmatrix} , \qquad (2.23)$$

where

$$V_{\text{CKM}} = \begin{pmatrix} V_{\text{ud}} & V_{\text{us}} & V_{\text{ub}} \\ V_{\text{cd}} & V_{\text{cs}} & V_{\text{cb}} \\ V_{\text{td}} & V_{\text{ts}} & V_{\text{tb}} \end{pmatrix} . \qquad (2.24)$$

The diagonal elements of the CKM matrix are of the order of a unity, which implies that transitions inside quark families are most likely to occur. Transitions between neighbouring families are already much less probable, since $|V_{\text{us}}|$ and $|V_{\text{cd}}|$ are of the order of 0.2, while $|V_{\text{cb}}|$ and $|V_{\text{ts}}|$ are of the order of 0.04. Transitions between the first and the third family are particularly rare, since the values of $|V_{\text{ub}}|$ and $|V_{\text{td}}|$ are less than 0.01.

Turning now to the neutral sector, the two physical currents - the electromagnetic current j_{EM}^{μ} and the weak neutral current j_Z^{μ} - are obtained as linear combinations of the third component $\mathcal{J}_3^{\mu}$ of the current $\mathcal{J}^{\mu}$ and of the current $\mathcal{J}_Y^{\mu}$:

$$j_{EM}^{\mu} = \mathcal{J}_3^{\mu} + \mathcal{J}_Y^{\mu} \qquad (2.25)$$

and

$$j_Z^{\mu} = \cos^2 \theta_W \mathcal{J}_3^{\mu} - \sin^2 \theta_W \mathcal{J}_Y^{\mu} = \mathcal{J}_3^{\mu} - \sin^2 \theta_W j_{EM}^{\mu} . \qquad (2.26)$$

The neutral part of the interaction Lagrangian $\mathcal{L}_{\text{EW,neutral}}^{int}$, written in terms of physical fields and currents, then reads:

$$\mathcal{L}_{\text{EW,neutral}}^{int} = -e_0 A_\mu j_{EM}^{\mu} - \frac{e_0}{\sin \theta_W \cos \theta_W} Z_\mu j_Z^{\mu} , \qquad (2.27)$$

where the coupling constants g and g', the weak mixing angle θ_W and the electron charge magnitude e_0 are related as follows:

$$g' \cos \theta_W = g \sin \theta_W = e_0 . \tag{2.28}$$

Explicitly, the two physical neutral currents are given as:

$$j_{EM}^\mu = \sum_{\mathrm{f}=\ell,q} \overline{\psi}_{\mathrm{f},L} \gamma^\mu q_\mathrm{f} \psi_{\mathrm{f},L} + \sum_{\mathrm{f}=\ell,q} \overline{\psi}_{\mathrm{f},R} \gamma^\mu q_\mathrm{f} \psi_{\mathrm{f},R} \tag{2.29}$$

and

$$j_Z^\mu = \sum_{\ell=\mathrm{e},\mu,\tau} \left(\overline{\psi}_{\nu_\ell}, \overline{\psi}_\ell \right)_L \gamma^\mu \frac{\tau_3}{2} \begin{pmatrix} \psi_{\nu_\ell} \\ \psi_\ell \end{pmatrix}_L + \sum_{\substack{q_d=\mathrm{d,s,b} \\ q_u=\mathrm{u,c,t}}} \left(\overline{\psi}_{q_u}, \overline{\psi}_{q_d} \right)_L \gamma^\mu \frac{\tau_3}{2} \begin{pmatrix} \psi_{q_u} \\ \psi_{q_d} \end{pmatrix}_L$$
$$- \sin^2 \theta_W \sum_{\mathrm{f}=\ell,q} \overline{\psi}_{\mathrm{f},L} \gamma^\mu q_\mathrm{f} \psi_{\mathrm{f},L} - \sin^2 \theta_W \sum_{\mathrm{f}=\ell,q} \overline{\psi}_{\mathrm{f},R} \gamma^\mu q_\mathrm{f} \psi_{\mathrm{f},R} , \tag{2.30}$$

where q_f denotes electric charge of a particular fermion in units of e_0, while

$$\frac{\tau_3}{2} \psi_\mathrm{f} = I_{W,\mathrm{f}}^3 \psi_\mathrm{f} , \tag{2.31}$$

with $I_{W,\mathrm{f}}^3$ being the third component of the weak isospin of the fermion. Contrary to the charged current (2.22), coupling only fermions of left chirality, the two neutral currents couple either two fermions of left chirality or two fermions of right chirality. For the electromagnetic current (2.29), coupling constants for the two chiralities are the same and coincide with e_0 (cf. expression (2.27)). For the weak neutral current, the coupling constants for the two chiralities differ. In terms of the electromagnetic coupling constant they read:

$$c_{Z,L}^\mathrm{f} = -\frac{q_\mathrm{f} \sin^2 \theta_W}{\sin \theta_W \cos \theta_W} ,$$
$$c_{Z,R}^\mathrm{f} = \frac{I_{W,\mathrm{f}}^3 - q_\mathrm{f} \sin^2 \theta_W}{\sin \theta_W \cos \theta_W} . \tag{2.32}$$

Instead of the *left* and the *right* coupling constants, their linear combinations are usually quoted:

$$v_\mathrm{f} = \frac{c_{Z,R}^\mathrm{f} + c_{Z,L}^\mathrm{f}}{2} = \frac{I_{W,\mathrm{f}}^3 - 2q_\mathrm{f} \sin^2 \theta_W}{2 \sin \theta_W \cos \theta_W} ,$$
$$a_\mathrm{f} = \frac{c_{Z,R}^\mathrm{f} - c_{Z,L}^\mathrm{f}}{2} = \frac{I_{W,\mathrm{f}}^3}{2 \sin \theta_W \cos \theta_W} . \tag{2.33}$$

They are referred to as the *vector* and the *axial* coupling constant, respectively. For example, for the b quarks with $I_{W,\mathrm{b}}^3 = -1/2$ and $q_\mathrm{b} = -1/3$, the ratio of the two coupling constants yields approximately

$$\frac{a_\mathrm{b}}{v_\mathrm{b}} = 1.44 , \tag{2.34}$$

if $\sin^2 \theta_W = 0.23$ is assumed. A value of the ratio (2.34) being different from zero accounts for the parity violation in neutral weak processes and directly implies a forward-backward asymmetry of b quarks produced in $\mathrm{e}^+\mathrm{e}^-$ annihilation (see below).

2.2 Physics of e^+e^- annihilation at LEP1
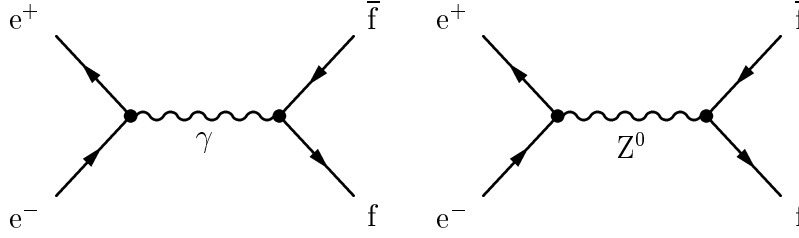
Figure 2.2 : Lowest-order Feynman diagrams for the process $e^+e^- \to f\bar{f}$ (f= ℓ^-, ν_ℓ, q).

The most important physical process at LEP1 energies is the process of electron-positron annihilation into fermion-antifermion pairs: $e^+e^- \to f\bar{f}$, where f= ℓ^-, ν_ℓ, q. For the process of our interest, i.e. when the charged fermion pairs are produced, there are only two annihilation diagrams contributing to the process in the lowest order[3]. These two Feynman diagrams are depicted in Figure 2.2. The amplitudes for the two lowest-order diagrams can be written in the Born approximation:

$$A_\gamma^{\text{Born}} = 4\pi\alpha \; q_e q_f \; \chi_\gamma(s) \cdot \gamma_\mu \otimes \gamma_\mu \,, \tag{2.35}$$

$$
\begin{aligned}
A_Z^{\text{Born}} &= e_0^2 \; \chi_Z^0(s) \cdot \gamma_\mu(v_e - a_e\gamma_5) \otimes \gamma_\mu(v_f - a_f\gamma_5) \\
&= \frac{e_0^2}{4\sin^2\theta_W \cos^2\theta_W} I_{W,e}^3 I_{W,f}^3 \; \chi_Z^0(s) \cdot \\
&\quad \cdot \Big\{ \gamma_\mu(1-\gamma_5) \otimes \gamma_\mu(1-\gamma_5) - 4|q_e|\sin^2\theta_W \; \gamma_\mu \otimes \gamma_\mu(1-\gamma_5) \\
&\qquad - 4|q_f|\sin^2\theta_W \; \gamma_\mu(1-\gamma_5) \otimes \gamma_\mu + 16|q_e q_f|\sin^4\theta_W \; \gamma_\mu \otimes \gamma_\mu \Big\} \,.
\end{aligned}
\tag{2.36}
$$

The symbol $\otimes$ is used for a short notation, e.g. $\gamma_\mu \otimes \gamma_\nu \equiv \overline{v}(p_+)\gamma_\mu u(p_-) \, \overline{u}(q_-)\gamma_\mu v(q_+)$, where $u(p_-)$ and $u(q_-)$ ($v(p_+)$ and $v(q_+)$) denote the spinors of interacting electron (positron) and produced fermion (antifermion). $\chi_\gamma(s)$ and $\chi_Z^0(s)$ refer to the photon and the Z^0 propagator, respectively:

$$\chi_\gamma(s) = \frac{1}{s} \quad \text{and} \quad \chi_Z^0(s) = \frac{1}{s - M_Z^2 + iM_Z\Gamma_Z^0} \,. \tag{2.37}$$

Note, that the width Γ_Z^0 in the latter of the two propagators is energy independent, since the propagator is calculated in the lowest-order Breit-Wigner approximation.

When only the amplitudes (2.35) and (2.36) are used, the differential cross-section for

---

[3]The Bhabha scattering, $e^+e^- \to e^+e^-(\gamma)$, is an exception, because the two annihilation diagrams have to be combined with the two scattering diagrams. It is due to the two scattering diagrams that the cross-section is strongly peaked in the forward direction, i.e. rises above all limits for very small scattering angles.

fermions f produced in the process $e^+e^- \to f\bar{f}$ can be expressed as [15]:

$$\frac{d\sigma_{\text{f,Born}}}{d(\cos\theta)} = 2\pi\frac{\alpha^2}{4s}N_C^{\text{f}}\sqrt{1 - 4\mu_{\text{f}}} \cdot$$
$$\cdot \left[G_1(s)\left(1 + \cos^2\theta\right) + 4\mu_{\text{f}}\,G_2(s)\,\sin^2\theta + 2\sqrt{1 - 4\mu_{\text{f}}}\,G_3(s)\,\cos\theta\right], \tag{2.38}$$

where s is the square of the centre-of-mass energy of an electron and a positron and θ is the polar angle of a fermion f with respect to the direction of the incident e^- as shown in Figure 2.3. The electromagnetic coupling constant is defined as $\alpha = e_0^2/4\pi$, while the symbol N_c^{f} denotes the number of colours (1 in case of leptons and 3 in case of quarks) and $\mu_{\text{f}} = m_{\text{f}}^2/s$. Note that the quoted result is valid for unpolarized beams, used for collisions in LEP.
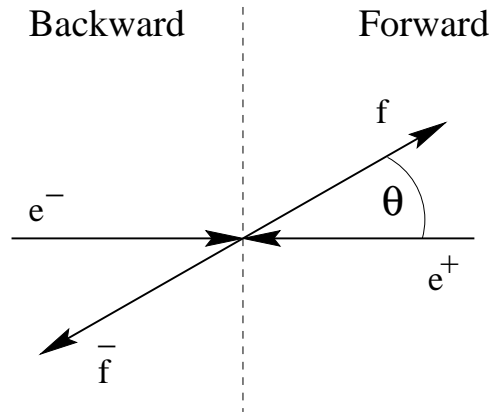
Figure 2.3 : Kinematics for the process $e^+e^- \to f\bar{f}$.

The coefficients dependent on energy in equation (2.38) can be expressed by fermion charges, vector and axial vector coupling constants given in (2.33) and the Z^0 propagator, normalized to the photon propagator:

$$\chi_0(s) = \frac{\chi_Z^0(s)}{\chi_\gamma(s)} = \frac{s}{s - M_Z^2 + iM_Z\Gamma_Z^0}, \tag{2.39}$$

yielding:

$$\begin{aligned}
G_1(s) &= q_e^2 q_f^2 + 2q_e q_f v_e v_f \Re e\chi_0(s) + (v_e^2 + a_e^2)(v_f^2 + a_f^2 - 4\mu_f a_f^2)|\chi_0(s)|^2, \\
G_2(s) &= q_e^2 q_f^2 + 2q_e q_f v_e v_f \Re e\chi_0(s) + (v_e^2 + a_e^2)v_f^2|\chi_0(s)|^2, \\
G_3(s) &= \qquad 2q_e q_f a_e a_f \Re e\chi_0(s) + 4v_e a_e v_f a_f|\chi_0(s)|^2.
\end{aligned} \tag{2.40}$$

A few comments concerning the three terms in square brackets of expression (2.38) should be given here:

- The first forward-backward symmetric term with the $(1 + \cos^2\theta)$ angular dependence includes all three different contributions possible in the lowest order, i.e. a γ-exchange, a Z^0-exchange and a γZ^0-interference. Only the latter two are energy dependent since they contain the Z^0 propagator.

- The second forward-backward symmetric term with the $\sin^2\theta$ angular dependence also includes contributions from the γ-exchange and from the Z^0-exchange as well as an interference of the two. However, even for the heaviest b quark the factor μ_f makes this term much smaller when compared to the term, proportional to G_1.

  Explicitly, when all terms proportional to μ_f are neglected, the fermion differential cross-section (2.38) can be written in the following form:

  $$\frac{d\sigma_f}{d(\cos\theta)} \propto 1 + \cos^2\theta + \frac{8}{3}A_{FB}^{b\overline{b}}(s)\cos\theta\,, \tag{2.41}$$

  where the coefficient $A_{FB}^{b\overline{b}}(s)$ describes the forward-backward asymmetry in the fermion production (see below).

- The third term is forward-backward asymmetric since it is proportional to $\cos\theta$. It contains only contributions from the Z^0-exchange and from the γZ^0-interference, i.e. forward-backward asymmetries vanish in the approximation of a pure γ-exchange.

2.2.1 Forward-backward asymmetry in the lowest order

A quantity called the *forward-backward asymmetry* for the process $e^+e^- \to f\overline{f}$ is defined as:

$$A_{FB}^{f\overline{f}} = \frac{\sigma_F^f - \sigma_B^f}{\sigma_F^f + \sigma_B^f}\,, \tag{2.42}$$

with the cross-sections for fermions f in the forward and the backward direction being defined as:

$$\sigma_F^f = \int\limits_0^1 \frac{d\sigma_f}{d(\cos\theta)}\,d(\cos\theta) \quad \text{and} \quad \sigma_B^f = \int\limits_{-1}^0 \frac{d\sigma_f}{d(\cos\theta)}\,d(\cos\theta)\,. \tag{2.43}$$

Since the *fermion* cross-section in the *forward* direction coincides with the *antifermion* cross-section in the *backward* direction:

$$\sigma_F^f = \int\limits_0^1 \frac{d\sigma_f}{d(\cos\theta)}\,d(\cos\theta) = \int\limits_{-1}^0 \frac{d\sigma_{\overline{f}}}{d(\cos\theta)}\,d(\cos\theta) = \sigma_B^{\overline{f}}\,, \tag{2.44}$$

an equivalent definition of the asymmetry can be given:

$$A_{FB}^{f\overline{f}} = \frac{\sigma_F^f - \sigma_F^{\overline{f}}}{\sigma_F^f + \sigma_F^{\overline{f}}}\,. \tag{2.45}$$

Taking into account the lowest-order expression for the differential cross section (2.38), the forward-backward asymmetry reads:

$$A_{FB}^{f\overline{f}}(s; \text{Born}) = \frac{3}{4}\frac{G_3(s)}{G_1(s) + 2\mu_f G_2(s)}\sqrt{1 - 4\mu_f}\,. \tag{2.46}$$

For the centre-of-mass energy at the nominal $\mathrm{Z^0}$ mass, $s = M_\mathrm{Z}^2$, when the $\mathrm{Z^0}$ propagator $\chi_0(s)$ becomes purely imaginary, the terms in the expression (2.40) due to the $\gamma \mathrm{Z^0}$-interference drop out. The so called *on-peak Born approximation forward-backward asymmetry* can therefore be written as:

$$A_{FB}^{\mathrm{f\bar{f}}}(M_\mathrm{Z}^2; \mathrm{Born}) = \frac{3}{4} \frac{2v_\mathrm{e}a_\mathrm{e} \cdot 2v_\mathrm{f}a_\mathrm{f}\sqrt{1 - 4\mu_\mathrm{f}}}{(v_\mathrm{e}^2 + a_\mathrm{e}^2)(v_\mathrm{f}^2 + a_\mathrm{f}^2) + \mu_\mathrm{f}(v_\mathrm{e}^2 + a_\mathrm{e}^2)(2v_\mathrm{f}^2 - 4a_\mathrm{f}^2) + \left(\frac{\Gamma_\mathrm{Z}^0}{M_\mathrm{Z}}\right)^2 q_\mathrm{e}^2 q_\mathrm{f}^2(1 + 2\mu_\mathrm{f})} \cdot$$

(2.47)

Neglecting the terms, proportional to μ_f and $(\Gamma_\mathrm{Z}^0/M_\mathrm{Z})^2$ $((\Gamma_\mathrm{Z}^0/M_\mathrm{Z})^2 \sim 10^{-3})$, the *Born approximation forward-backward pole asymmetry* reads:

$$A_{FB}^{0,\mathrm{f\bar{f}}}(\mathrm{Born}) = A_{FB}^{\mathrm{f\bar{f}}}(M_\mathrm{Z}^2; \mathrm{Born}) = \frac{3}{4}\mathcal{A}_\mathrm{e}\mathcal{A}_\mathrm{f} ,$$

(2.48)

with the so-called *left-right flavour asymmetries* being defined as:

$$\mathcal{A}_\mathrm{f} = \frac{2a_\mathrm{f}v_\mathrm{f}}{a_\mathrm{f}^2 + v_\mathrm{f}^2} = \frac{2(1 - 4|q_\mathrm{f}|\sin^2\theta_W)}{1 + \left(1 - 4|q_\mathrm{f}|\sin^2\theta_W\right)^2} \cdot$$

(2.49)

Note that equation (2.49) defines also $\mathcal{A}_\mathrm{e}$ after a replacement of indices: $\mathrm{f} \to \mathrm{e}$.

After neglecting the parameter μ_f, the Born approximation forward-backward pole asymmetry is determined by the values of the fermion charges q_f and by the value of the weak mixing angle, $\sin^2\theta_W$. Measured asymmetries can therefore be used to extract the value $\sin^2\theta_W$. In Table 2.3 calculated values of forward-backward pole asymmetries are given for different fermions and for three values of $\sin^2\theta_W$. For the considered values, the asymmetry is the most pronounced in case of down-like quarks. The down-like quark asymmetry also turns out to be the most sensitive to $\sin^2\theta_W$ (see Figure 2.4). These two features are the most important theoretical motivations for the measurements of $A_{FB}^{\mathrm{b\bar{b}}}$ near the $\mathrm{Z^0}$ peak.

	$A_{FB}^{0,\mathrm{f\bar{f}}}(\mathrm{Born})$		
$\sin^2\theta_W$	leptons (e,μ,τ)	up-like quarks (u,c,t)	down-like quarks (d,s,b)
0.22	0.04198	0.12528	0.16726
0.23	0.01896	0.08022	0.11166
0.24	0.00478	0.03818	0.05571

Table 2.3 : The values of the forward-backward pole asymmetry calculated in Born approximation according to equation (2.48) are listed for different fermion types and for three values of $\sin^2\theta_W$.
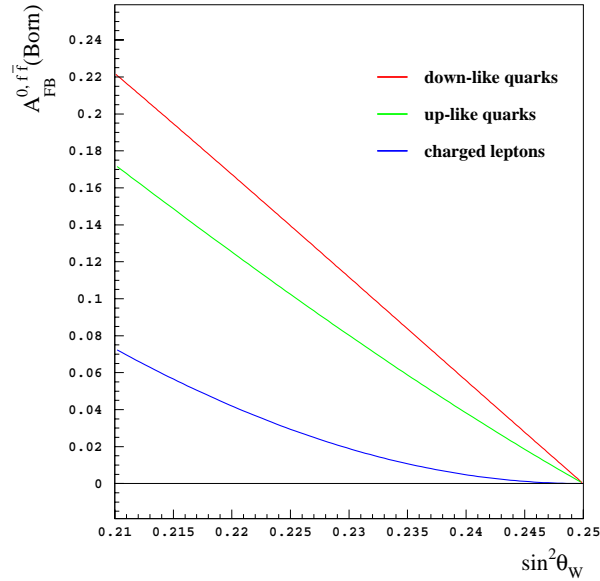
Figure 2.4 : Dependence of $A_{FB}^{0,\mathrm{f\bar{f}}}(\mathrm{Born})$ on $\sin^2\theta_W$.

2.2.2 Corrections to lowest-order diagrams

LEP experiments enable measurements of forward-backward asymmetries to precision that exceeds the accuracy of the lowest-order calculations. For this reason also the higher order contributions to the process $\mathrm{e^+e^-} \to \mathrm{f\bar{f}}$ have to be included in theoretical predictions. Formally, the higher order electroweak corrections to the forward-backward asymmetry can be written in the following form:

$$A_{FB}^{\mathrm{f\bar{f}}}(s) = A_{FB}^{\mathrm{f\bar{f}}}(s;\mathrm{Born}) + \Delta A_{FB}^{\mathrm{f\bar{f}}}(s;\mathrm{RC}) \,. \tag{2.50}$$

As a consequence of these corrections, the forward-backward asymmetry is no more determined only by the electric charge of fermions and by the value of $\sin^2\theta_W$, as it was the case for the tree-level calculations. Namely, the *electroweak radiative correction* term, $\Delta A_{FB}^{\mathrm{f\bar{f}}}(s;\mathrm{RC})$, contains also other parameters of the Standard Model. Measuring the forward-backward asymmetries to a high precision thus represents a possibility for an estimation of parameters of the SM through the radiative correction term. This is especially interesting because of the Higgs mass, M_{H}, the only undetermined parameter of the Standard Model. For this reason, a few additional comments on electroweak corrections are given in this subsection.

    The electroweak corrections contributing to $\Delta A_{FB}^{\mathrm{f\bar{f}}}(s;\mathrm{RC})$ are usually divided into two subgroups:

- "QED corrections" (bremsstrahlung corrections), including Born diagrams with additional photon lines,

- "Weak corrections", consisting of all electroweak corrections apart from QED corrections.

a) Propagator corrections   b) Vertex corrections   c) Box corrections
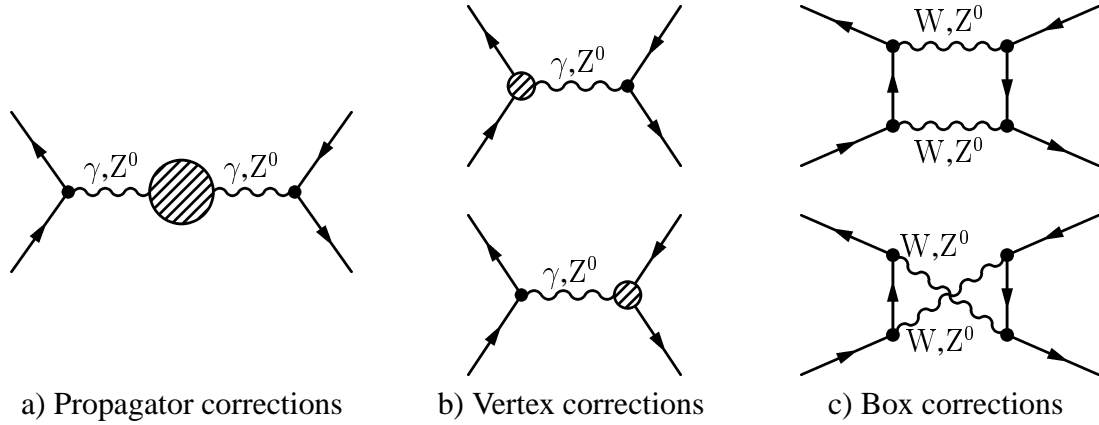
Figure 2.5 : Weak corrections to the process $e^+e^- \to f\bar{f}$. Note that for the WW box corrections to quark asymmetries the upper diagram is relevant only for the d-type quarks, while the lower diagram with the crossed-box topology is relevant only for the u-type quarks. In case of Z^0Z^0 box diagrams both topologies are met.

Due to specific properties, each of these two classes is treated in a different way. The main characteristics of the treatments are described in the following paragraphs.

Weak corrections

The weak corrections are separated from the QED corrections. They are independent of the experimental set-up, but they do depend on all parameters of the theory. In particular, these corrections are sensitive also to the Higgs sector of the Standard Model. It turns out that this dependence is not very strong, but it still enables setting the limits on the mass M_H of the Higgs boson.

The corrections are of three types, shown schematically in Figure 2.5. The contributions due to propagator corrections (Figure 2.5.a) are numerically dominant and universal, i.e. they do *not* depend on the species of incoming and outgoing fermions. Formally they are taken into account by applying several replacements in the Born expression (2.38). For example, the running electromagnetic coupling is used due to the dressed photon propagator:

$$\alpha \longmapsto \alpha(s) \, . \tag{2.51}$$

The dressed Z^0 boson propagator further requires two replacements. The coupling constant for the weak neutral current and the width of the Z^0 boson in the Z^0 propagator become dependent on the centre-of-mass energy s [15]:

$$\alpha_Z = \frac{e_0^2}{4\pi \sin^2\theta_W \cos^2\theta_W} \longmapsto \alpha_Z(s) \tag{2.52}$$

$$\chi_Z^0(s) = \frac{1}{s - M_Z^2 + iM_Z\Gamma_Z^0} \longmapsto \chi_Z(s) = \frac{1}{s - M_Z^2 + i\frac{s}{M_Z^2}M_Z\Gamma_Z} \, , \tag{2.53}$$
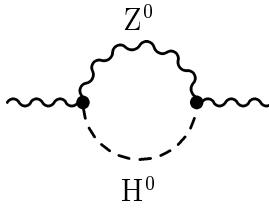
Figure 2.6 : A contribution of the Higgs boson to the first order weak corrections of the propagators.

where Γ_Z is the physical width of the Z^0 boson. The last replacement to be made is due to contributions of the γZ^0-mixing propagator. The contributions can be accounted for by replacing the weak mixing angle θ_W, defined in (2.14), by an effective mixing angle $\theta_{\text{eff}}(s)$:

$$\sin^2 \theta_W \longmapsto \sin^2 \theta_{\text{eff}}(s) = \kappa(s) \sin^2 \theta_W \,. \tag{2.54}$$

The s-dependence of the effective angle is due to the propagator corrections. Note that the propagator corrections include also the Higgs contribution: an example is shown in Figure 2.6.

The weak corrections of vertices and contributions of the so-called box diagrams are depicted in Figures 2.5.b and 2.5.c, respectively. The corrections are taken into account by additional replacements in the expressions of the Born approximation. Contrary to the corrections of propagators, they depend explicitly on the quantum numbers of external fermions. Non-universality of vertex and box corrections now implies different coupling constants (or equivalently – effective mixing angles) for neutral currents of different fermion flavours. Contributions of the Higgs sector to the vertex corrections are depicted in Figures 2.7.a and 2.7.b. Due to the nature of the Yukawa couplings, the contributions are more important for the production of heavy fermions. For the $b\overline{b}$ final state, there is also a significant contribution of the virtual t-quark exchange (see Figures 2.7.c and 2.7.d) due to the diagonal CKM matrix element V_{tb}. In addition, the $Z^0 Z^0$ and WW box diagrams introduce also a t-dependence[4] into the effective couplings. Formally, the corrections due to the dressed vertices and due to the box diagrams read:

$$\sin^2 \theta_{\text{eff}}(s) = \kappa(s) \sin^2 \theta_W \longmapsto \sin^2 \theta_{\text{eff}}^f(s, t) = \kappa_f(s, t) \sin^2 \theta_W \,. \tag{2.55}$$

All the described changes induced by weak corrections can therefore be taken into account by introducing non-universal, energy dependent form factors, conveniently packed into effective couplings. The replacements (2.51)–(2.55) define the so-called *Improved Born Approximation* (IBA).

For example, the one-loop amplitude (OLA) [16] corrections within the IBA are treated as follows. For the corrected γ-exchange amplitude, the corrections are absorbed in the running electromagnetic coupling constant $\alpha(s)$:

$$A_\gamma^{\text{IBA}} = 4\pi\alpha(s) \, q_e q_f \, \chi_\gamma(s) \cdot \gamma_\mu \otimes \gamma_\mu \,. \tag{2.56}$$

---

[4]For a process $e^+ e^- \to f\overline{f}$ the Mandelstam variables are defined as: $s = (p_{e^-} + p_{e^+})^2$, $t = (p_{e^-} - p_f)^2$ and $u = (p_{e^-} - p_{\overline{f}})^2$. Only two of them are independent due to the relation: $s + t + u = 2m_e^2 + 2m_f^2$.
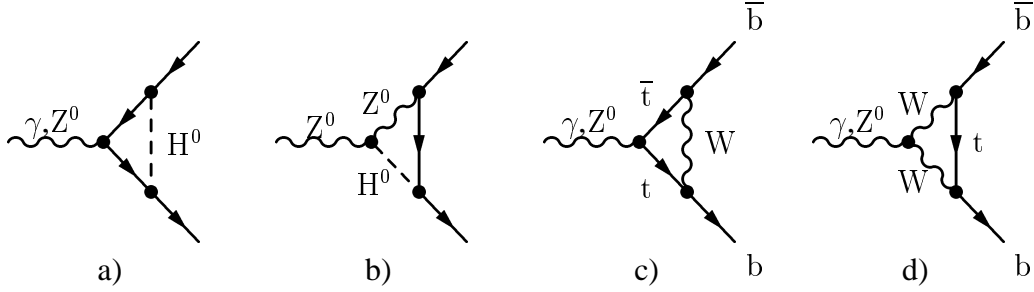
Figure 2.7 : a) and b) Higgs contributions to the vertex corrections. For light quarks these two are negligible due to small Yukawa couplings. c) and d) Virtual top-quark vertex contributions which are important only in the $b\overline{b}$ channel.

The corrections of the Z^0-exchange amplitude are contained in four form factors, $\rho_{ef}(s,t)$, $\kappa_e(s,t)$, $\kappa_f(s,t)$ and $\kappa_{ef}(s,t)$, and in the propagator $\chi_Z(s)$ (see eq. (2.53)):

$$A_Z^{\text{IBA}} = \sqrt{2}G_F M_Z^2 \, I_{W,e}^3 I_{W,f}^3 \, \chi_Z(s) \, \rho_{ef}(s,t) \cdot$$

$$\cdot \left\{ \gamma_\mu(1-\gamma_5) \otimes \gamma_\mu(1-\gamma_5) - 4|q_e|\kappa_e(s,t) \, \sin^2\theta_W \, \gamma_\mu \otimes \gamma_\mu(1-\gamma_5) \right.$$

$$\left. - 4|q_f|\kappa_f(s,t) \, \sin^2\theta_W \, \gamma_\mu(1-\gamma_5) \otimes \gamma_\mu + 16|q_e q_f|\kappa_{ef}(s,t) \, \sin^4\theta_W \, \gamma_\mu \otimes \gamma_\mu \right\} . \tag{2.57}$$

Three out of the four different form factors[5] – κ_e, κ_f and κ_{ef} – account for relative magnitudes of corrections, applied to the four terms of the corresponding Born amplitude (2.36), while $\rho_{ef}(s,t)$ takes into account the correction of the overall normalization.

Since the OLA corrections are contained in the four different form factors, each of them being a function of two Mandelstam variables s and t, it is difficult to extract a contribution of a particular process from the observed forward-backward asymmetry. However, it turns out that at the Z^0 peak the corrections due to the WW and Z^0Z^0 box diagrams become negligible which simplifies the task considerably. In particular, t-dependence of the form factors switches off at $s = M_Z^2$. At the fixed centre-of-mass energy, the form factors can therefore be regarded as constants: $\kappa_f(M_Z^2, t) \approx \kappa_f$. In this way, the flavour-dependent effective mixing angles can be defined as:

$$\sin^2\theta_{\text{eff}}^f = \kappa_f \sin^2\theta_W . \tag{2.58}$$

In case there is no significant contribution from the box diagrams, also the factorization of the form factors in the amplitude (2.57) is re-established to a very good approximation, e.g. $\kappa_{ef} \approx \kappa_e\kappa_f$. The forward-backward pole asymmetry calculated within the IBA can therefore be written in a form analogous to (2.48):

$$A_{FB}^{0,f\overline{f}} = A_{FB}^{f\overline{f}}(M_Z^2; \text{IBA}) = \frac{3}{4}\bar{\mathcal{A}}_e\bar{\mathcal{A}}_f , \tag{2.59}$$

---

[5]The four form factors are independent since *no* factorization can be applied within the IBA: e.g. $\kappa_{ef} \neq \kappa_e\kappa_f$.

with the bare left-right asymmetries being replaced by the effective ones:

$$\bar{\mathcal{A}}_f = \frac{2\bar{a}_f \bar{v}_f}{\bar{a}_f^2 + \bar{v}_f^2} = \frac{2(1 - 4|q_f| \sin^2 \theta_{\text{eff}}^f)}{1 + \left(1 - 4|q_f| \sin^2 \theta_{\text{eff}}^f\right)^2} \; . \tag{2.60}$$

Magnitudes of errors that were possibly introduced by the described simplifications can be estimated by the ZFITTER programme package [17]. It turns out that the errors are negligible when compared to the experimental resolution for all fermion types except for the b quarks, where they are of the order of 10^{-4}. In order to allow for a reliable comparison of the measured and the calculated pole asymmetry $A_{FB}^{0,f\bar{f}}$, the latter has to be corrected for the estimated shifts.

QED corrections
QED corrections are different from the weak ones since they depend strongly on the experimental conditions, i.e. on the criteria for the selection of particular processes. The corrections can be understood as a convolution of corrected weak processes with the emission of various real and virtual photons. Feynman diagrams depicting such processes are given in Figure 2.8. Note that also interferences between these diagrams have to be taken into account.

Quantitatively, the contribution of the QED corrections can again be estimated with the ZFITTER. The results of the QED-corrected $b\bar{b}$ forward-backward asymmetry are shown in Figure 2.9 together with the results for the Born and Improved Born approximations. For the reference, the muon forward-backward asymmetry is also added.
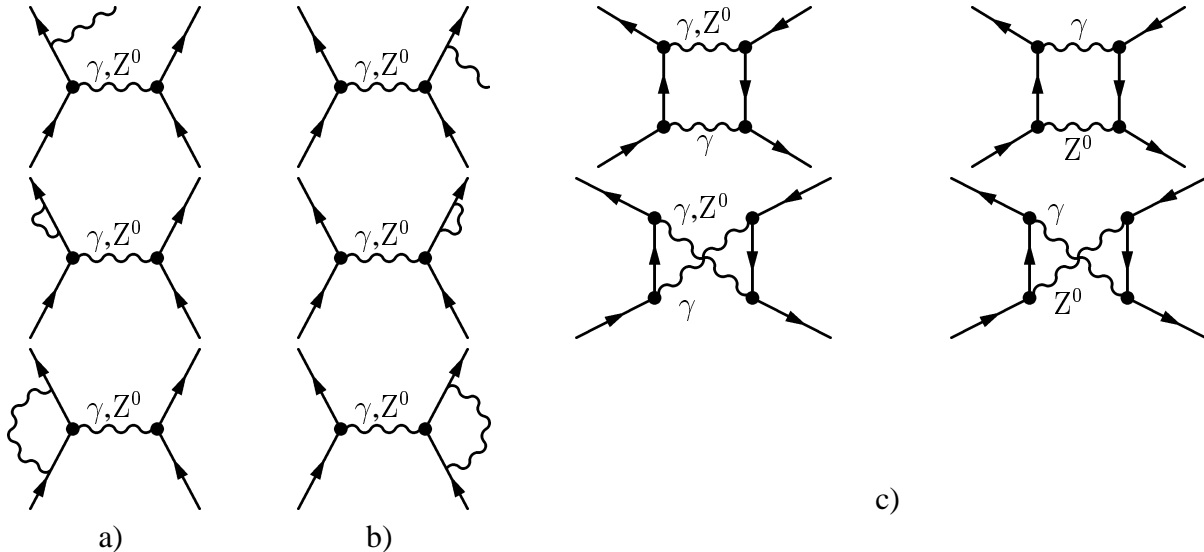
Figure 2.8 : Lowest-order Feynman diagrams for various QED corrections to the process $e^+e^- \rightarrow f\bar{f}$: a) initial state radiation (ISR), b) final state radiation (FSR) and c) γZ^0 and $\gamma\gamma$ box diagrams. Note that in the upper two diagrams of a) and b) one diagram is drawn, while the other ones can be obtained simply by transferring the emitted photon from a fermion to an antifermion or from an electron line to the one for a positron.
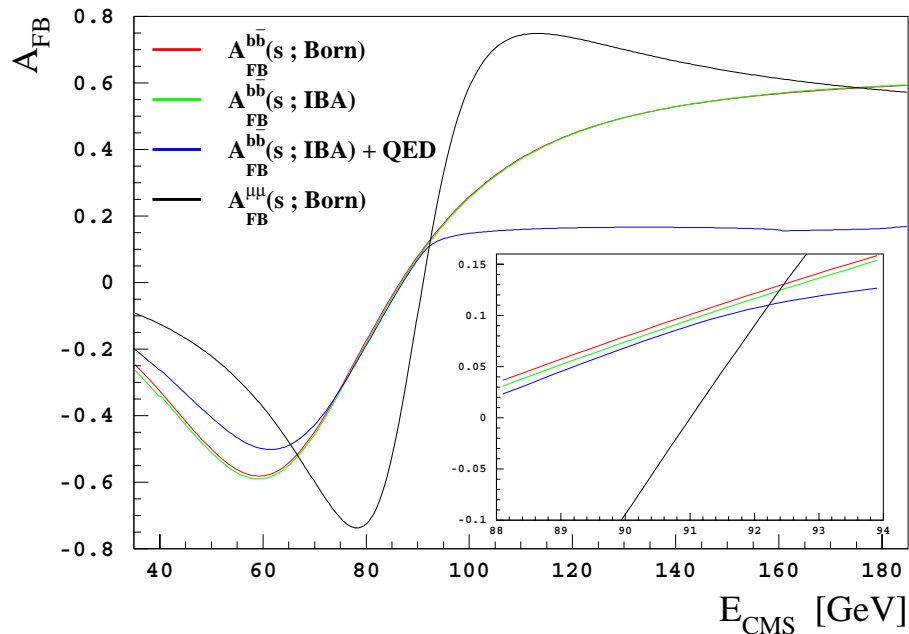
Figure 2.9 : Energy dependence of forward-backward asymmetry for $b\bar{b}$ quark pairs in various approximations. For the sake of comparison the muon forward-backward asymmetry is depicted, too. All curves are obtained with the ZFITTER programme package. Parameters used in calculation were set to their world average values or nominal SM values, while the mass of the Higgs boson was $M_H = 115$ GeV (see Table 2.5).

2.2.3 QCD corrections

Forward-backward asymmetries of fermions, produced in e^+e^- annihilation, are a direct consequence of properties of the electroweak interactions. The strong interactions, however, do *distort* such quark asymmetries by changing the direction of the primary quarks during their evolution to the final-parton level and during the following hadronisation. The most significant contributions come from the hard gluon radiations in the parton shower. Due to the smallness of the strong coupling constant at the LEP momentum transfers [13]:

$$\alpha_s(M_Z^2) = 0.119 \pm 0.002 \,,$$

the impact of the QCD effects on the measured forward-backward asymmetries for quarks is small. Its significance depends also on the technique, used to extract the asymmetry from the data. The QCD distortions and the corresponding corrections of the asymmetries are treated in detail in Chapter 5.

2.2.4 Constraints on the mass of the hypothetical Higgs boson

As already mentioned, precise measurements of the forward-backward asymmetries can be used to set limits on the mass M_H of the hypothetical Higgs boson. The limits are not very stringent
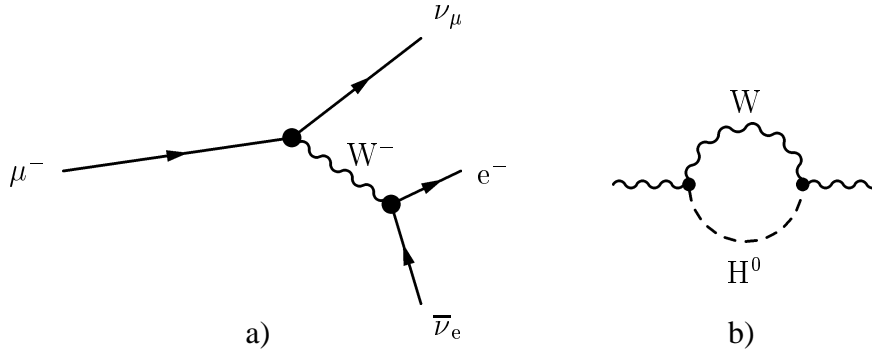
Figure 2.10 : a) Lowest-order Feynman diagram for a muon decay. b) A contribution to the correction of the W propagator with the highest sensitivity to M_H.

since the asymmetries depend only weakly on M_H. On top of that, also other parameters of the Standard Model are known with a limited precision which imposes additional difficulties and uncertainties on indirect measurements of this type. Still, a lack of any direct information on the Higgs sector of the SM motivates these estimations.

The most important corrections of the pole forward-backward asymmetries that contain exchanges of virtual Higgs bosons are almost independent of the flavour of produced fermions. The first of the two processes that introduce most of the sensitivity of the pole asymmetries to M_H is shown in Figure 2.6. It represents a part of the overall propagator correction in OLA calculation.

The second important source of the dependence of $A_{FB}^{0,\text{f}\overline{\text{f}}}$ on M_H comes from the determination of the weak mixing angle θ_W (2.14):

$$\frac{M_\text{W}}{M_\text{Z}} = \cos \theta_W \ . \tag{2.61}$$

Since the precision of direct measurements of M_W is much worse than the precision of corresponding measurements of M_Z (cf. the measured values in Table 2.1), a more accurate value of M_W, extracted from the Fermi constant G_F, is used in (2.61). G_F itself is determined from

Fermions	$\dfrac{\overline{v}_\text{f}}{\overline{a}_\text{f}}$	$\bar{\mathcal{A}}_\text{f}$	$\dfrac{\partial \bar{\mathcal{A}}_\text{f}}{\partial \sin^2 \theta_\text{eff}}$	$A_{FB}^{0,\text{f}\overline{\text{f}}}$	$\dfrac{\partial A_{FB}^{0,\text{f}\overline{\text{f}}}}{\partial \sin^2 \theta_\text{eff}}$
leptons	0.08	0.1590	-7.85	0.01896	-1.81
up-like quarks	0.387	0.6727	-3.43	0.08022	-4.37
down-like quarks	0.693	0.9365	-0.632	0.1117	-5.59

Table 2.4 : Numerical values for effective couplings, left-right asymmetries, forward-backward pole asymmetries and their sensitivities. The universal value of the effective Weinberg angle, $\sin^2 \theta_\text{eff} = 0.23$, was used for this estimation.
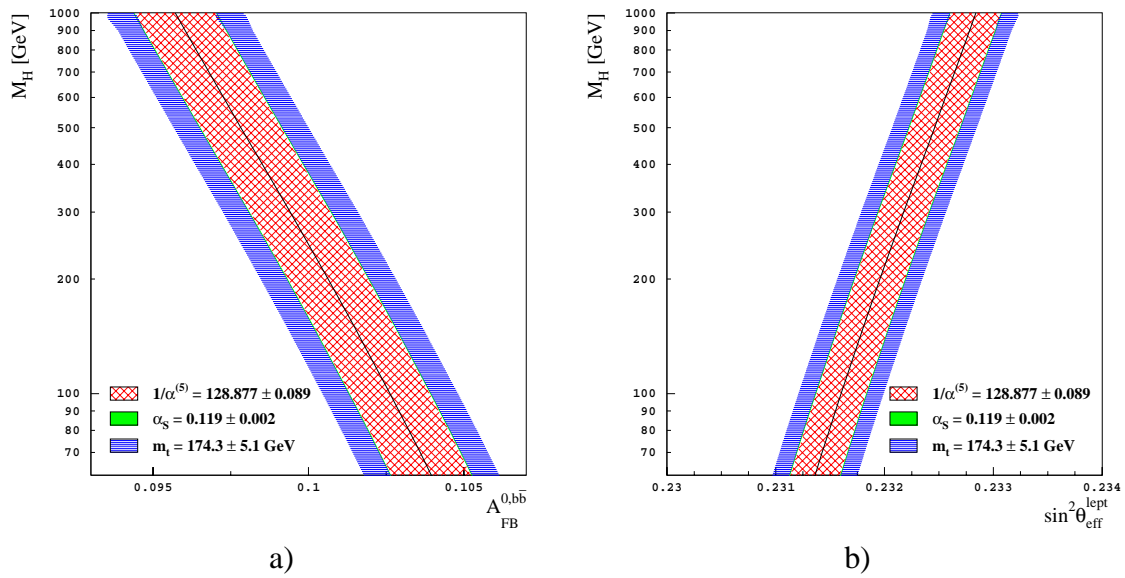
Figure 2.11 : a) Forward-backward $b\overline{b}$ pole asymmetry and b) effective leptonic mixing angle as functions of the Higgs boson mass. The width of the hatched band corresponds to the linear sum of uncertainties due to errors on quoted parameters.

measurements of the muon lifetime. For a precise extraction of M_{W} from G_F, also higher order corrections to the Born-term expression, illustrated in Figure 2.10.a have to be taken into account. Due to a correction illustrated in Figure 2.10.b, the relation between G_F and M_{W} depends also on M_{H}. In this way, a M_{H}-dependent mass of the charged weak boson introduces also a M_{H}-dependence of the weak mixing angle θ_W (see eq. (2.61)). The latter enters asymmetries (2.59) through the relations (2.60) and (2.58).

Figure 2.11.a shows a dependence of the $b\overline{b}$ forward-backward pole asymmetry on M_{H} as calculated by the DIZET routine of the ZFITTER programme package [17]. The width of the corresponding line in the figure is determined by uncertainties on other parameters of the Standard Model. The largest uncertainty comes from the error on the running of the electromagnetic coupling α because of the difficult calculations of light quark loop contributions.

The pole asymmetry $A_{FB}^{0,\mathrm{f\overline{f}}}$, calculated within the IBA (2.59), can be expressed as a product of the effective left-right asymmetries $\bar{\mathcal{A}}_{\mathrm{e}}$ and $\bar{\mathcal{A}}_{\mathrm{b}}$ (2.60). Of the two left-right asymmetries, $\bar{\mathcal{A}}_{\mathrm{e}}$ is for an order of magnitude more sensitive to the value of $\sin^2\theta_{\mathrm{eff}}$ and thus to M_{H} (see Table 2.4). Because of this and in order to make a comparison of the asymmetries for different fermions easier, the measured asymmetries are usually quoted in terms of the effective lepton angle $\sin^2\theta_{\mathrm{eff}}^{\mathrm{lept}}$, defined by the electron couplings[6]:

$$\sin^2\theta_{\mathrm{eff}}^{\mathrm{lept}} = \frac{1}{4}\left(1 - \frac{\overline{v}_{\mathrm{e}}}{\overline{a}_{\mathrm{e}}}\right) . \qquad (2.62)$$

---

[6]The definition implies that for muons and τ leptons a lepton universality is assumed.

Parameter	Value
M_Z	91.187 **GeV**
$1/\alpha(0)$	137.0359895
G_F	$1.16637 \cdot 10^{-5}$ **GeV**$^{-2}$
$1/\alpha^{(5)}(M_Z^2)$	128.877 ± 0.089
m_t	(174.3 ± 5.1) **GeV**
α_S	0.119 ± 0.002
M_H	115 **GeV**

Table 2.5 : A set of values of the SM parameters used in the DIZET routine for the calculation of $\bar{\mathcal{A}}_b$. $\alpha^{(5)}(M_Z^2)$ is the running electromagnetic coupling with the lepton and five quark loop contributions. The errors quoted for some parameters were taken from ref. [13] and used to determine the uncertainties of the Higgs-mass estimates in Figure 2.11.

In what follows, a procedure for the extraction of $\sin^2 \theta_{\text{eff}}^{\text{lept}}$ from the measured forward-backward asymmetries, is described. The procedure was adopted by all four LEP experiments and by the LEP electroweak working group [5]. At the beginning, the pole asymmetry is obtained from the measured asymmetry by correcting for possible QED and QCD distortions, as well as for the center-of-mass energy shift from the Z^0 peak. At the same time, the left-right asymmetry $\mathcal{A}_b$ for b-quarks is calculated by the DIZET routine of the ZFITTER package. Doing this, the parameters of the Standard Model are set to their nominal values. Table 2.5 shows a set of the values used in the present analysis. Using the central values of these parameters, the value $\bar{\mathcal{A}}_b = 0.934607$ was calculated. Having the measured pole asymmetry extracted and the left-right asymmetry $\bar{\mathcal{A}}_b$ calculated, a value of the electron left-right asymmetry $\bar{\mathcal{A}}_e$ and thus a value of the effective lepton angle $\sin^2 \theta_{\text{eff}}^{\text{lept}}$ can be obtained by using equations (2.59) and (2.58). Figure 2.11.b shows a dependence of the effective lepton angle on the mass of the hypothetical Higgs boson.

2.3 Measurement of the forward-backward $b\overline{b}$-asymmetry using charged kaons

Besides the theoretical motivations for the measurement of $A_{FB}^{b\overline{b}}$ illustrated in the previous subsection, measurements of forward-backward asymmetry in the $b\overline{b}$ channel are also experimentally motivated. Namely, there are several kinematic properties of $Z^0 \rightarrow b\overline{b}$ decays that allow for an isolation of $b\overline{b}$ final states out of all produced $q\overline{q}$ final states. These properties and the experimental idea of the so-called b-tagging are described more thoroughly in the next chapter.

In order to measure the forward-backward asymmetry for the process $e^+e^- \rightarrow b\overline{b}$, the charges of the original quarks have to be determined from the final-state particles. In the measurement that is the subject to this thesis, charged kaons produced inclusively in the quark decay

a)

b)
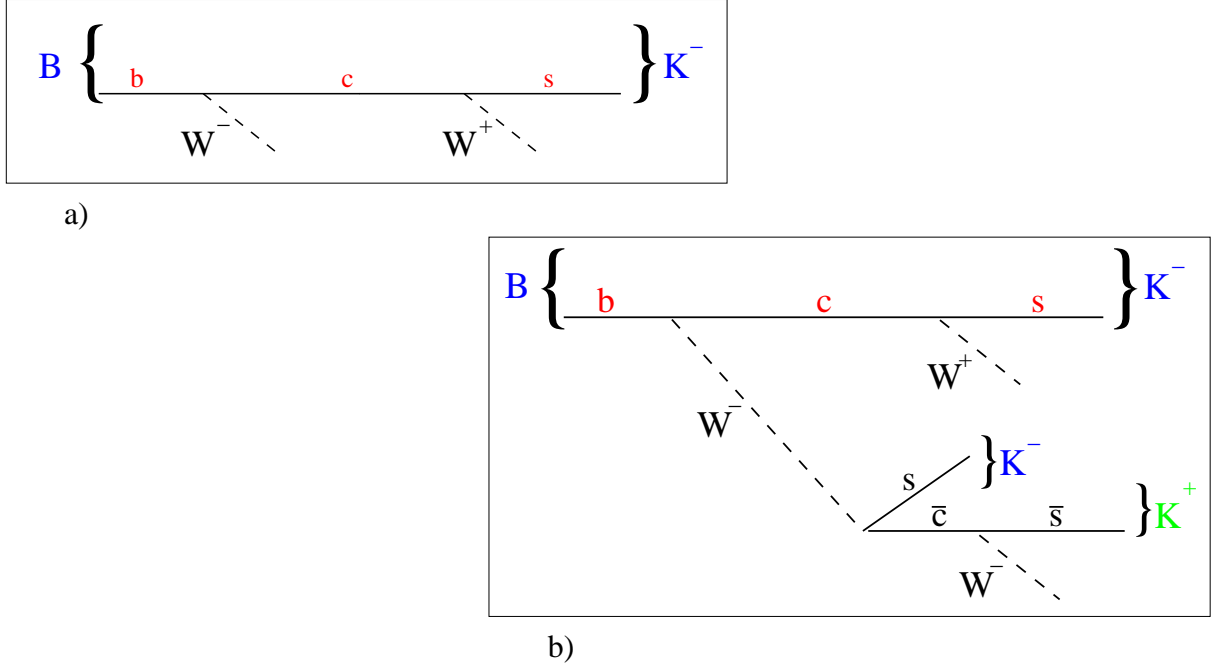
Figure 2.12 : a) Quark decay chain $b \to c \to s$. At the end, the charge of the produced kaon K^- can be used to tag the charge of the original b quark. b) A decay chain of a b quark where apart from two correct-charge kaons also a wrong-charge kaon is produced.

chain

$$b \to c \to s \tag{2.63}$$

are used to tag the charge of the initial quark[7]. It is due to the decay chain (2.63) that a jet, originating from a b-quark fragmentation, contains more negatively than positively charged kaons, and the opposite is true for $\overline{b}$ jets. The b-quark forward-backward asymmetry therefore implies also a charged-kaon asymmetry:

$$A_{FB}^{K} = \eta_b A_{FB}^{b\overline{b}} \,. \tag{2.64}$$

Or, the other way around, one can deduce $A_{FB}^{b\overline{b}}$ from the kaon asymmetry. The two asymmetries are related via a dilution factor:

$$\eta_b = 2c_b - 1 \,, \tag{2.65}$$

which is a simple function of a probability c_b for the correct kaon tagging of the b-quark charge. In other words, c_b is a probability that a detected K^- belongs to a jet originating from a produced b quark and *not* from a produced $\overline{b}$. The opposite is true for K^+. Charged kaons, with a charge matching the charge of the quark they originate from, are referred to as *correct-charge kaons*. A decay chain (2.63), leading to a production of such kaons, is depicted in Figure 2.12.

---

[7]When a particular process throughout the thesis is written, the charge-conjugated states are included implicitly, unless stated otherwise.

However, a considerable amount of the so-called *wrong-charge kaons* is also produced during the process of the b-quark hadronisation, during the lifetime of the produced B hadrons and also during their decay, as well as during the hadron identification (see Figure 2.12 for an example). Wrong-charge kaons diminish the power of the described tagging and have therefore a direct impact on the significance of the results, extracted in this thesis.

3

Experimental set-up

The set-up for collecting the experimental data used in this analysis consisted of the accelerating and colliding facilities for electrons and positrons on the one hand and the detector of the produced particles on the other hand.

3.1   The LEP collider

The Large Electron-Positron (LEP) collider [18] was located at the European Laboratory for Particle Physics (CERN) near Geneva. With a circumference of 26.7 km this collider was the largest accelerator in the world. It was positioned in the tunnel which was excavated about 100 m underground between the Jura mountains and the Lake of Geneva, as can be seen on the map of the region, depicted in Figure 3.1. It took six years for the accelerator to be constructed and finally put into operation in 1989. From the year 1989 to 1995, during the LEP1 period, the accelerator operated at the collision energy of about 91 GeV. At the end of October 1995, tests with beam energies between 65 GeV and 68 GeV started, so that in 1996 the collider could operate at the center-of-mass energies above 160 GeV. This marked the start of the LEP2 phase. Since the data used in this analysis were collected during the LEP1 period, in what follows, all descriptions of the accelerator and a detector (see the next Section) will be given for the years up to 1995.

Electrons and positrons colliding in LEP were produced and then accelerated in several stages before being injected to LEP (see Figure 3.2). The first stage was called the LEP Pre-Injector (LPI). Electrons from an electron gun and positrons from the tungsten electron-to-positron converter were first accelerated to 600 MeV in the LINAC Injector for LEP (LIL) and then stored in an Electron-Positron Accumulator (EPA). After having accumulated about hundred injections of electrons and positrons from LIL, EPA passed the particles to the second stage, the CERN Proton Synchrotron (PS). Leptons were then accelerated to 3.5 GeV and injected to the third-stage accelerating machine, CERN Super Proton Synchrotron (SPS). In SPS, beams were accelerated to an energy of 20 GeV and finally injected to the final-stage accelerator, LEP. Due to this acceleration procedure, produced electron and positron beams were not continuous, but contained particles grouped into several bunches.

27
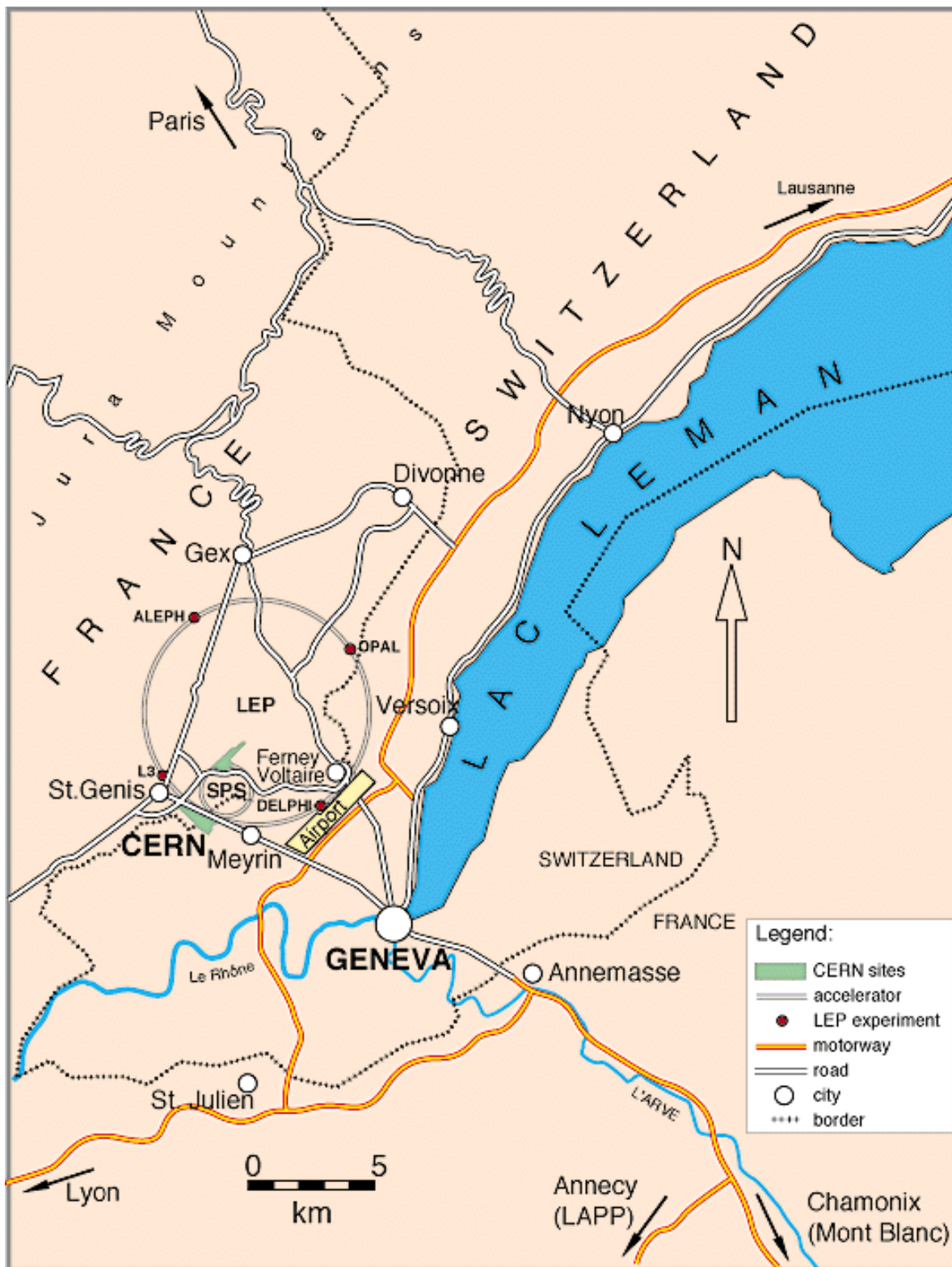
Figure 3.1 : The location of the CERN laboratory and the LEP accelerator.
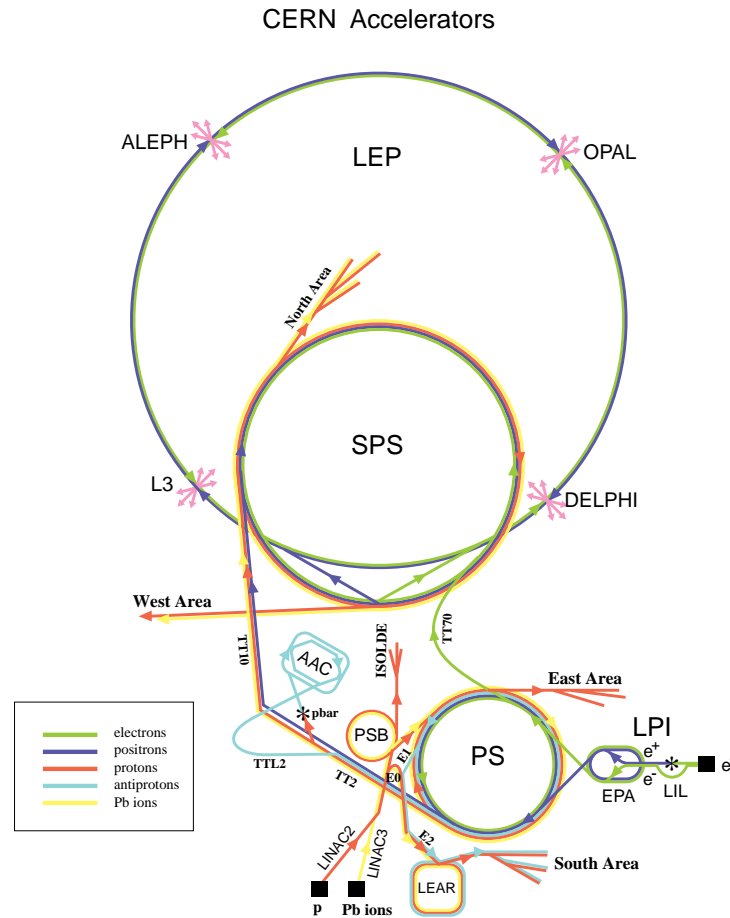
CERN Accelerators

Figure 3.2 : Scheme of the accelerator complex in CERN. The LEP accelerator chain (LPI–PS–SPS–LEP) can be tracked down by following the electron and positron lines.

In LEP, the beams were first accelerated to the final energy. This was done by RF cavities positioned in the eight straight sections of the accelerator. In the interlaying bent sections, the beams were then curved and guided into orbits by dipole, quadrupole, sextupole and other magnets. When the desired beam energy was reached, LEP started performing as an electron-positron storage ring. The cavities were then used to compensate for the energy loss of the beams due to the synchrotron radiation. The loss was quite significant, since it is proportional to E_b^4/R_L, where E_b is the beam energy and R_L is the LEP radius [18]. The lifetimes of the colliding beams at LEP1 were about 20 hours, with the main beam lifetime limitations coming from beam-beam bremsstrahlung ($e^+e^- \to e^+e^-\gamma$) and from scattering of beams on the rest gas in the vacuum tube and on thermal photons [19]. The beams at LEP1 were typically kept in collision for 10–12 hours. After that, the beams were dumped and the entire operating cycle was repeated.

For detection of particles produced in collisions of electrons and positrons, four multipurpose detectors were located in every second straight section of the LEP tunnel, at points where beams collided. The purpose of putting four detectors instead of one at the same collider was

in enabling independent measurements on the one hand and having better statistics on the other hand. The detectors ALEPH, DELPHI, L3 and OPAL were similar, but each of them was characterized by some special features. At the centre of every detector, electron and positron beams coming from opposite directions were additionally focused in order to obtain high luminosities. *Luminosity* $\mathcal{L}$ is one of the most important parameters of the accelerator, since it connects the expected event rate of a specific process i with its cross-section σ_i:

$$\frac{dN_i}{dt} = \mathcal{L}\sigma_i . \tag{3.1}$$

For the two beams overlapping completely, the luminosity depends on the machine parameters in the following way:

$$\mathcal{L} = k_b \, \nu_{rev} \, \frac{N_{e^+} N_{e^-}}{4\pi \sigma_x \sigma_y} . \tag{3.2}$$

Here, ν_{rev} is the revolution frequency of the beams (about 11.25 kHz for LEP), k_b is the number of bunches (4, 8 or 12 in 1995) in either of the beams around the ring and N_{e^+}, N_{e^-} are the numbers of electrons and positrons per bunch (between $1.0 \cdot 10^{11}$ and $1.5 \cdot 10^{11}$) [19]. At the interaction point, the dimensions of the beam in the plane perpendicular to beam directions were $\sigma_x = 200$ μm and $\sigma_y = 3.5$ μm. Rather than the rate, one is usually interested in the total number of events of a specific type. For this reason, the quantity commonly quoted is the (time-)integrated luminosity, $L = \int \mathcal{L}dt$, delivered to a particular experiment.

In principle, it is possible to calculate the luminosity (3.2) only by knowing the specific beam parameters. However, in practice these parameters are usually not known with a precision which is good enough for the experimental purpose and the luminosity is measured more accurately according to the definition (3.1): by knowing the cross-section of a specific process and by measuring the reaction rate. The process used for the measurement is the Bhabha scattering, i.e. the electron-positron scattering, $e^+e^- \rightarrow e^+e^-(\gamma)$. This is a pure QED process, so the cross-section can be calculated with a high accuracy – the theoretical uncertainty of the calculations is estimated to 0.11 % [20]. The Bhabha scattering cross-section is also large enough, so that the interaction rate ensures small statistical error of the luminosity measurement. Since the majority of the particles are scattered at small angles with respect to the beam, this enables Bhabha events to be well separated from events due to other processes.

As already mentioned, between 1989 and 1995 LEP operated at the collision energy of about 91 GeV, the rest energy of the Z^0. During this – LEP1 phase – the Z^0 was the most frequent product of electron-positron collisions. An energy scan in the region of about 6 GeV around the Z^0 peak enabled the measurement of energy dependence of cross-sections and forward-backward asymmetries. The peak luminosity in the LEP1 phase was usually about $1.5 \cdot 10^{31}$ cm^{-2}s^{-1}, so that one hadronic Z^0 decay was produced every two seconds at each beam collision point. The total integrated luminosity delivered to each of the four detectors amounted to about 200 pb^{-1} (see Table 3.1). This luminosity enabled the four experiments to detect together about 20 million Z^0 decays during the years 1989 and 1995 [21].

Year	$\int \mathcal{L} dt$ [pb^{-1}]
1989	1.7
1990	7.6
1991	17.3
1992	28.6
1993	40
1994	64.4
1995	39.9

Table 3.1 : Integrated luminosities per experiment for various years of LEP1 operation at energies near the Z^0 peak [21].

3.2 The DELPHI detector

The DELPHI (DEtector with Lepton, Photon and Hadron Identification) spectrometer was one of the four detectors used for measuring the products of the electron-positron collisions at LEP. It was a general purpose detector with efficient and accurate tracking, good calorimeter performance and particle identification capabilities over an almost full solid angle and momentum range. The spectrometer was composed of many sub-detectors (see Figure 3.3), which can be divided into several groups according to the performing tasks. In what follows, the groups of sub-detectors will be briefly described, with the emphasis given on the components relevant for the analysis presented in this thesis. The detailed description of the detector and its performance are given elsewhere [22, 23].

Roughly speaking, the DELPHI detector consisted of a central cylindrical section – the *barrel* region, and two end-caps on each side, referred to as the *forward* regions. The end-caps could be moved away from the barrel region by 2.8 m to allow rapid access to the various sub-detectors. The overall length and the diameter of the detector were about 10 m, while its mass was roughly 3500 tons. The z-axis of the detector coordinate system was the direction of the electron beam, the x-axis coincided with the radial direction of the LEP ring, while the y-axis pointed toward the ground. For various descriptions cylindrical and spherical coordinates are often used instead. The plane perpendicular to the z-axis is described by the radius R and the angle ϕ, while the polar angle θ is 0 along the z-direction.

The Solenoid

In the central part of the detector, the superconducting solenoid with a length of 7.4 m and an inner diameter of 5.2 m, provided the magnetic field parallel to the beam axis. The field was used for bending the tracks of charged particles, enabling thus the measurement of their momenta (see below). For the purpose of precise momentum measurement, the field of 1.2 T produced with a current of 5000 A was very homogeneous: inside the Time Projection Chamber deviations of the longitudinal component of the field were of the order of 10^{-4} T, and the radial component was less than 0.0005 T [22].
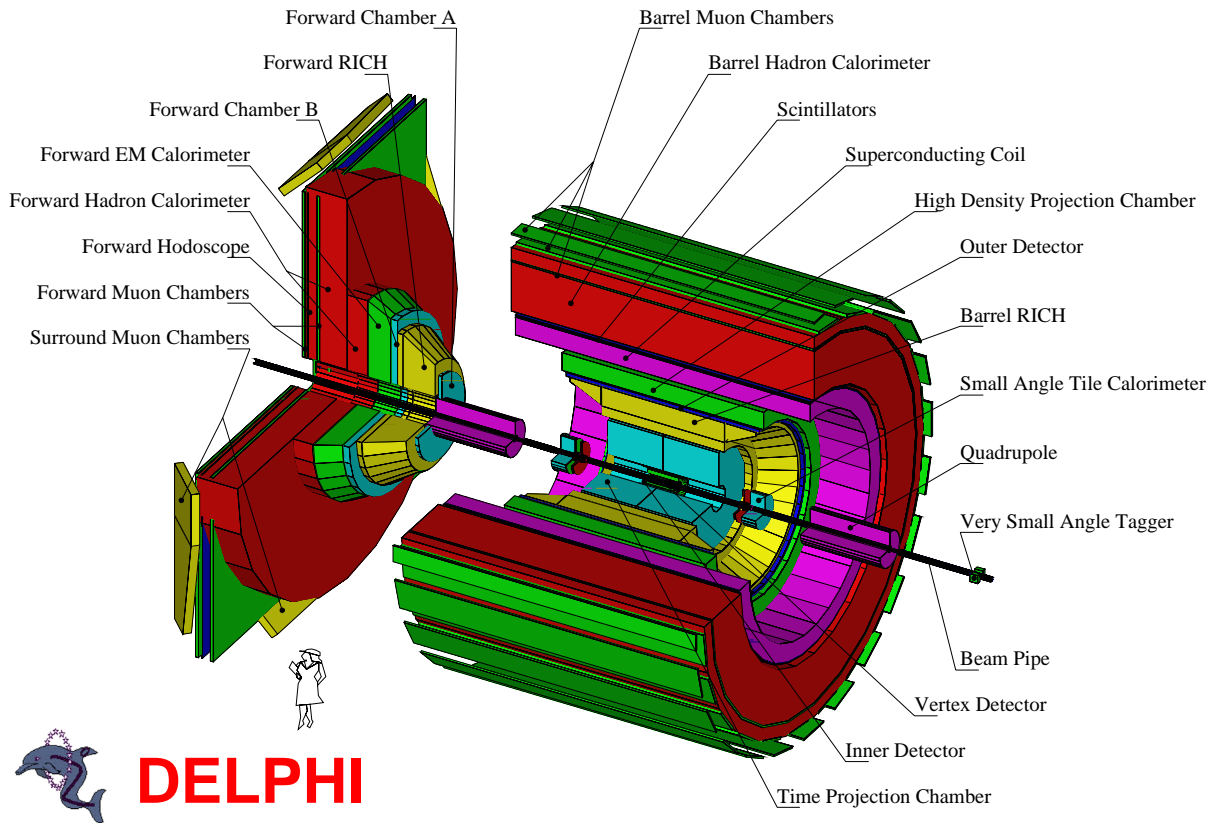
Figure 3.3 : A schematic view of the DELPHI spectrometer with the barrel region and one of the two end-caps shown. The size of the detector is compared to a human size.

3.2.1   Tracking sub-detectors

Tracking sub-detectors were used for detection and reconstruction of tracks of long-living charged particles: $e^\pm$, $\mu^\pm$, $K^\pm$, $\pi^\pm$ and $p(\overline{p})$. Flying through the detector material, these particles produce free charge carriers along their path. Detection of these charge carriers and determination of their points of origin enables one to identify the space points through which the trajectory of charged particles can then be fitted. The general requirement imposed on the tracking system is that it should provide good space precision of the track reconstruction, with smallest possible changes of the particle momentum and energy. This can be achieved only with a careful material selection and design of components. The tracking sub-detectors in DELPHI included Vertex Detector, Inner Detector, Time Projection Chamber and Outer Detector in the barrel region, and Forward Chambers in the end-caps. The main characteristics of these components are described below.

Vertex Detector (VD)
The vertex detector [24] was the innermost sub-detector, located just outside the beam pipe. It
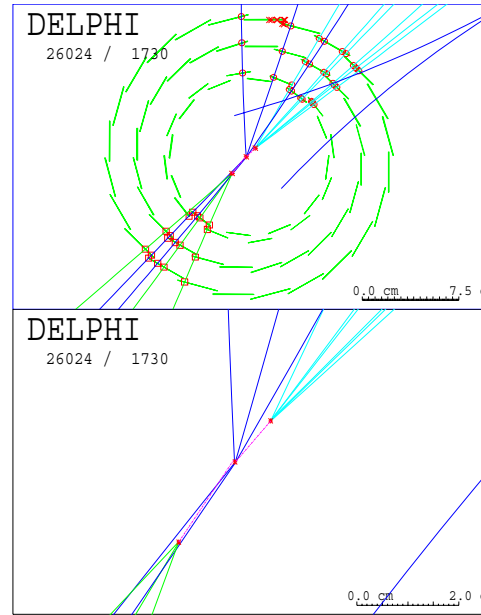
Figure 3.4 : Event display showing decays of hadrons containing b quarks (B hadrons) reconstructed from charged tracks in the vertex detector. The uppermost picture shows the projection onto the $R\phi$-plane, where also the three layers of VD are seen. The magnified view of the central part is shown below, so that tracks coming from the B-hadron decay points are clearly visible.

consisted of three concentric layers of silicon micro-strip detectors at average radii of 6.3, 9.0 and 11.0 cm from the interaction region. Until 1993, the angular acceptance of this detector was $44° \leq \theta \leq 136°$ for particles crossing all three layers. At that time, the detector provided only measurements of the $R\phi$-coordinates. In 1994, the innermost and the outermost VD layers were equipped with double-sided silicon detectors, with two layers of strips orthogonal to each other on opposite sides of the detector wafer. This upgrade enabled measurements of z-coordinates as well. At the same time, the angular acceptance for the innermost layer was enlarged to $25° \leq \theta \leq 155°$. So most of the data were taken with the upgraded detector.

The precision of the track position measurement for a single layer of the Vertex Detector was about 8 μm in the $R\phi$-direction. In the z-direction the resolution was a function of the incidence angle of the track and it varied from 9 μm for tracks perpendicular to the module to about 30 μm for tracks at $\theta = 45°$ [23]. The precision of the VD enabled reconstruction of the B-hadron decay point, since B hadrons have a lifetime of 1.6 ps [13] and they typically fly a few millimetres away from the primary interaction point before they decay. This feature can be used for the so called b-tagging, separation of b$\overline{\text{b}}$ events from other hadronic events (see Chapter 4). Figure 3.4 shows an event, where tracks of a b-decay candidate were reconstructed by the Vertex Detector.

Inner Detector (ID)
This sub-detector lay outside the Vertex Detector, between 12 cm and 28 cm of radius. It consisted of two parts: the inner Jet Chamber and outer Trigger Layers (TL). The Jet Chamber

was a drift chamber providing up to 24 $R\phi$-points per charged track between radii of 12 and 23 cm and covered polar angles in the range $23° \leq \theta \leq 157°$. Points were determined by the sense wires, measuring the drift time of the electrons from the ionization position. Trigger layers were used for fast triggering, but also for determining the drift direction of the electrons in the drift chamber. In the beginning, TL's consisted of five layers of multiwire proportional chambers (MWPC's) with circular cathode strips and 192 sense wires, thus providing both, $R\phi$- and z-information. In the beginning of 1995, the layers of proportional chambers were replaced by five layers of straw-tube detectors. These detectors had the same functionality as the old MWPC layers, except there was no longer any z-measurement. The sub-detector was also extended, so that the new polar angle coverage of the ID was then $15° \leq \theta \leq 165°$.

The achieved average single wire $R\phi$-resolution was about 90 μm. When combining multiple hits in the Jet Chamber and information from Trigger Layers, the maximum achieved precision for $R\phi$-measurement was 50 μm for MWPC's and 40 μm in the case of straw tubes. Separation resolution for two charged tracks was of the order of 1 mm. A schematic view of the ID is presented in Figure 3.5.
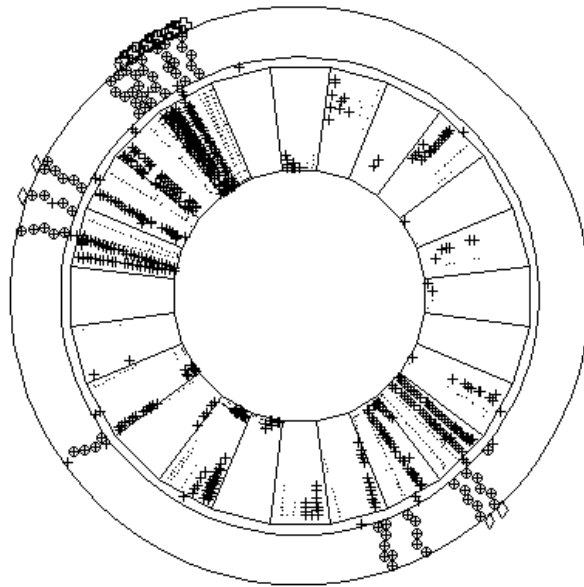
Figure 3.5 : The $R\phi$-cross-section through the inner detector as seen at the event display for a hadronic Z^0 decay. The hits made by charged tracks in the inner layer (drift chamber), divided into 24 azimuthal sections, and in the outer layers (straw tubes) can be seen.

Time Projection Chamber (TPC)
The TPC [25], the main DELPHI tracking device, was a 3.34 m long cylinder with inner and outer radius of 30 cm and 122 cm, respectively (see Figure 3.6). The detector provided a 3-dimensional measurement of particle trajectories. Electrons, produced through the ionization of gas (a gas mixture was composed of 80% Ar and 20% CH_4) by charged particles, drifted

in the electric field parallel to the beam axis towards the detecting planes at both ends of the cylinder. Since the drift time of electrons was used to determine the z coordinate, the monitoring of the drift velocity was of crucial importance for TPC measurements. The electric drift field of 150 V/cm was produced by the high voltage plate at 20 kV, dividing the drift volume into two halves. The two electron-detecting planes were divided into 6 sectors equipped with MWPC's. Each of the chambers contained 192 sensitive wires and a cathode with 16 circular rows of capacitive pads. The induced electric signal on the cathode pads served for the measurement of the $R\phi$-coordinate of the charged track. Up to 16 space points could be measured for angles $39° \leq \theta \leq 141°$. Outside this region, extending on one side to $20°$ and on the other to $160°$, there were at least 3 points per track available, thus enabling the reconstruction of the charged particle trajectory.

The spatial resolution for a single track point was 250 μm in $R\phi$- and 880 μm in z-direction. Two points were considered as separated if the distance between them was at least 1 cm in each direction. Apart from the position measurement, TPC provided also an information for particle identification, since each sensitive wire measured specific energy loss dE/dx for charged tracks.
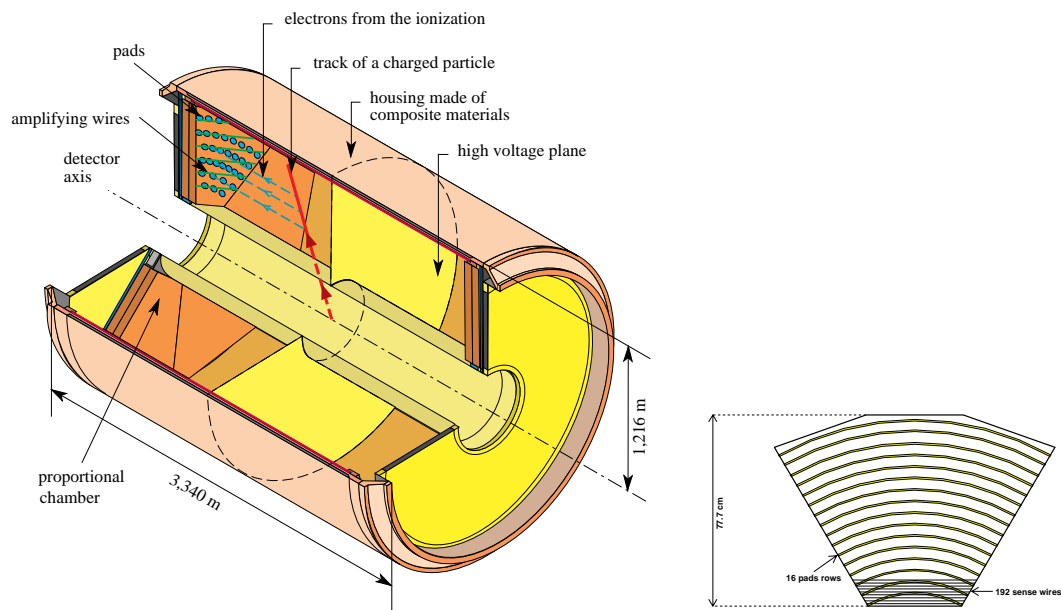
Figure 3.6 : Schematic view of the DELPHI TPC. Left figure shows the entire cylinder, while the right one depicts one of the sections in the detecting planes.

Outer Detector (OD)

This sub-detector completed the tracking in the barrel region. It was composed of 24 azimuthal modules, each consisting of 145 drift tubes in 5 layers. Drift tubes in different layers overlapped, thus providing full azimuthal coverage (see Figure 3.7). OD improved the momentum resolution of the tracking system, since it provided additional charged-track points at radii between 197

and 206 cm. It covered the polar angle between $43°$ and $137°$. All the layers provided $R\phi$-information, while the middle three of them were equipped to measure also z-coordinate of the charged track by timing the signals at the ends of the anode wires. Single point precisions were 110 μm in $R\phi$-plane and 3.5 cm in z-direction [23].
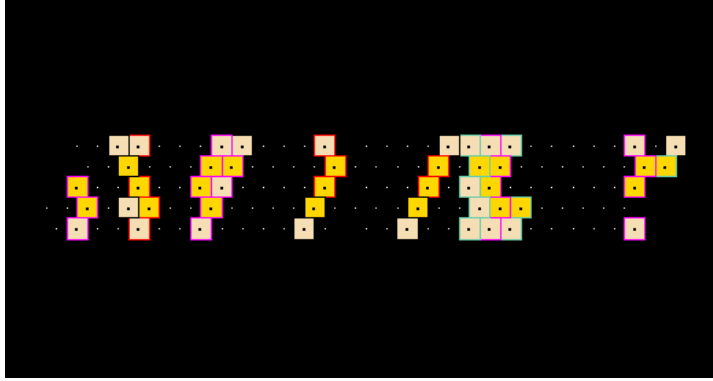
Figure 3.7 : The $R\phi$-cross-section through one of the 24 azimuthal modules of the OD: 145 drift tubes arranged in 5 layers are shown schematically. Tubes, hit by charged particles, are displayed in colours.

Forward Chambers (FCA and FCB)

Each of these sub-detectors were composed of two planes of drift chambers, placed at ±160 cm (FCA) and ±270 cm (FCB) in the z-direction. The chambers provided measurements of low angle particle trajectories, going into the forward regions: for FCA the angular region covered was $11° \leq \theta \leq 32°$ and $148° \leq \theta \leq 169°$, while FCB measured tracks with polar angles $11° \leq \theta \leq 36°$ and $144° \leq \theta \leq 169°$. A single wire resolution of about 190 μm and 300 μm was achieved for FCA and FCB, respectively.

3.2.2 Measurement of track parameters

Since the tracking detectors were placed in the magnetic field provided by the superconducting solenoid, the reconstruction of tracks bent in the field enabled the determination of the charged-particles momenta. The precision of the particle momentum measurement was a function of polar angle θ and momentum itself, but it also depended on the number of tracking detectors used for the track reconstruction. The overall momentum measurement performance of the tracking system is best illustrated by the average momentum resolution for muons from the $Z^0 \rightarrow \mu^+\mu^-$ decay. For the complete barrel tracking system (VD, ID, TPC and OD), the distribution of the inverse muon momentum could be fitted with the sum of two Gaussians having the same mean value. The narrower one, including about 92 % of events, had a width of:

$$\sigma(1/p) = 0.57 \cdot 10^{-3} \ (\text{GeV})^{-1}, \tag{3.3}$$

while the width of the second Gaussian was $1.04 \cdot 10^{-3} (\text{GeV})^{-1}$ [23]. The same approach for muons in the forward region, seen at least in the VD and FCB, yielded a precision of

$$\sigma(1/p) = 1.31 \cdot 10^{-3} \ (\text{GeV})^{-1} \, . \tag{3.4}$$

The dependence of the resolution on the polar angle of the charged track and on the track momentum could be estimated by comparing the simulated and reconstructed track parameters in a sample of generated Z^0 hadronic decays. Tracks from such decays typically had smaller momenta than the muons described above and due to larger curvatures the momentum resolution was expected to be superior. On the other hand, the precision was affected by the multiple scattering, which dominated the resolution bellow 2.5 GeV and contributed a constant term of about 0.6% to the relative momentum resolution. As far as the angular dependence is concerned, the general feature for samples of tracks in certain momentum intervals was that the precision remained essentially constant over the barrel region, but deteriorated in forward regions of the detector. For particles with momentum of 10 GeV, produced at the angles of about $20°$, the relative precision was estimated to about 7% [23].

Apart from particle momentum, the second important track characteristic is its impact parameter, i.e. the minimum distance with respect to the reconstructed primary interaction point. Track impact parameters could be used to separate various $q\bar{q}$-events (see the description of b-tagging technique in the next Chapter). The impact parameters in the $R\phi$- and z-planes were evaluated separately. The performance of all four tracking sub-detectors in the barrel region led to the following parameterisation of track extrapolation error of impact parameter d in $R\phi$-plane [23]:

$$\sigma_{d_{R\phi}} = \sqrt{\left(\frac{65 \ \mu\text{m} \cdot \text{GeV}}{p \sin^{3/2} \theta}\right)^2 + (20 \ \mu\text{m})^2} \, , \tag{3.5}$$

The first term above, depending on the polar angle θ, describes the multiple scattering contribution and the second one is due to the measurement error, i.e. due to intrinsic resolution of tracking detectors. The extrapolation error on impact parameter in z-plane showed even stronger dependence on the polar angle θ of the charged track. This was because, apart from increase of the multiple scattering uncertainty due to the larger path travelled in the material, there was also an additional influence on the measurement error due to the varying point precision in z-coordinate. For tracks within the barrel region the parameterisation of extrapolation error on impact parameter in z-plane was of the form:

$$\sigma_{d_z} = \sqrt{\left(\frac{\alpha_{MS}(\theta)}{p}\right)^2 + \left(\sigma_{0,z}(\theta)\right)^2} \, , \tag{3.6}$$

with the two coefficients $\alpha_{MS}(\theta)$ and $\sigma_{0,z}(\theta)$ varying from $71 \ \mu\text{m} \cdot \text{GeV}$ and $39 \ \mu\text{m}$ for almost perpendicular tracks ($80° < \theta < 90°$) to $151 \ \mu\text{m} \cdot \text{GeV}$ and $96 \ \mu\text{m}$ for tracks at the edge of the barrel region, with $45° < \theta < 55°$ [23].

3.2.3 Calorimetry

Calorimeters are used to detect neutral particles and to measure the energy of both, neutral and charged particles. For this purpose, it is required that particles deposit most of their energy in the calorimeter. At the same time calorimeters have to be made and read out in a way precise enough to determine the position of traversing tracks. There were two types of calorimeters in DELPHI: hadron calorimeter and electromagnetic calorimeters.
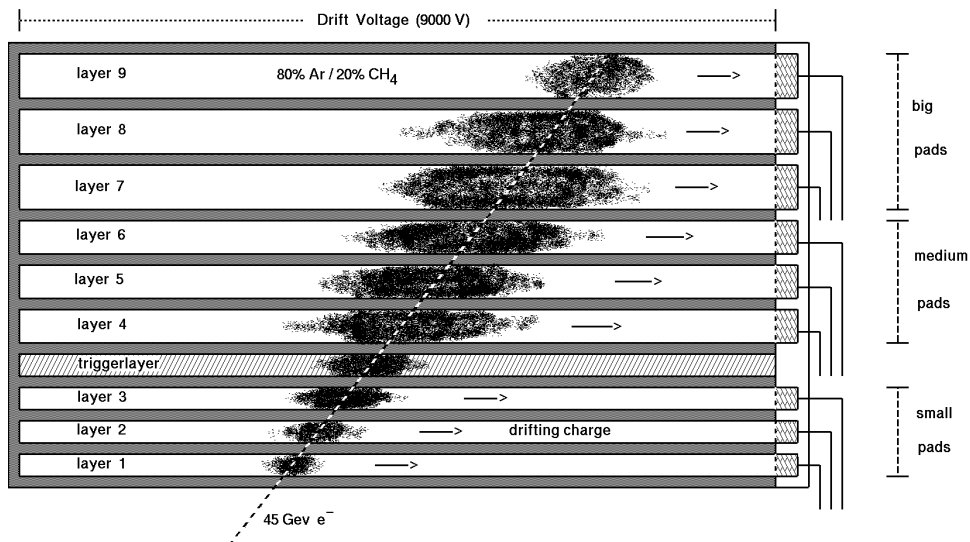
Figure 3.8 : A cross-section through the HPC, the barrel electromagnetic calorimeter of the DELPHI detector. The figure shows an electromagnetic shower produced by the passage of an electron through the detector.

Electromagnetic Calorimeters
These sub-detectors were used for energy measurement of photons and electrons. In the dense material of these detectors, photons with sufficient energy produced e^+e^- pairs. These secondary particles produced new photons by bremsstrahlung. The new photons again converted into e^+e^- pairs. This process continued until a shower of low energy electrons, positrons and photons was formed. These particles then deposited their energy in the material by ionization, absorption and other reactions. Electrons and positrons produced similar showers by initial bremsstrahlung in electromagnetic calorimeters (see Figure 3.8). Other particles, like hadrons and muons, flew through electromagnetic calorimeters without loosing a significant fraction of their energy.

High Density Projection Chamber (HPC)
HPC was an electromagnetic calorimeter in the barrel part of the DELPHI detector. It consisted of 144 modules arranged in a cylindrical layer between the radii of 208 and 260 cm. Polar angle coverage of this sub-detector was between $43°$ and $137°$. Each module of the HPC was a small TPC, containing lead layers separated by gas gaps. The lead wires, glued together,

were used as converters and they also provided the electric drift field in gas. Proportional gas chambers enabled a three dimensional reconstruction of charged tracks, as in the main DELPHI TPC. The total thickness of the converter was 18 radiation lengths in the radial direction. The energy calibration and alignment of HPC were performed by using electrons and positrons from $Z^0 \rightarrow e^+e^-$ decays and neutral pion decays, $\pi^0 \rightarrow \gamma\gamma$, reconstructed with high precision from one photon converted into an electron-positron pair before the HPC and the other photon detected in the HPC. The determined energy resolution of the detected photons in the HPC could be parameterised as [23]:

$$\frac{\sigma_E}{E} = \sqrt{(0.043)^2 + \frac{(0.32)^2 \text{ GeV}}{E}} \, . \tag{3.7}$$

The angular precision of the photon incident point was about 1 mrad in the azimuthal angle ϕ and 1.7 mrad in the polar angle θ.

Forward Electromagnetic Calorimeter (FEMC)

The FEMC consisted of two disks, each of them composed of 4532 lead glass blocks. The polar angle coverage of these two detectors was from $8°$ to $35°$ and from $145°$ to $172°$. The thickness of the blocks was 20 radiation lengths. The Čerenkov radiation emitted by the charged particles (see the beginning of the part on RICH Detector below) in the shower was read out by a photomultiplier for each block. The energy was measured with the following precision [23]:

$$\frac{\sigma_E}{E} = \sqrt{(0.03)^2 + \frac{(0.12)^2 \text{ GeV}}{E} + \left(\frac{0.11 \text{ GeV}}{E}\right)^2} \, , \tag{3.8}$$

where the last term is due to amplification noise.

Small Angle Tagger (SAT)/Small Angle Tile Calorimeter (STIC) and Very Small Angle Tagger (VSAT)

There were two electromagnetic calorimeters in the very forward region, used mainly for the luminosity measurement by counting Bhabha scattering events. Before 1994, the absolute luminosity was measured using the SAT detector, with acceptance between 43 and 135 mrad in θ. In 1994, the SAT was replaced by the STIC, which was a sampling lead-scintillator calorimeter formed of two cylindrical detectors placed on both sides of the detector at a distance of 2.2 m from the interaction point. It covered an angular region between 29 and 185 mrad in θ and had a relative energy resolution of 2.7% at 45.6 GeV.

The other very forward calorimeter, VSAT, was even closer to the beam, since it covered the polar angles between 5 and 7 mrad. Its modules were placed symmetrically around the beam pipe at a distance of ±7.7 m from the interaction point. Being closer to the beam, this detector counted more particles from Bhabha scattering and thus measured the luminosity with a smaller statistical error as STIC(SAT). On the other hand, VSAT was more sensitive to the background scattering processes, which increased the systematic error of the measurement. For this reason, VSAT was used to obtain relative luminosities at different energies, while the absolute value of the luminosity was measured by STIC(SAT).

Hadron Calorimeter (HCAL)
Hadrons interact with nuclei in the material predominantly via strong interactions. These reactions are not very likely to happen, since in lead the hadron average free path is around 19 cm. For this reason, hadrons mostly flew undetected through the entire material of the tracking system and even of the electromagnetic calorimeters. In order to detect them, large volume of relatively dense material had to be placed behind the electromagnetic calorimeters. The hadron calorimeter fulfilled these requirements and when hadrons reached this detector, the hadronic shower was formed, similar to the electromagnetic shower in HPC. Showers were almost completely absorbed in the detector. Muons on the other hand lost energy mainly through ionization and left therefore only a fraction of their energy in the calorimeter.

Hadron calorimeter was a sampling gas detector incorporated in the magnet yoke. It consisted of the barrel section and two end-caps and covered almost the full solid angle: $11° \leq \theta \leq 169°$. The HCAL consisted of streamer tubes, inserted in 1.8 cm slots between 5.0 cm thick iron plates of the return yoke of the DELPHI solenoid. Charge, released by ionization of the gas in streamer tubes, induced a signal on the cathode pads. Altogether, more than 19000 of streamer tubes were installed between $R = 3.20$ m and $R = 4.79$ m. They were arranged in 20 layers in the barrel region and 19 in the end-caps. The total thickness of the HCAL was 6 interaction lengths.

The electronic signal from streamer tubes did not depend on the amount of ionization produced by a charged particle. The energy was measured from the number of hits in different tubes, which of course was larger for hadronic showers than for penetrating muons. The calibration of the HCAL was performed using hadronic and dimuonic Z^0 decays. The precision of the energy measurement in the barrel region of the HCAL was found to be:

$$\frac{\sigma_E}{E} = \sqrt{(0.21)^2 + \frac{(1.12)^2 \text{ GeV}}{E}}\,, \tag{3.9}$$

where the fixed term in the expression was due to the material between the electromagnetic calorimeter and the hadron calorimeter [23].

3.2.4   Detectors for charged-particle identification

The identification of charged particles was based on the specific ionization loss per unit length (dE/dx) measured in the TPC, the information from the RICH detectors and Muon Chambers, and the energy deposition in HPC and HCAL. Some of the identification sub-detectors – TPC, HPC and HCAL – have already been described above, while the rest of them will be mentioned here.

Muon Chambers (MUC)
Muon chambers were used for detection and identification of muons. Since muons are supposed to be the only charged particles to penetrate even through the hadron calorimeter, muon chambers were installed on the outer side of the detector, behind all other sub-detectors.

Barrel Muon Chambers (MUB) consisted of three layers. Each of these layers was divided into 2 hemispheres with 24 azimuthal sectors. The innermost layer lay inside HCAL, at a radius

of 4.42 m, while the other two were installed on the outer side of HCAL, at the radii of 4.8 m and 5.15 m. In the radial direction, each layer was composed of two or three drift-chamber planes. Each drift chamber had a single anode wire in the centre and the cathode strips along z-axis on the inner walls. The $R\phi$-coordinate of the passing track was provided by the measurement of the signal on the anode wire. One of the cathode strips was used as a delay line for measurement of the z-position of the track. Forward Muon Chambers (MUF) were sub-detectors similar to MUB, placed in forward regions of the detector.

Surrounding Muon Chambers (MUS) covered the missing regions between MUB and MUF at a polar angle of about $45°$. In this way, the complete coverage of the muon detection system was assured for all polar angles between $20°$ and $160°$.

Ring Imaging Čerenkov Detectors (RICH)

The RICH sub-detector for the identification of charged particles was composed of the barrel (BRICH) and the forward (FRICH) part. Since the Barrel RICH [26], covering the barrel region of the DELPHI detector, was the most important sub-detector used for identification of kaons in this analysis, it is described a little more thoroughly. For more details on the Forward RICH which was operating on similar principles, the reader is referred to the literature [27].

Čerenkov radiation

Charged particle traversing a dielectric medium with a velocity exceeding the velocity of light in that material, produces a cone of Čerenkov light, as illustrated in Figure 3.9. The effect is a consequence of coherent polarization in the medium around a charged particle. The Čerenkov angle, θ_C, defined as the opening angle of the cone around the direction of charged particle, is a function of particle velocity $\beta = v/c$:

$$\cos \theta_C = \frac{1}{\beta n} \, , \tag{3.10}$$

where n is the refractive index of the material used as a radiator medium. The information on the charged-particle velocity β is obtained according to (3.10) from the measured Čerenkov

Figure 3.9 : The principle of the Čerenkov effect.

angle. Using the velocity together with the measured charged-particle momentum p, discussed in subsection 3.2.2, it is possible to identify a charged particle by calculating its mass:

$$mc^2 = pc\sqrt{\frac{1}{\beta^2} - 1} \,. \tag{3.11}$$

Additional information used for the identification of particles can be obtained from the number of emitted Čerenkov photons, which also depends on the particle's velocity [28]:

$$N_\gamma \propto 1 - \frac{1}{\beta^2 n^2} = \sin^2 \theta_C \,. \tag{3.12}$$

Naturally, the identification cannot be assured for the entire momentum range of the charged particles. Particles with velocities below the threshold velocity $\beta_{\mathrm{thr}} = 1/n$ do not cause the Čerenkov radiation. However, identification can be performed also below the Čerenkov threshold, based on the fact that for a given momentum some particles cause medium to radiate, while the others do not. This is called a *veto mode identification*, which substantially extends the momentum range of particle identification. Still, not even the veto identification can be performed in the low momentum region where several types are below the Čerenkov threshold, which finally sets the low limit on the identification momentum range. The upper identification limit of the momentum range is determined by the fact that with β approaching unity, Čerenkov angle converges towards its maximal value $\theta_C^{max} = \arccos(1/n)$. Once the difference in the expected angles for the two particles of different masses becomes smaller than the resolution of the measured Čerenkov angle, the separation of those two particles becomes impossible.

Barrel RICH (BRICH)

The barrel part of the DELPHI RICH was placed between the radii of 1.23 m and 1.97 m. The angular region covered by this detector was between $42°$ and $138°$. The BRICH consisted of two halves, divided by the plane including the interaction point. Each of the two halves was

(a)

(b)

Figure 3.10 : a) The sector of the barrel RICH detector, shown in the cross-section along the beam axis. b) Part of the barrel RICH, shown schematically. One half of the detector is shown, corresponding to the cross-section view depicted in a).

further divided into 24 sectors in $R\phi$ direction. A schematic view of the detector is shown in Figure 3.10.

In order to achieve a $\pi/\mathrm{K}/\mathrm{p}$ separation over a wide momentum range, two radiator media were combined in the RICH counters, one liquid and one gaseous. A particle emerging from the $\mathrm{e^+e^-}$ interaction point first crossed the boxes with liquid radiator $\mathrm{C_6F_{14}}$ of 1 cm thickness (see Figure (3.11)), placed near the inner radius of the barrel RICH. The refractive index of this radiating medium[8] was about 1.283, corresponding to the maximal Čerenkov angle of 39° and the momentum threshold of about 0.6 GeV for the charged kaons to radiate Čerenkov light (see Figure 3.12). The photons produced in the liquid radiator entered the 5 cm thick drift gas boxes, inside which they were converted into photoelectrons using a small addition of photosensitive vapour (TMAE) in the drift gas. Further on, charged particles flew through the gaseous radiator, placed on the outer side of the photon detector. As gaseous medium, $\mathrm{C_5F_{12}}$ was used, with the refractive index[9] around 1.00172, corresponding to the maximum Čerenkov angle of 3.36° and the threshold for $\mathrm{K^\pm}$ at about 8 GeV. Photons produced in gas were reflected back to the photo-detection plane by a set of parabolic mirrors near the outer wall of BRICH. The path travelled by photons in gas was 60 cm on average and thus long enough to enable the measurement of the Čerenkov angles in spite of their rather small values. Cones of Čerenkov light were observed as rings in the photo-detection plane. Produced photoelectrons drifted through the gas along the z-direction to the outer end, where they were detected by MWPC's. Combining the determined position in MWPC's with the measured drift time, the photon detector actually acted as a TPC, enabling a 3-dimensional reconstruction of the photon conversion point.
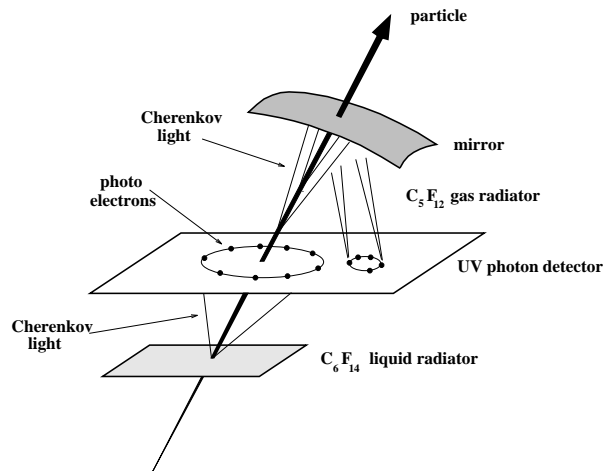
Figure 3.11 : Illustration of the barrel RICH detector's operation.

The response of the detector was tested with $\mathrm{Z^0} \rightarrow \mu^+\mu^-$ decays. Isolated muon tracks from such decays produced radiation at an angle which could not be experimentally distinguished from the saturated Čerenkov angle, for both liquid and gaseous radiators. From the distribution of single photon angles therefore the resolution of measured Čerenkov angles could

---

[8]The value of the refractive index is given for UV photons and for the operating temperature of $40\ ^\circ\mathrm{C}$ [26].

[9]See the previous footnote.

be determined. In case of above muons the average number of photons detected in liquid and gaseous medium of the barrel RICH detector were 14 and 9, with an achieved resolution of 13.5 and 4.5 mrad, respectively [28]. When the information from both radiators was combined, the particle identification capability for the barrel RICH detector was assured over the momentum range from ~ 0.7 GeV to ~ 25 GeV.

3.2.5 Charged-particle identification performance

Responses from various identification detectors were combined in order to obtain the best identification performance. The combination of the detectors used, depended on the type of particles that were to be identified. For the electrons, the information about the electromagnetic showers formed in the HPC was used together with the specific ionization measurement in the TPC. The latter measurement as a function of particles momenta is shown in Figure 3.12. Identification of muons, on the other hand, was achieved by the Muon Chambers, placed behind the
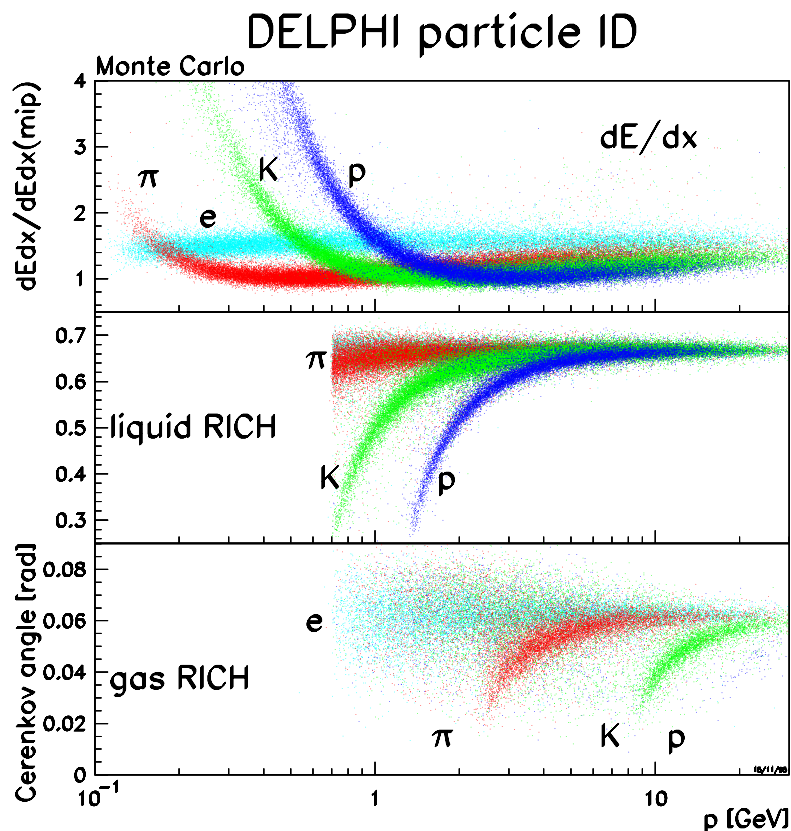
Figure 3.12 : Specific ionization measured by the TPC and Čerenkov angle as determined by the RICH detector [23]. The results are shown for electrons and different types of hadrons as a function of the particle momentum. Used particles corresponded to reconstructed tracks in a simulated sample of hadronic Z^0 decays.

Hadron Calorimeter which stopped the majority of hadrons and prevented them from entering the chambers.

Charged hadron identification was the most important feature of the DELPHI detector used in the described analysis. Standard hadron identification was performed using the specific ionization measurement in the TPC and the information from the RICH sub-detector. Specific ionization sampled by 192 anode wires in the TPC was compared to the expected detector response for different types of charged particles, as shown in Figure 3.12. The results of these comparisons were expressed as probabilities that the charged tracks corresponded to various types of hadrons. This measurement was compared to the identification information obtained by the measurement of the Čerenkov angle in the RICH. The Čerenkov angle as a function of the charged particle momentum is also shown in Figure 3.12, as determined for reconstructed tracks in a simulated sample of hadronic Z^0 decays. After combining the information from both sub-detectors described, the charged hadronic tracks were tagged as being pions, kaons or protons. Selection of hadronic tracks according to these tags, named traditionally as very loose, loose, standard and tight, provided samples of different purities obtained with different efficiencies. Tighter tags resulted in lower efficiency and higher purity, where the latter is defined as a fraction of correctly identified particles in the selected sample. The performance of the identification procedure can be demonstrated for selection of charged kaons. By identifying, for example, $K^\pm$ with the loose kaon tag, the sample of kaons with momentum above 0.7 GeV was selected with efficiency and purity of about 60%. For the tight kaon tag the efficiency dropped by 20%, while the contamination of the selected kaon sample was only about 20% [23].

In addition to these general identification capabilities, the performance of the kaon identification used in this analysis is discussed in more detail in the next Chapter.

3.2.6   Other sub-detectors

The remaining DELPHI sub-detectors are mentioned briefly in this subsection for the sake of completeness.

- **Time of Flight Counters (TOF)** were scintillator detectors positioned in the barrel region and were providing the signal for fast triggering and rejection of cosmic rays. In the forward region the same task was performed by the Forward Hodoscope or Horizontal Flight Tagger (HOF).

- **Phi-, $90°$- and $40°$-Taggers** were supplementary lead-scintillator counters used for coverage of cracks, gaps and holes between various modules of electromagnetic detectors. In this way an almost complete hermeticity of the detector was obtained.

3.2.7   Trigger and data flow

The aim of the triggering system is to select physically interesting events which are then written on magnetic tape. The DELPHI trigger system [29] was composed of four successive levels, named T1, T2, T3 and T4. The first two levels, T1 and T2, were synchronized with respect to the Beam Cross Over (BCO), while the last two, T3 and T4, were software filters performed

asynchronously with respect to the BCO. The bunch crossing interval for LEP was 22 μs (11 μs), corresponding to 4 (8) bunches of electrons and positrons in the collider. The trigger decisions for T1 and T2 were taken in 3.5 μs and 39 μs, respectively, implying that after each positive T1 decision 1 or 3 consecutive BCO's were lost, depending on the number of bunches. The action of the two hardware triggers thus introduced a dead time of about 2%.

- **T1** decision was based solely on information from detectors with the fast read-out, such as: ID, OD, FCA, FCB, TOF, HOF, MUB and HPC scintillators. No correlation between different sub-detectors was demanded for the decision. At a typical luminosity of $1.5 \cdot 10^{31}$ cm^{-2}s^{-1}, the normal T1 trigger rate was 700 Hz.

- **T2** decided also on the information from the slow drift sub-detectors, such as TPC, HPC and MUF. The second trigger level also demanded the correlation between responses of different sub-detectors. After the positive T2 decision the acquisition of data collected in various sub-detectors was done. The typical rate of the second level trigger was 4.5 Hz.

- **T3** simply refined the T2 trigger procedure by using more detailed information available from the sub-detectors. The rate of T2 was typically cut in half at this level.

- **T4** was based on the modified DELPHI tracking algorithm and rejected events without tracks pointing to primary interaction point or events without significant energy deposits in the calorimeters. Typical T4 triggering rate was 1 Hz.

According to the estimations, the trigger efficiency for multi-hadronic and leptonic events was very close to 100%. This meant that at the final rate of 1 Hz the stored data included practically all the hadronic Z^0 events with the rate of 0.5 Hz, and resulted in about 50% purity in terms of events interesting for physics analyses.

The Data Acquisition System (DAS) sent from the detector cavern to the surface all the events triggered at the T4-level. These events were then written to a disk or magnetic tapes in a so called "raw-data" format. The off-line analysis was then performed in order to make the final reconstruction. The central part of this processing was done by the DELANA analysis package [30], which performed calibrations, pattern recognition and track fitting. Some standard particle identification algorithms were also performed at this stage. The output of DELANA, a Data Summary Tape (DST), included information which could then be used for specific physics analyses. However, for some sub-detectors an additional fine tuning and calibration was performed at the level of the DST, correcting for possible unexpected effects not taken into account during the DST production (see for example [31]).

3.2.8 Detector simulation

Simulated data containing predicted values of theoretical parameters, are used for the interpretation of the measured results obtained by various analyses. Also, comparisons between the measured data and the simulation are usually done when different experimental methods and their limitations are studied and when various systematic errors of measurements are estimated. For these reasons, simulated data have to be produced in such a way, that the obtained events

are as close as possible to the real data. The DELPHI simulation package DELSIM [32] was based on the production chain, composed of three stages:

- Event generators [33] were used to generate events arising from the physical processes expected at LEP1 energies. The hard process, such as $e^+e^- \rightarrow (\gamma, Z^0) \rightarrow q\overline{q}$, was generated in the first step. Parton showers were formed in the next step, followed by a subsequent fragmentation of partons into hadrons. Produced mesons and baryons were finally let to decay into stable particles. The events for the presented analysis were generated with JETSET 7.4 Parton Shower model [34]. Various parameters, such as branching ratios for different decays, particles masses and their decay times, were determined experimentally and used in the generator. Since some of these parameters were not very well known, the phenomenological procedure based on many additional tunable parameters was applied. These parameters of the generator were adjusted to match the measured DELPHI data [35].

- In the second stage of the simulation procedure, the produced particles were tracked through all the components of the DELPHI detector. In order to describe physical processes in the detector, the DELSIM programs included the descriptions of the detector material as well as the parameters of the magnetic field.

- In the last stage of the procedure, the responses of all sub-detectors were determined according to all particles created in the detector at the previous stage. The output, estimated separately for each of the sub-detectors, was given in the form of the obtained electronic signals. The signals from various detector components were then used to produce the file in a "raw-data" format, which was processed by DELANA in exactly the same way as the measured data.

4

Sample selection

The analysed data were collected by the DELPHI detector at the LEP1 storage ring in the years 1992 to 1995. During the four years LEP operated at energies near the Z^0 peak. In 1993 and 1995 data were also taken at about 2 GeV above and below the energy corresponding to the nominal mass of the Z^0 boson, i.e. at the so-called "peak$\pm$2" points. In total, the collected data correspond to the integrated luminosity of 138.5 pb^{-1} [36], as listed in Table 4.1.

Year	$\sqrt{s}$ [GeV]	$\int \mathcal{L}dt$ [pb^{-1}]
1992	91.28	24.1
1993	89.43	9.7
	91.22	16.6
	93.02	10.0
1994	91.20	46.3
1995	89.44	8.4
	91.30	13.8
	92.97	9.5

Table 4.1 : Integrated luminosities for the data collected by the DELPHI detector between years 1992 and 1995, shown together with the average centre-of-mass energies, $\sqrt{s}$. Compare the collected luminosities with the ones delivered by the LEP collider and listed in Table 3.1.

4.1 Hadronic event selection

At the preselection stage, candidates for the hadronic decays of Z^0 bosons, $Z^0 \rightarrow q\overline{q}$, were selected from the recorded data in the following way. An event was chosen as a hadronic-decay

candidate if there were tracks of at least 5 charged particles detected and if the total measured energy of the charged particles (all of them were assumed to be pions) exceeded 30 GeV. The particles were reconstructed from the tracks in the DELPHI tracking detectors that met the requirements listed in Table 4.2.

charged particle momentum	$>$	0.4 GeV
error of the momentum measurement	$\leq$	10 GeV
relative momentum uncertainty	$\leq$	150 %
length of tracks measured with TPC	$\geq$	30 cm
polar angle for charged particles	between	$15°$ and $165°$
impact parameter relative to interaction point:		
projection in the $R\phi$-plane	$\leq$	10 cm
projection in the z-direction	$\leq$	20 cm

Table 4.2 : Requirements for the selection of well measured tracks.

Altogether 3 million hadronic events were selected from the 1992–1995 data at centre-of-mass energies in the range of about ± 2 GeV around the nominal Z^0 mass (see Table 4.3). According to the simulation, the efficiency of the selection was about 86% for hadronic Z^0 decays. The remaining background from τ events, $\gamma\gamma$ events, Bhabha events and background from beam-gas and beam-wall interactions contributed less than 0.5% to the preselected sample and was found to be negligible for this analysis.

The simulated sample used in the analysis consisted of 12.4 million simulated hadronic events for the years 1992 to 1995 (see Table 4.3). The events $\mathrm{e^+e^-} \to \mathrm{q\overline{q}}$ were generated and processed as described at the end of the previous Chapter.

The number of the hadronic decay candidates was further reduced by limiting the polar angle θ_T of the *thrust axis* of the selected events, to the barrel region of the detector ($|\cos\theta_T| < 0.7$). The event thrust axis is the unit vector $\mathbf{n}_T$, for which the maximum of *thrust* is attained:

$$T = \max_{\mathbf{n}_T} \left\{ \frac{\sum_{i=1}^{N} |\mathbf{n}_T \cdot \mathbf{p}_i|}{\sum_{i=1}^{N} |\mathbf{p}_i|} \right\} , \tag{4.1}$$

with the sum running over all detected particles (charged and neutral) in the event. The requirement is necessary due to the limited angular acceptance of the Vertex Detector, essential for the selection of $Z^0 \to \mathrm{b\overline{b}}$ decays (see below).

4.2 $\mathrm{b\overline{b}}$ enrichment of the sample

For the measurement of $A_{FB}^{\mathrm{b\overline{b}}}$ it is necessary to separate the $Z^0 \to \mathrm{b\overline{b}}$ decays from other hadronic Z^0 decays. This separation can be done by a so-called b-tagging, an experimental technique

	MEASURED DATA		SIMULATED DATA	
Year	$\sqrt{s}$ [GeV]	No. of events	$\sqrt{s}$ [GeV]	No. of events
1992	91.28	604493	91.25	2310113
1993	89.43	83122	89.40	269026
	91.22	405483	91.25	1947842
	93.02	115673	93.00	339528
1994	91.20	1208082	91.25	5568447
1995	89.44	73108	89.43	268898
	91.30	397988	91.25	1250493
	92.97	115217	93.01	423237
92-95	89.43	156230	89.42	537924
	91.24	2616046	91.25	11076895
	92.99	230890	93.01	762765

Table 4.3 : Numbers of selected candidates for hadronic decays of Z^0 for measured data and the entire set of simulated hadronic data for different periods of data taking. The average centre-of-mass energy, $\sqrt{s}$, for each of the periods is also shown.

based on unique properties of b$\overline{\text{b}}$ events. A method called b-confidence [37] was used in this analysis, exploiting several characteristic properties of B hadrons, contained in b jets.

The main characteristics of B hadrons are their relatively long lifetimes, which on average are about 1.6 ps [13]. Long lifetimes of B hadrons, accompanied by their large masses and large fractions of the event energy taken by these particles result in larger impact parameters of particles produced in decays of B hadrons. The impact parameter is defined as a minimum distance between a track and the reconstructed primary vertex. The sign of the track impact parameter is defined according to the direction of the jet to which the given track belongs: it is positive when the angle between the jet direction and the vector pointing from the primary vertex to the point of closest approach, is less than $90°$ (see Figure 4.1). With this definition, the tracks from the decays of B hadrons have positive impact parameters. On the other hand, tracks from the primary vertex have impact parameters which are different from zero only due to the track extrapolation error and the error on the reconstructed position of the primary vertex. Such impact parameters usually have much smaller values, symmetrically distributed around 0. The significance of the impact parameter d, which is defined as the ratio between the track impact parameter and its measurement error, $S_d = d/\sigma_d$, can then be used to classify tracks from different quark decays, as it can be seen in Figure 4.2.

Apart from the impact parameters, the improved b-tagging method [37] used in this anal-
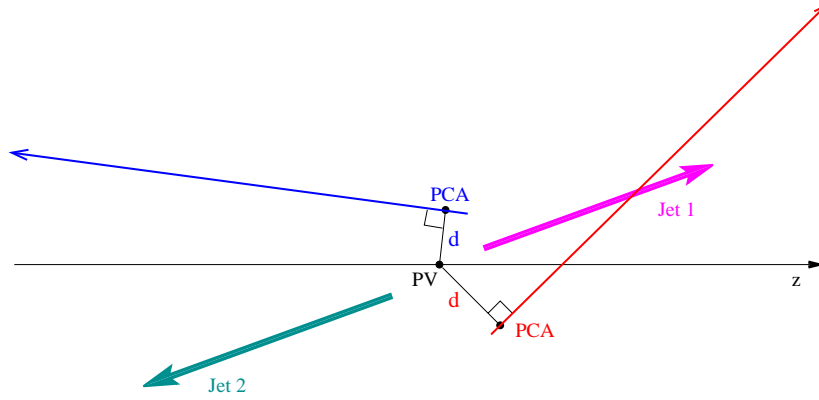
Figure 4.1 : The definition of the track impact parameter, illustrated by an example with two tracks. The right track, belonging to Jet 1, has positive impact parameter d, while the negative impact parameter d is assigned to the track belonging to the Jet 2. The abbreviations PV and PCA denote the primary vertex and a point of closest approach to the primary vertex, respectively.

ysis also exploits the fact that tracks from the decays of B hadrons have higher momenta and significant angles between the track momenta and the b-quark jet direction. Distributions of the three variables are combined in a probabilistic variable, b-confidence, used for determining a probability that an observed track comes from a b-quark jet. At certain values of the impact parameter significance S_d, of the track momentum p and of the angle ψ between the track and the jet, this combined variable reads

$$\mathcal{P}^{\mathrm{b}}(S_d, p, \psi) = \frac{f^{\mathrm{b}}(S_d, p, \psi)}{f^{\mathrm{b}}(S_d, p, \psi) + f^{\mathrm{c}}(S_d, p, \psi) + f^{\mathrm{uds}}(S_d, p, \psi)}\,. \tag{4.2}$$

The fractions

$$f^{\mathrm{b}}(S_d, p, \psi) = \frac{N^{\mathrm{b}}(S_d, p, \psi)}{N^{\mathrm{b}}_{\mathrm{total}}}\,,\ \ f^{\mathrm{c}}(S_d, p, \psi) = \frac{N^{\mathrm{c}}(S_d, p, \psi)}{N^{\mathrm{c}}_{\mathrm{total}}}\ \text{and}\ f^{\mathrm{uds}}(S_d, p, \psi) = \frac{N^{\mathrm{b}}(S_d, p, \psi)}{N^{\mathrm{uds}}_{\mathrm{total}}}$$

were determined from the simulated data. $N^{\mathrm{b}}_{\mathrm{total}}$, for example, denotes the total number of tracks in a sample of simulated $\mathrm{b\overline{b}}$ decays of Z^0 bosons, while $N^{\mathrm{b}}(S_d, p, \psi)$ is the number of the tracks with certain values of the track-parameter significance S_d, of the angle ψ and of the momentum p. The probabilities (4.2) for all the observed particles in an event are combined in a single separating variable, event b-confidence $\mathrm{b_{conf}}$:

$$\mathrm{b_{conf}} = \frac{\displaystyle\prod_j \mathcal{P}^{\mathrm{b}}_j}{\displaystyle\prod_j \mathcal{P}^{\mathrm{b}}_j + \prod_j \mathcal{P}^{\mathrm{c}}_j + 3 \cdot \prod_j \mathcal{P}^{\mathrm{c}}_j}\,. \tag{4.3}$$

Here, index j runs over different tracks in an event. The values of the separating variable are concentrated close to unity for $\mathrm{b\overline{b}}$ events, while non-$\mathrm{b\overline{b}}$ events tend to have smaller values of

Impact parameter significance
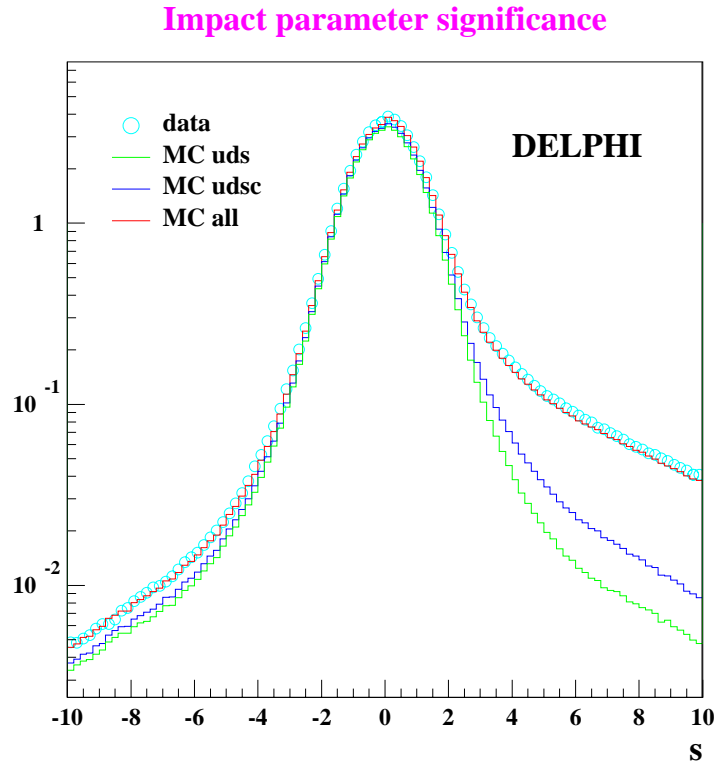
Figure 4.2 : The distribution of the impact parameter significance is shown for measured data and for the different contributing quarks in the simulation [38]. bb̄ content becomes dominant at large positive values of significance.

b_{conf}, as can be seen in Figure 4.3. The spike at the event b-confidence of 0.2 is caused by events without any tracks usable for b-tagging.

For a selected event to be tagged as a $Z^0 \rightarrow b\bar{b}$ candidate, the value of b_{conf} had to exceed a certain minimum value. Different minimum values were set for data collected during different years of LEP1 in order to optimize the tagging in terms of significance of the measured asymmetries (see the discussion in Section 4.4 and Table 4.4 for the list of selected cut values). On average, the efficiencies of the b-tagging used in the analysis were around 60% and purities over 90%. A diagram illustrating the relationship between efficiency and purity as obtained by the simulation of 1994 data is shown in Figure 4.4.

4.2.1 Background estimation

The only important source of background in the sample selected by requiring a certain minimum value of the event b-confidence, is due to the non-bb̄ decays of Z^0. The fraction of such events in the selected sample was estimated using the simulated $e^+e^- \rightarrow q\bar{q}$ data. The estimated background contribution was then subtracted from all the measured distributions. For example, a distribution of the bb̄ events with respect to an arbitrary variable x was obtained from the
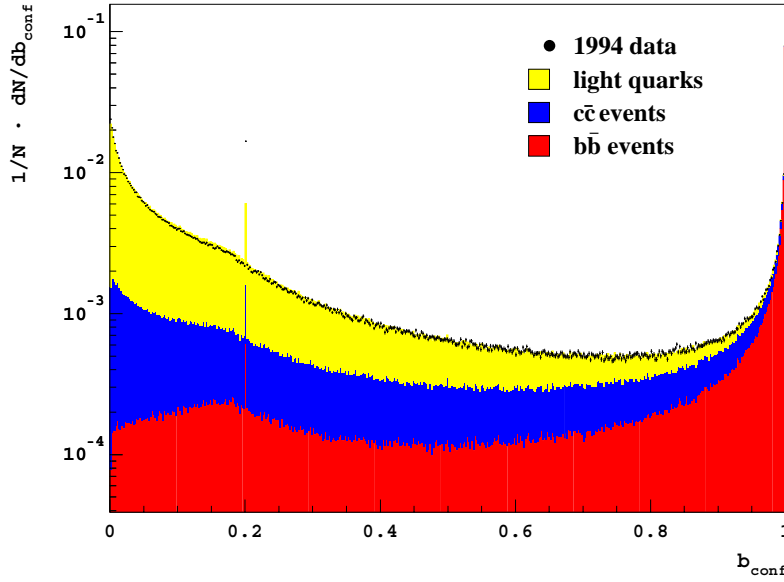
Figure 4.3 : Distribution of the normalized number of measured events versus the separating variable b_{conf}, compared to the simulation. A spike at the value $b_{conf} \simeq 0.2$ is due to events with no tracks that can be used for the b-tagging.

measured distribution as:

$$\frac{dN_{b\bar{b}}}{dx} = \frac{dN_{meas}}{dx}\left[1 - f_{bkg}(x)\right] , \tag{4.4}$$

with the background fraction estimated from the selected simulated data:

$$f_{bkg}(x) = \frac{N_{MC,sel}^{bkg}(x)}{N_{MC,sel}(x)} .$$

Small uncertainties of background estimations due to finite samples of the simulated data were taken into account together with the statistical errors of the measured data.

4.3   Identification of charged kaons

The momentum interval of charged kaons with the ability of tagging the charge of b quarks ranges mainly between 2 and 15 GeV (see section 4.4 below). The most important component of the DELPHI detector that provides identification of such kaons is the barrel RICH. The identification information obtained by the barrel RICH was combined with the measurements of the specific ionization in the TPC, the latter being of a significant importance mainly for the identification of low momentum hadrons.

To combine these two pieces of information for the data taken by the DELPHI detector in 1992 and 1993, the HADSIGN [23] algorithm was applied in the way already mentioned
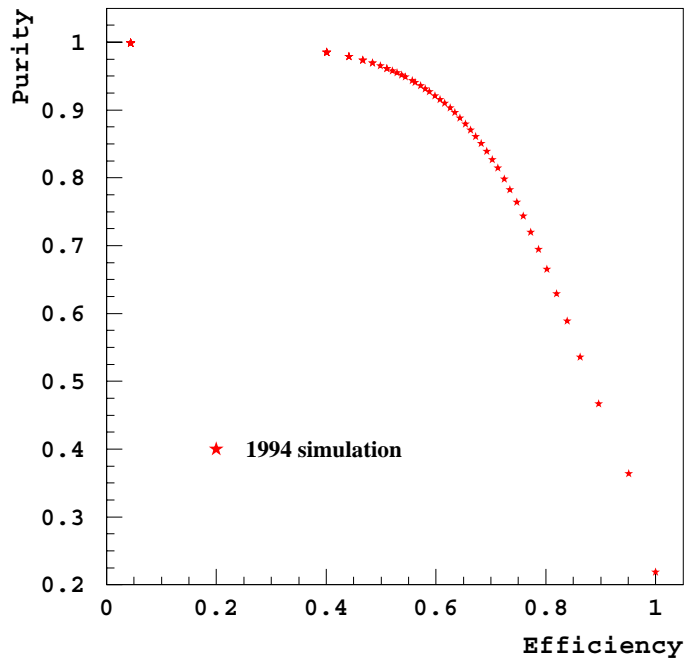
Figure 4.4 : Efficiency of the b-tagging method versus purity of the sample tagged. The diagram is obtained for the 1994 simulated sample.

in the particle identification section of the previous chapter. For the data taken in 1994 and 1995, representing the major part of the measured data, the MACRIB [39] package was used for the kaon identification. Namely, besides the HADSIGN algorithm there exists another algorithm for interpretation of the RICH data, called RIBMEAN [40]. Since the two identification methods sometimes give complementary results, MACRIB benefits by taking both of them simultaneously into account. However, since the two basic algorithms are also highly correlated, the available information was combined using a neural network. Apart from the mentioned two algorithms, the decision of the network was based upon many additional pieces of information, such as: the information from the Outer Detector, the muon identification flag, the information about the electron identification [41], etc. The neural network provided a single output variable in the interval between -1 and $+1$, which was then used for the kaon identification (see Figure 4.5). The performance of the MACRIB kaon identification was studied on the simulated data by selecting only tracks above different minimum values of the network output. In this way, the efficiency and purity for MACRIB identification were determined, shown in Figure 4.6 for all tracks with the momentum above 0.7 GeV. By studying the simulated sample it was also established that the MACRIB identification gives up to 20% better efficiency at the same purity when compared to the HADSIGN algorithm.
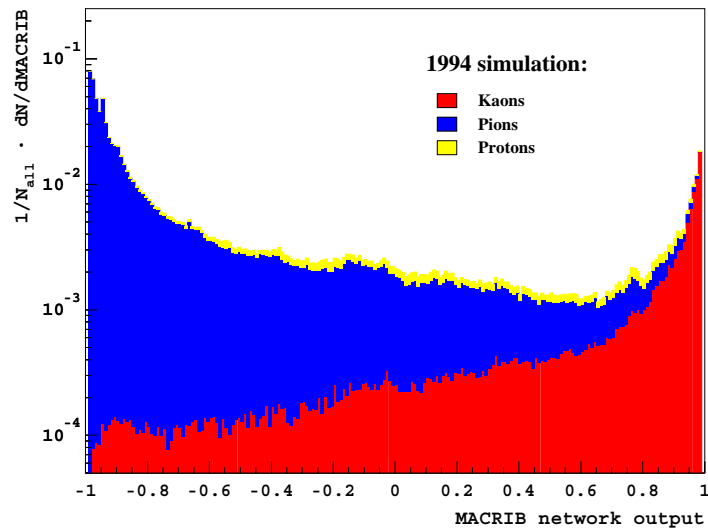
Figure 4.5 : The distribution of the MACRIB neural network output for 1994 simulated $\bar{q}q$ data. The network output is shown for hadronic charged tracks (kaons, pions and protons) with the momentum above 0.4 GeV. Note the logarithmic scale on y-axis.
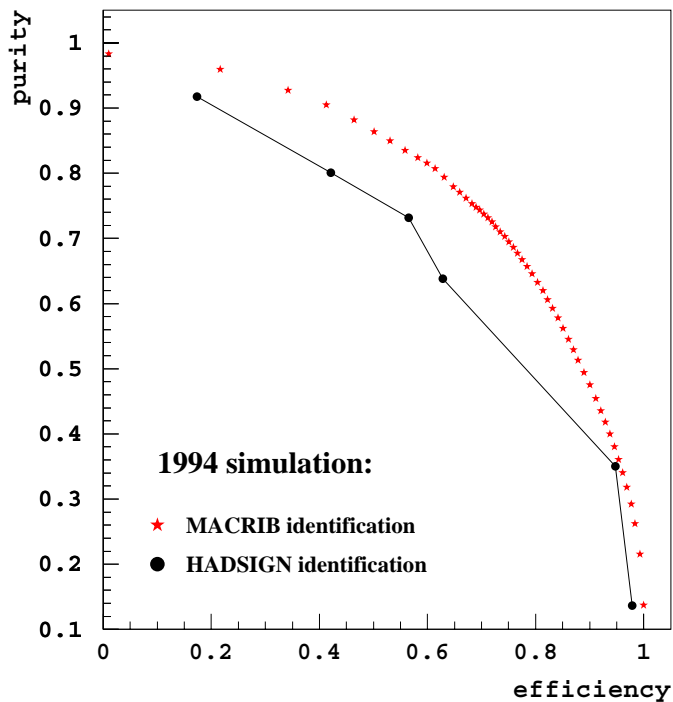
Figure 4.6 : Efficiency vs. purity for both kaon identification methods used in the analysis. The results for 1994 simulated sample is shown, where only the tracks with the momentum above 0.7 GeV were used.

For the analysis, the kaon identification working point was chosen in such a way, that the purity for the studied 1994 simulated sample was around 60%. For the HADSIGN algorithm this corresponds to the loose kaon tag, while in the case of the MACRIB identification all tracks above the minimum value of the neural network output of 0.225 were taken into account. Only charged tracks detected in the barrel region of the DELPHI detector were used, since this region is covered by the barrel RICH counters, allowing for a powerful hadron identification. The barrel region was chosen also because it roughly coincides with the region covered by the Vertex Detector, essential for the b-tagging technique, as already mentioned before.

4.4 Separation of kaons from weak B-hadron decays

After selecting the sample of hadronic Z^0 decays enriched with $\mathrm{b\overline{b}}$ events and subtracting the non-$\mathrm{b\overline{b}}$ background, we can determine the number of kaon candidates produced exclusively in $\mathrm{b\overline{b}}$ events. However, apart from kaons, produced in weak decays of B hadrons, there are also charged kaons coming from the primary vertex. These kaons arise in the process of hadronisation of primary quarks from $\mathrm{Z}^0 \rightarrow \mathrm{b\overline{b}}$ decays or in decays of excited B hadrons, e.g. $\mathrm{B}_s^{**} \rightarrow \mathrm{B}^*\mathrm{K}$. Since the power of these kaons to tag the charge of b quarks is smaller than the tagging power of kaons from weak B decays, special kinematical properties were used to separate the two classes of kaon candidates. Conveniently, these kinematical properties can be used to classify all charged particles, observed in $\mathrm{b\overline{b}}$ events, which allows the classification of kaon candidates to be practically independent on the purity of the selected kaon sample. In other words, the separating procedure is applicable to all kaon candidates, even if these are misidentified pions or protons instead of true kaons.

There are various differences between the two groups of charged particles mentioned above. Some of them were already exploited for the b-tagging, described in section 4.2. For instance, tracks coming from B hadrons can be distinguished by large impact parameters with respect to the primary vertex and by substantial angle with respect to the jet containing B hadrons [37]. In addition, due to the hard momentum spectra of B hadrons, particles from B-hadron decays are distinguished also by higher momenta and by larger values of track rapidity, the latter being defined as:

$$y = \frac{1}{2} \ln \left(\frac{E + p_L}{E - p_L} \right) , \tag{4.5}$$

where E is the track energy and p_L is the momentum component along the reference axis, i.e. along the direction of the jet containing the B hadrons.

The mentioned separating variables are only a part of a set of 11 variables, used to separate tracks coming from the secondary vertices of weakly decaying B hadrons from those coming from the primary vertices [42]. The variables were used as an input to the B-track Neural Network, taking in this way correlations between different input variables automatically into account. The output of the network was a single separating variable which could then be used for an efficient reduction of the primary-vertex background contribution to the sample of selected kaon candidates. The network is incorporated in the BSAURUS, a package for B-physics analyses of Z^0 events [42].
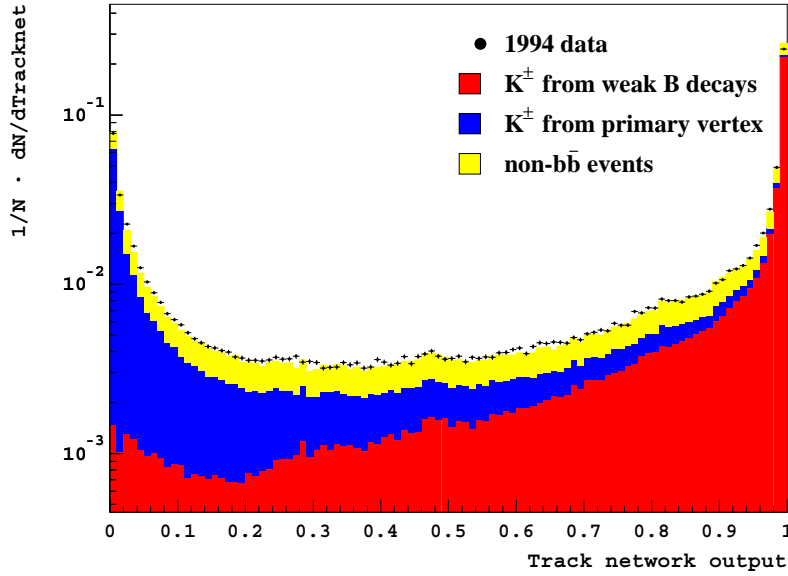
Figure 4.7 : Comparison between data and simulation of the track neural network performance for reconstructed tracks of kaon candidates. Measured data for 1994 and a simulated sample are shown, both selected with a minimum value of $b_{conf} = 0.7$. The simulated sample is divided into subsamples: kaons from weak B-hadron decays, kaons from the primary vertex and non-$b\bar{b}$ background contribution. Note the logarithmic scale on y-axis.

All input variables to the track neural network are listed and their individual distributions were studied in ref. [42]. We studied the performance of the neural network on a sample of selected simulated kaon candidates and the obtained distribution of the network output variable is shown in Figure 4.7. From the plot it can be inferred that the neural network output approaches unity for tracks coming from a secondary vertex, while it is peaked at zero for tracks which originate from the main interaction point.

Only kaons with the output value of the track neural network above a certain minimum value were considered. The minimum value of the network output, and consequently the kaon selection efficiency, depends on the purity of the selected sample of the $b\bar{b}$ candidates. For this reason, the cut value on the net output, and the minimum value of the variable b_{conf} used to select $b\bar{b}$ candidates among the hadronic Z^0 decays (see Section 4.2), were set simultaneously so as to maximize the *significance* of the kaon asymmetry A^K_{FB}. The significance is defined as the ratio between the asymmetry and its statistical error:

$$S = \frac{A^K_{FB}}{\sigma_{A^K_{FB}}} \ . \tag{4.6}$$

The maximization of significance was done on the simulated sample. The value of asymmetry and its statistical error were calculated for various minimum values of neural network output and b_{conf}. The maximum of calculated significance was then determined for each year

Year	b_{conf} cut	b-efficiency	b-purity	Track neural network cut
1992	0.94	55.5 %	89.9 %	0.84
1993	0.94	56.9 %	89.4 %	0.84
1994	0.94	62.1 %	90.6 %	0.84
1995	0.98	52.6 %	95.3 %	0.7

Table 4.4 : Minimum values required for b_{conf} of selected events and for the output of the track neural network for the selected kaons. The estimates for the efficiencies of the applied b-tagging and for the $b\overline{b}$ purities of the selected samples are also shown.

of data taking. The corresponding cut values obtained in this way are given in Table 4.4. Since the obtained cut values do not change much from one year to another, the cut values used in the analysis were the same for the first three years of data taking, while there was a small difference for 1995. The difference was due to different operating conditions of some sub-detectors for 1995. An example of determination of the significance maximum is shown in Figure 4.8 for the sample of 1994 simulated data.

Similarly, the significance dependence on the required minimum value of selected-kaon momenta was also checked for different data taking periods. It was determined, that the cut value of 2.0 GeV can be used for all years.

The final data sample was obtained by selecting $b\overline{b}$ candidates with at least one kaon meet-
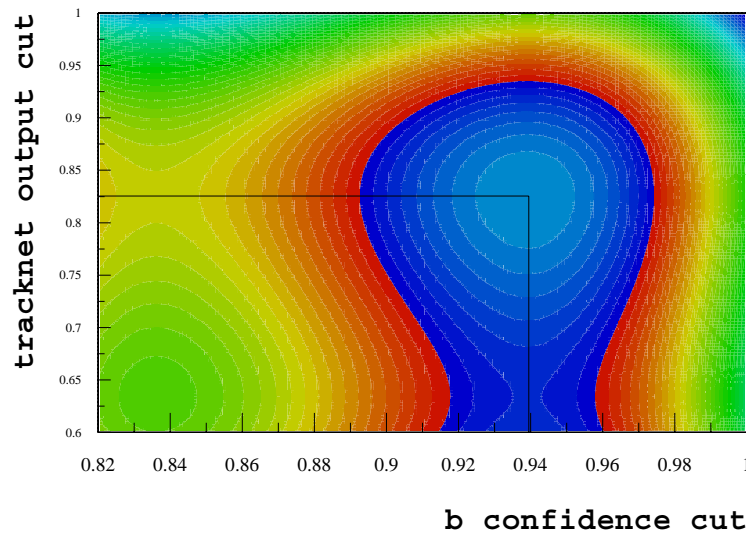
Figure 4.8 : Smoothed-significance contours for $A_{FB}^{b\overline{b}}$ as functions of the minimum values required for the b_{conf} variable of hadronic events and the output of the track neural network for the selected kaons. The example is shown for the 1994 simulation.

Year	$\sqrt{s}$ [GeV]	N_K	non-b$\overline{\text{b}}$ contamination
1992	91.28	37572	8.8%
1993	89.43	6097	9.4%
	91.22	26462	9.4%
	93.02	8716	9.4%
1994	91.20	96436	8.7%
1995	89.44	2128	4.6%
	91.30	22025	4.6%
	92.97	3556	4.6%

Table 4.5 : The selected events with at least one track of a charged particle passing the requirements for kaons used for tagging the charge of b quarks.

ing all the described requirements. The number of such events is shown in Table 4.5. A measured and a simulated momentum spectrum of selected kaons in the final sample of the 1994 data are shown in Figure 4.9, while plots for the entire data set are displayed in Appendix B.1.
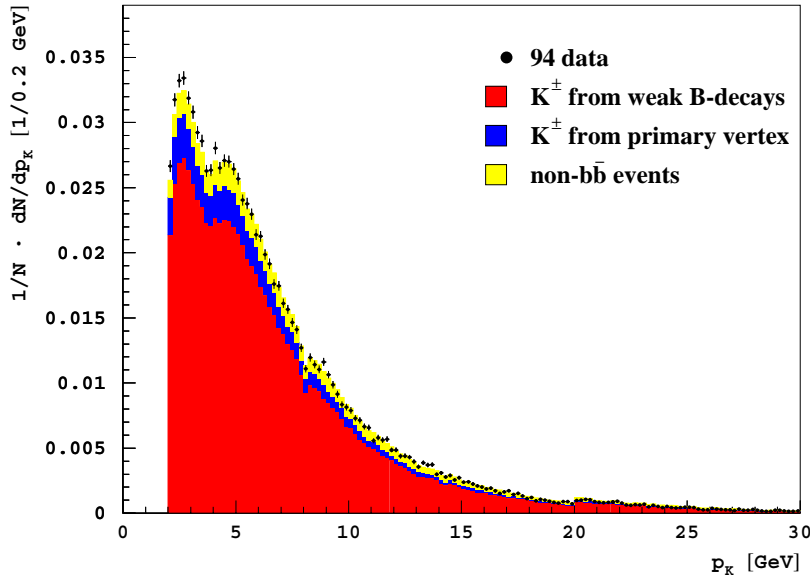
Figure 4.9 : Momentum spectrum of selected kaons from measured (dots with errors bars) and from simulated (filled histograms) b$\overline{\text{b}}$-decay candidates passing the selection criteria described in the text. Normalized distributions, corresponding to the 1994 data, are shown.

5

Data analysis

5.1 Asymmetry of charged kaons

For the purpose of tagging the charge of a b quark in a selected $Z^0 \to b\bar{b}$ decay candidate, only a charged kaon with the highest output value of the track neural network in the event was used. To the selected kaon the nearby thrust polar angle θ_T was attributed, i.e. the kaon momentum was required point in the same hemisphere as the thrust axis, with the two hemispheres in an event being defined by a plane perpendicular to the thrust axis. The procedure of this attribution is clean since there are virtually no ambiguous candidates, produced in the direction close to the plane separating the two hemispheres, as shown in Figure 5.1.a. Since the thrust axis coincides to a very good approximation with the momentum direction of the original quark pair (see Figure 5.1.b), the thrust polar angle was used to define the b-quark direction: $\theta_T = \theta$. In other words, attributing the thrust polar angle θ_T to the selected kaon in the described manner is equivalent to tagging the charge of the quark produced at the polar angle θ. The selected tag-
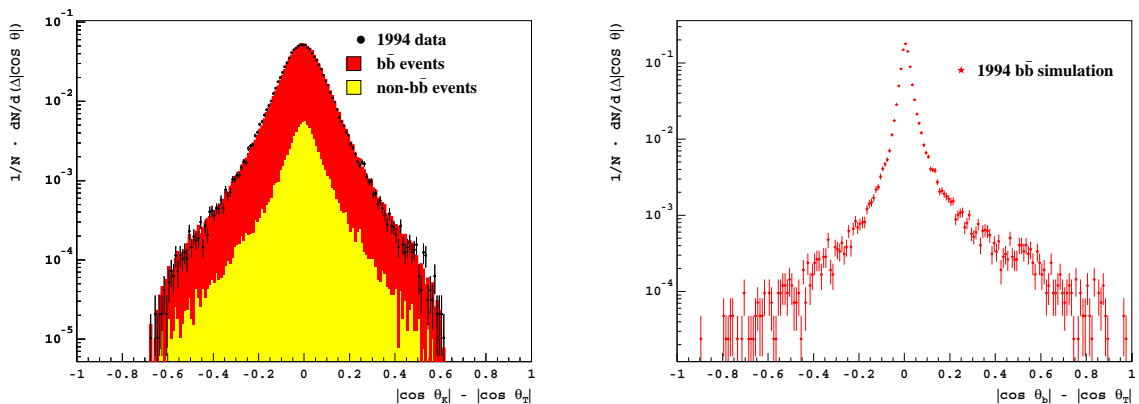
Figure 5.1 : Normalized distribution of the difference between: a) the selected kaon direction and the event thrust axis and b) the quark direction and the thrust axis. Both plots are done for the sample of events, belonging to the 1994 simulated dataset. In the case of kaon candidates the simulated distribution is shown in comparison to the measured one. Note the logarithmic scale in y-axis.

61

ging kaons were used for the measurement of the charged-kaon asymmetry. Measured angular distributions of selected negative and positive kaon candidates for the 1994 data are shown in Figures 5.2.a and 5.2.b, respectively. The figures for other years of data taking are collected in Appendix B.2. The fraction of non-$b\overline{b}$ events in the selected samples was estimated from the MC simulation and the estimated background contributions were subtracted from the measured distributions.

Having the background contribution to the sample of selected kaons subtracted, the observed forward-backward asymmetry for the selected charged kaons in $b\overline{b}$ decays given at a certain value of the thrust polar angle θ reads:

$$A_{\mathrm{K}}^{\mathrm{obs}}(\theta) = \frac{N_{\mathrm{K}^-}(\theta) - N_{\mathrm{K}^+}(\theta)}{N_{\mathrm{K}^-}(\theta) + N_{\mathrm{K}^+}(\theta)} \, . \tag{5.1}$$

The charged-kaon detection efficiency is expected to cancel out in ratio (5.1). Measured charged-kaon asymmetry for the 1994 data is shown in Figure 5.2.c, while plots for all datasets are collected in Appendix B.3. Note that the central region of the polar angle interval $-0.05 \leq \cos\theta \leq 0.05$ was excluded from all plots and calculations to avoid additional effects due to interactions in the central high voltage TPC plate.

There is a shift of measured asymmetry towards negative values, i.e. measured asymmetries in Appendix B.3 look to be more negative than positive. The shift in asymmetry which is of the order of 1 %, implies that there are altogether more positive kaon candidates detected than negative ones. Since the production rate and the kaon detection efficiency do not depend on the kaon charge, the difference in numbers of kaons can only be attributed to different behaviour in the detector. This effect, referred to as the *material asymmetry* is a consequence of the fact that the cross-section for interactions of negative kaons with the material in the detector is larger than the cross-section for the positive kaons [13]. Since it is more likely for a K^- than for a K^+ to interact in the detector material before reaching the particle identification devices, the original kaon asymmetry coming from the $b\overline{b}$ asymmetry is therefore distorted (see equation (A.14)).

The magnitude of material asymmetry for the selected sample of kaon candidates was estimated from the measured data. The estimation was done by constructing the ratio:

$$A_{\mathrm{K}}^{\mathrm{mat}}(\theta) = A_{\mathrm{K}}^{\mathrm{mat}}(\pi-\theta) = \frac{\left(N_{\mathrm{K}^+}(\theta) + N_{\mathrm{K}^+}(\pi-\theta)\right) - \left(N_{\mathrm{K}^-}(\theta) + N_{\mathrm{K}^-}(\pi-\theta)\right)}{N_{\mathrm{K}^+}(\theta) + N_{\mathrm{K}^+}(\pi-\theta) + N_{\mathrm{K}^-}(\theta) + N_{\mathrm{K}^-}(\pi-\theta)} \, . \tag{5.2}$$

The above equation is based on the assumption that the effect of the material is forward-backward *symmetric*. This is a justifiable assumption, since the detector was built in such a way and possible differences between the material in forward and backward hemispheres should be negligible. This is also confirmed in ref. [43], where the material asymmetry of kaons from $s\overline{s}$ events was explicitly measured. A distribution of the material asymmetry (5.2) with respect to $\cos\theta$ as determined from the data collected in 1994 is shown as an example in Figure 5.3. The complete set of figures for various subsets of data are collected in Appendix B.4.

In order to obtain the corrected asymmetry $A_{\mathrm{K}}^{\mathrm{corr}}$, the contribution (5.2) is added to the
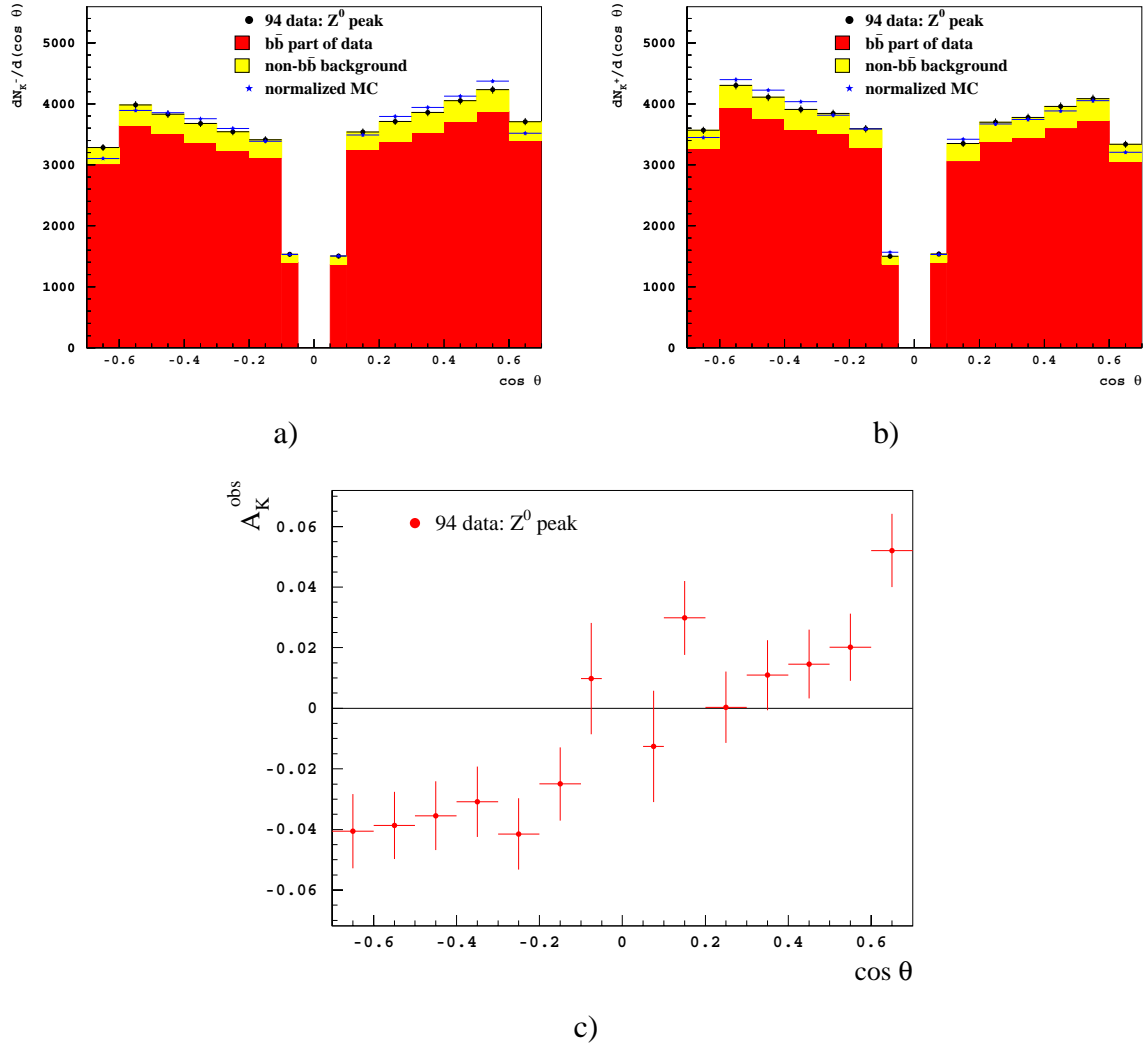
Figure 5.2 : Angular distributions of selected kaon candidates with a) negative and b) positive charge. The measured distributions correspond to 1994 data. Non-$b\bar{b}$ contribution to selected samples is estimated from the simulation. The shape of the simulated distribution (MC normalized to the number of measured events) is compared to the measured one. Note that the generated values of asymmetry in simulated samples (Table 5.5) were slightly larger than the measured values. c) The observed kaon asymmetry (5.1) obtained with distributions a) and b) after the background subtraction.

observed kaon asymmetry:

$$A_{\mathrm{K}}^{\mathrm{corr}}(\theta) = \frac{A_{\mathrm{K}}^{\mathrm{obs}}(\theta) + A_{\mathrm{K}}^{\mathrm{mat}}(\theta)}{\Lambda(\theta)} \,, \tag{5.3}$$

where distortions due to possible differences between the efficiencies in the forward and the
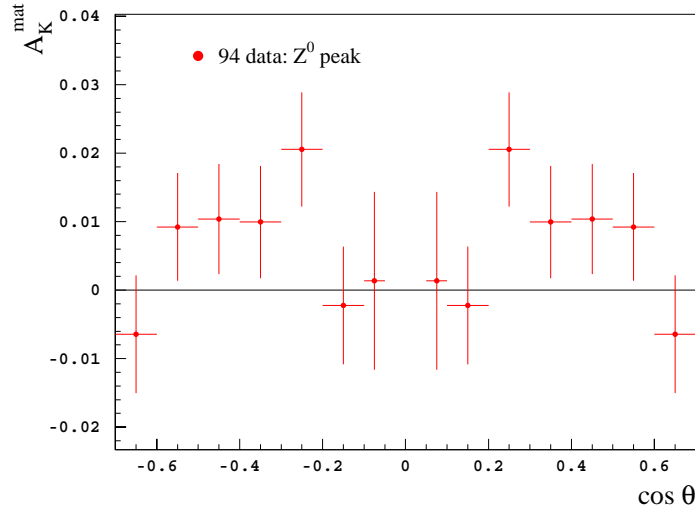
Figure 5.3 : The material kaon asymmetry as determined from the data collected in 1994.

backward direction are compensated for by introducing an additional correction factor:

$$
\Lambda(\theta) = 1 - \frac{4\left\{N_{K^+}(\theta) + N_{K^+}(\pi - \theta)\right\}\left\{N_{K^-}(\theta) + N_{K^-}(\pi - \theta)\right\}}{\left\{N_{K^+}(\theta) + N_{K^+}(\pi - \theta) + N_{K^-}(\theta) + N_{K^-}(\pi - \theta)\right\}^2} \cdot
$$
$$
\cdot \frac{\sqrt{N_{K^-}(\theta)N_{K^+}(\theta)} - \sqrt{N_{K^-}(\pi - \theta)N_{K^+}(\pi - \theta)}}{\sqrt{N_{K^-}(\theta)N_{K^+}(\theta)} + \sqrt{N_{K^-}(\pi - \theta)N_{K^+}(\pi - \theta)}} \ . \quad (5.4)
$$

Values of the compensating factor (5.4) equal unity within variations of the order of a percent. For a detailed derivation of expressions (5.1)-(5.4) see Appendix A.

Note, that in the process of the correction described above, charged kaons at angles θ and $\pi - \theta$ are simultaneously used. As a consequence, the absolute values of the A_K^{corr} at the opposite bins are the same and therefore completely correlated, as can be seen in Figure 5.4, plotted for 1994 data (see also figures for differetn data sets in Appendix B.5). This is understandable, since all the possible differences in absolute values of observed kaon asymmetry A_K^{obs} between θ and $\pi - \theta$ are attributed to the material asymmetry and the efficiency differences.

5.2   Dilution factor

The measured asymmetry (5.3) is interpreted as a paw print of the b-quark forward-backward asymmetry. However, as already mentioned in Section 2.3, a significant part of the $K^\pm$-tagging information is lost during the process of quark hadronisation, during the lifetime of B hadrons and their decay, and finally also at the level of hadron identification. For example, the charge of tracks arising in the process of quark hadronisation has no significant correlation with the charge of a b quark. The same is true for misidentified pions or protons. The charge tagging performance is spoiled also due to the process of B^0 or B_s^0 mixing, when quarks convert into their antiquarks and vice versa. Kaons from the decay chain (2.63) of mixed B mesons therefore
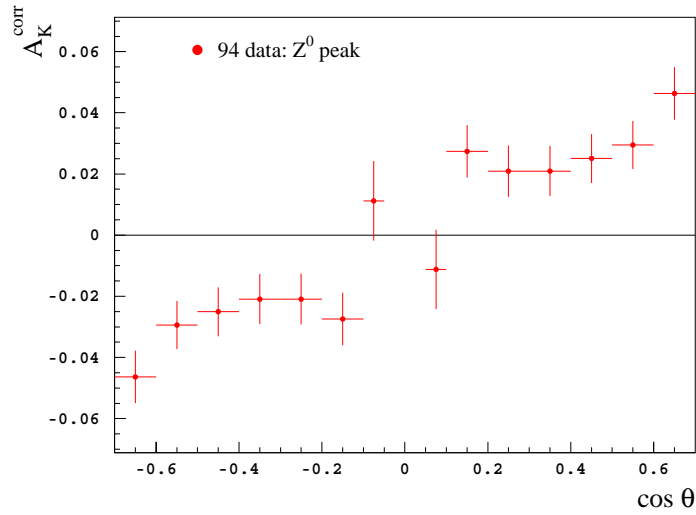
Figure 5.4 : The corrected kaon asymmetry (5.3) as a function of $\cos\theta$ for 1994 data. Note that due to the correction procedure the absolute values of asymmetry at the opposite bins in $\cos\theta$ are the same.

mistag the charge of the original b quarks from $Z^0 \rightarrow b\overline{b}$ decays. In addition, the tagging information can also be veiled in the decays of unmixed B hadrons, e.g. in the decays $b \rightarrow c\overline{c}s$ where apart from the dominant charm production (2.63) also a "wrong-sign" charm $\overline{c}$ is produced. All processes which result in loss of tagging information are accounted for by the dilution factor η_b, connecting kaon and quark asymmetries (cf. eqs. (2.64) and (A.14)).

The dilution factor η_b was determined on the measured data itself, using the double-tagged events. Charged kaon candidates were selected as in case of measured asymmetry except that here two tagging kaons per event were required, one in each of the two hemispheres. In Figure 5.5.a and 5.5.b, the numbers of selected double-tagged events from 1994 data are shown as functions of $\cos\theta$, where θ is the polar angle of the first tagging kaon. It turns out (see the derivation in Appendix A) that the square of the dilution factor equals the asymmetry of the double-tagged events:

$$\eta_b^2(\theta) = \eta_b^2(\pi - \theta) = \frac{N_K^{\mathrm{opp}}(\theta) - N_K^{\mathrm{same}}(\theta)}{N_K^{\mathrm{opp}}(\theta) + N_K^{\mathrm{same}}(\theta)} \,, \tag{5.5}$$

where $N_K^{\mathrm{opp}}(\theta)$ ($N_K^{\mathrm{same}}(\theta)$) stands for the number of events with the two tagging kaons in the opposite hemispheres having opposite (same) charge. The ratio (5.5) was made forward-backward symmetric by attributing events at θ and $\pi - \theta$ to the same thrust angle. As a consequence of this approach, each event is then counted twice and the opposite bins of a histogram shown in Figure 5.5.c are completely correlated as in case of a corrected kaon asymmetry. The non-$b\overline{b}$ contribution to the sample of the double-tagged events was again determined by using the simulated samples and subtracted from the data prior to the construction of the ratio (5.5).

The measured ratio of double-tagged events shows an angular dependence. By studying the simulated data, it was determined that the angular dependence is a consequence of the selected kaon-sample purity. The measured angular dependence of the dilution factor $\eta_b^2(\theta)$ was fitted to

a)   b)

c)
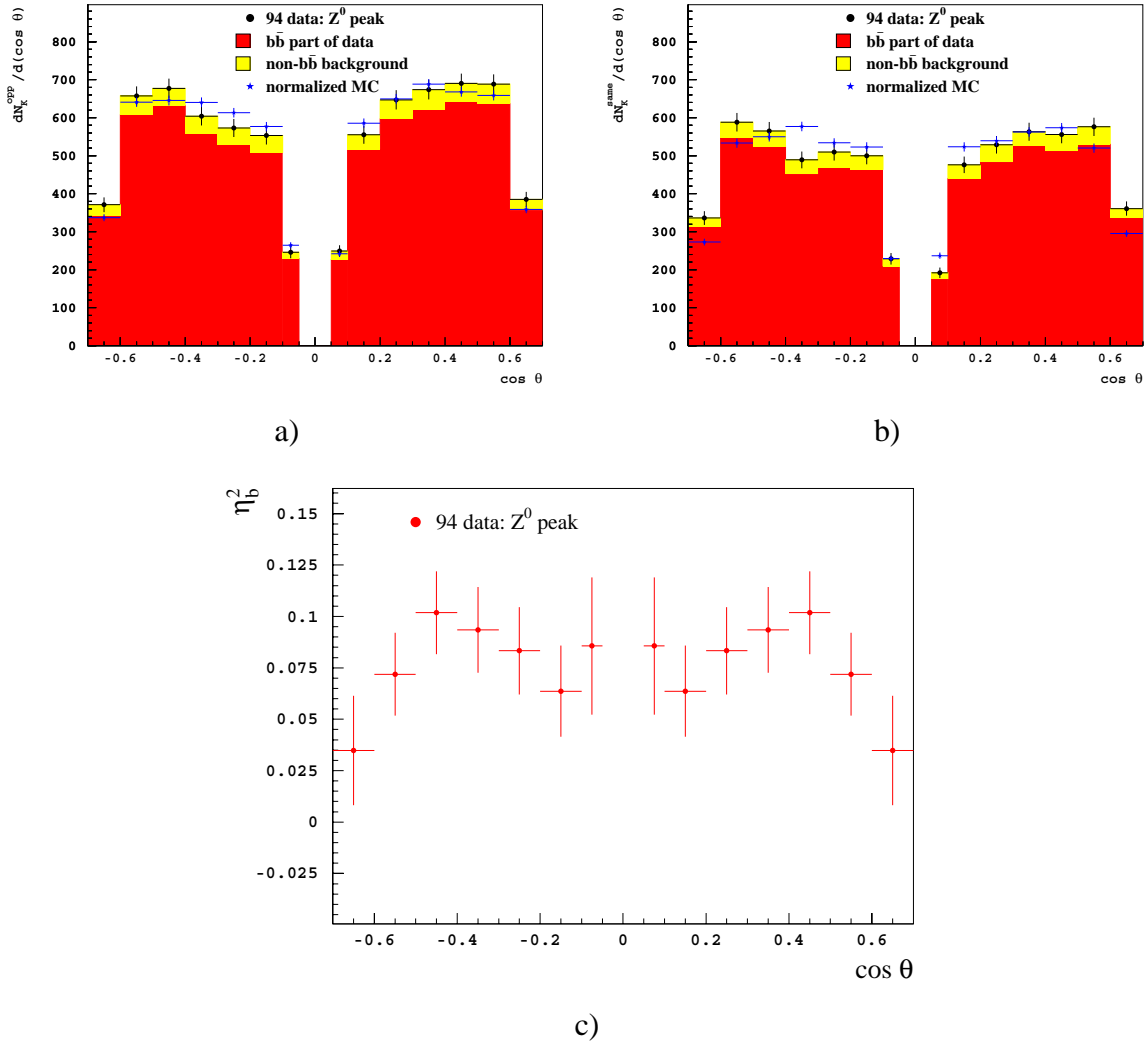
Figure 5.5 : Numbers of double-tagged events from 1994 data as a function of $\cos\theta$, where θ is the polar angle of the first tagging kaon, for the case when charges of two kaons are a) the opposite or b) the same. Non-$b\bar{b}$ contribution to selected samples is estimated from the simulation. The shape of the simulated distribution (MC normalized to the number of measured events) is shown in comparison with the measured one. c) Forward-backward symmetric ratio of double-tagged events, defined in (5.5). Note that the opposite bins are completely correlated.

a function

$$\eta_{b,0}^2 \cdot p_4(\cos\theta) = \eta_{b,0}^2 \cdot \left(a_0 + a_1 \cos^2\theta + a_2 \cos^4\theta\right). \tag{5.6}$$

The chosen shape of the function with the coefficients, $a_0 = 0.096$, $a_1 = 0.244$ and $a_2 = -0.324$, was provided by an investigation of $\eta_b^2(\theta)$ distribution as obtained with a sample of events belonging to the 1994 simulated data. The simulated distribution together with the fitting function is shown in Figure 5.6.a. The factor $\eta_{b,0}$ is a normalization factor obtained by fitting the measured data to the angular distribution $p_4(\cos\theta)$ of the 1994 simulated sample (see

Year	$\sqrt{s}$ [GeV]	$\eta_{b,0}$
1992	91.28	0.709 ± 0.093
1993	89.43	0.953 ± 0.154
	91.22	0.642 ± 0.124
	93.02	0.762 ± 0.161
1994	91.20	0.793 ± 0.044
1995	89.44	1.229 ± 0.173
	91.30	0.865 ± 0.076
	92.97	0.850 ± 0.192

Table 5.1 : The dilution factors as obtained by fitting the asymmetry of double-tagged events collected during different years of data taking to expression (5.6). Note that this factor has to be multiplied with the angular dependence $p_4(\cos\theta)$ in order to get the entire expression for $\eta_b^2(\theta)$.

Figure 5.6.b as an example). The values of $\eta_{b,0}$ obtained for different years of data taking are given in Table 5.1, while the corresponding figures are shown in Appendix B.7. In addition to this, figures of angular distributions of double-tagged events for all years of data taking are collected in Appendix B.6.
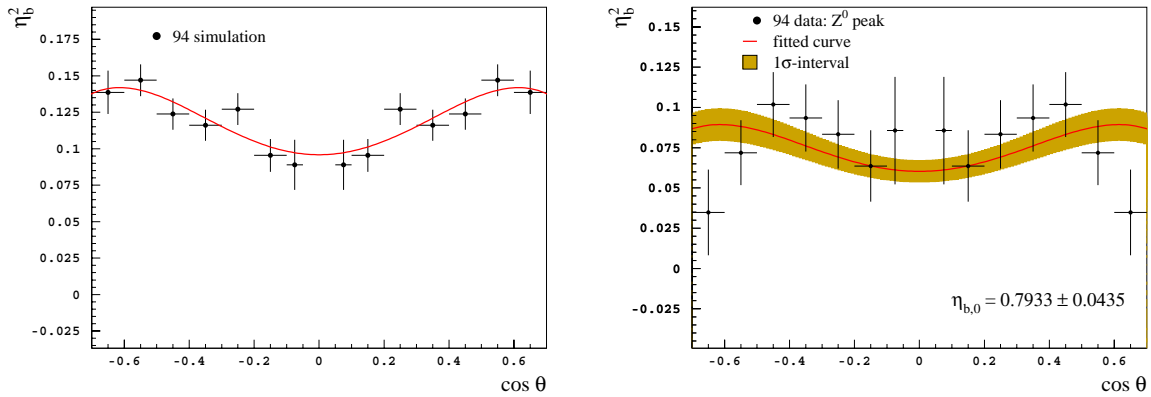
Figure 5.6 : a) The asymmetry of double-tagged events for 1994 simulated data. The distribution is shown together with the fitting function used in Expression (5.6). The shape of the function $p_4(\cos\theta)$ was determined from this very fit. b) The asymmetry of 1994 measured double-tagged kaon events shown together with the best fit function. The obtained value of $\eta_{b,0}$ with its statistical error is given in the lower right corner of the figure.

5.3 Bottom-quark forward-backward asymmetry

At a certain polar angle θ of the corrected charged-kaon asymmetry and the dilution factor, $A_{\mathrm{K}}^{\mathrm{corr}}(\theta)/\eta_{\mathrm{b}}(\theta)$ equals the corresponding b-quark asymmetry (cf. (2.64)). On the other hand, the expected value of the b-quark asymmetry can be written as:

$$A_{FB}^{\mathrm{b\overline{b}}} \cdot f(\theta) = A_{FB}^{\mathrm{b\overline{b}}} \cdot \frac{8}{3} \frac{\cos\theta}{1+\cos^2\theta} , \tag{5.7}$$

where $f(\theta)$ accounts for the angular dependence of the forward-backward asymmetry (compare eqs. (2.41) and (2.45)). The bottom-quark forward-backward asymmetry, $A_{FB}^{\mathrm{b\overline{b}}}$, used in the shape parameterisation (5.7) can then be determined by performing a minimization of a χ^2 function, defined as:

$$\chi^2 = \sum_{i=1}^{N_{\mathrm{bins}}} \left(\frac{\frac{A_{\mathrm{K}}^{\mathrm{corr}}(\theta_i)}{\eta_{\mathrm{b}}(\theta_i)} - A_{FB}^{\mathrm{b\overline{b}}}(1 - \delta_{\mathrm{QCD}}^{\mathrm{b}})f(\theta_i)}{\sigma_i} \right)^2 , \tag{5.8}$$

where σ_i are the scaled statistical errors of the corrected kaon asymmetry:

$$\sigma_i = \frac{\sigma_{A_{\mathrm{K}}^{\mathrm{corr}}(\theta_i)}}{\eta_{\mathrm{b},0} \cdot p_4(\cos\theta_i)} . \tag{5.9}$$
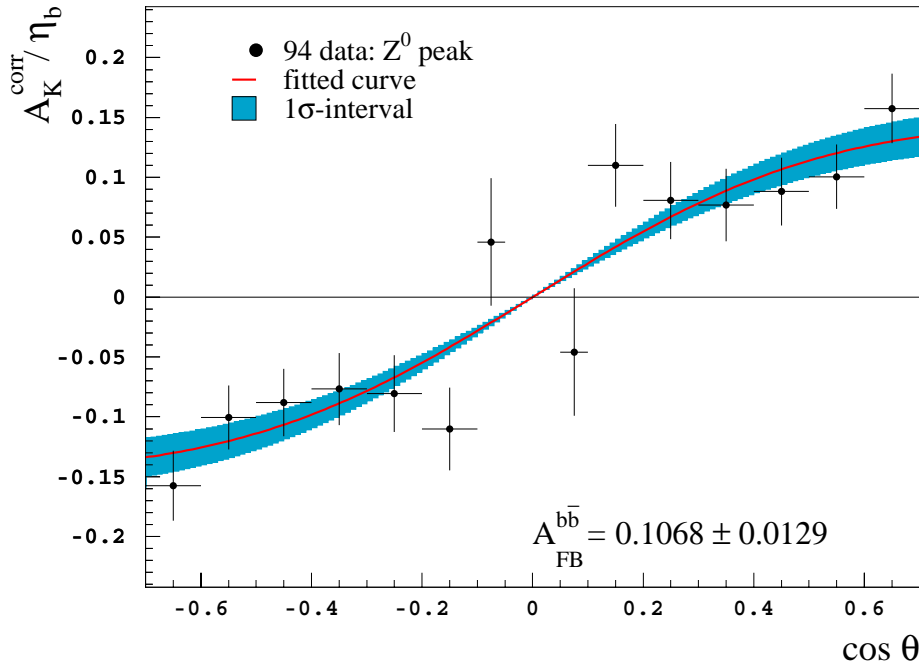
Figure 5.7 : Forward-backward asymmetry of the b quark as determined from the 1994 data together with the best fit expected shape and with those deviating one standard deviation from the optimal one (boundaries of the coloured region). Errors shown and quoted are the statistical errors of $A_{\mathrm{K}}^{\mathrm{corr}}$. Note that the opposite bins are completely correlated and that *only positive values* of $\cos\theta$ were included in the fit.

The correction factor $\delta^{\rm b}_{\rm QCD}$ was introduced here in order to compensate for the QCD effects that smear the quark asymmetry (see Section 5.4 below). Since the opposite bins of $A^{\rm corr}_{\rm K}$ and $\eta_{\rm b}$ are completely correlated, as demonstrated in Equations (5.1)-(5.4) and (5.5)), the summation index i in the expression (5.8) runs only over $N_{\rm bins}$ in the region where $0.05 \leq \cos\theta \leq 0.7$, i.e. there are altogether 7 bins included in the fits. As an illustration, Figure 5.7 shows the fitted asymmetry $A^{\rm corr}_{\rm K}(\theta)/\eta_{\rm b}(\theta)$ and the best fit function (5.7) as determined for the 1994 data (the complete set of figures for all years of data taking is displayed in Appendix B.8). The values of $A^{\rm b\overline{b}}_{FB}$ obtained for different years of data taking and centre-of-mass energies are listed in Table 5.2 together with the estimated statistical errors. The systematic uncertainties of the quoted results are extensively discussed in Section 5.5.

Year	$\sqrt{s}$ [GeV]	$A^{\rm b\overline{b}}_{FB}$
1992	91.28	$0.118 \pm 0.022_{\rm stat} \pm 0.016_{\rm syst}$
1993	89.43	$0.025 \pm 0.041_{\rm stat} \pm 0.004_{\rm syst}$
	91.22	$0.123 \pm 0.029_{\rm stat} \pm 0.024_{\rm syst}$
	93.02	$0.106 \pm 0.043_{\rm stat} \pm 0.023_{\rm syst}$
1994	91.20	$0.107 \pm 0.013_{\rm stat} \pm 0.008_{\rm syst}$
1995	89.44	$0.076 \pm 0.055_{\rm stat} \pm 0.011_{\rm syst}$
	91.30	$0.098 \pm 0.025_{\rm stat} \pm 0.010_{\rm syst}$
	92.97	$0.094 \pm 0.061_{\rm stat} \pm 0.022_{\rm syst}$

Table 5.2 : The measured forward-backward asymmetry for the bottom quark as extracted from the data taken during the years 1992-1995. The statistical errors are due to the corrected kaon asymmetry, while the systematic uncertainties are discussed in Section 5.5.

5.4 QCD corrections

The analysis of the final states of hadronic Z^0 decays gives only indirect information about the electroweak process $Z^0 \rightarrow q\overline{q}$. The evolution of primary b quarks to the final parton level and following hadronisation smear the original signature of the initial $q\overline{q}$-system. The most significant contribution to this smearing is due to the hard gluon radiation in the parton shower. This process changes significantly the direction of the primary quarks and therefore also the angular distribution of the produced partons and hadrons.

The consequence of the smearing of the quark angular distribution is the change of the quark forward-backward asymmetry. The observed b-quark asymmetry $A^{\rm b\overline{b}}_{FB}({\rm QCD})$ is then related to the original b-quark forward-backward asymmetry without gluon radiation (see (2.64)), by the

expression [44]:

$$A_{FB}^{b\overline{b}}(\text{QCD}) = (1 - \delta_{\text{QCD}}^{b})A_{FB}^{b\overline{b}}\,. \tag{5.10}$$

The QCD correction factor, δ_{QCD}^{b}, depends on the individual technique used for the measurement of the forward-backward asymmetry and its sensitivity to the mentioned gluon-radiation effects. The correction factor was therefore determined by a comparison of a forward-backward asymmetry of a simulated sample of primary b quarks and the asymmetry obtained by analysing the sample at the level of hadrons, with events that met the same selection requirements as the measured data and with the original quark direction approximated by the thrust axis. The estimated value of δ_{QCD}^{b} was:

$$\delta_{\text{QCD}}^{b} = (1.4 \pm 1.8)\,\%\,. \tag{5.11}$$

Note that relation (5.10) with the value of QCD correction factor (5.11) was already used in construction of the χ^2 function (5.8).

5.5 Cross-checks and systematic uncertainties

Table 5.3 contains a list of the considered sources of possible systematic uncertainties together with the estimated contributions to the overall uncertainty on $A_{FB}^{b\overline{b}}$.

The dilution factor η_{b} that connects the kaon forward-backward asymmetry to the asymmetry of b-quarks in Z^0 decays (see eqs. (2.64) and (5.8)), was determined by using the measured data. The systematic uncertainties on η_{b} is therefore dominated by the statistical uncertainties due to the limited number of measured events with tagging kaons in both hemispheres.

Using double-tagged events for the determination of η_{b} (see eq. (5.5)), correlations between the two hemispheres were not taken into account. For kaon-tagging, the correlation coefficient $\rho(\text{K})$ between the two hemispheres is defined by a system of two equations:

$$\begin{aligned}
N_{\text{H}}^{\text{T}}(\text{K}) &= N_{\text{H}}\ \epsilon(\text{K})\,, \\
N_{\text{E}}^{\text{T}}(\text{K}) &= N_{\text{E}}\ \epsilon(\text{K})^2\ (1 + \rho(\text{K}))\,,
\end{aligned} \tag{5.12}$$

where $N_{\text{H}}^{\text{T}}(\text{K})$ ($N_{\text{E}}^{\text{T}}(\text{K})$) is the number of kaon-tagged hemispheres (double-tagged events), N_{H} (N_{E}) is an overall number of hemispheres (events) in a selected sample, while $\epsilon(\text{K})$ is the probability to find at least one tagging kaon in a hemisphere. Figure 5.8 shows values of $\rho(\text{K})$ as determined by solving the system of equations (5.12) for the 1994 data and for the corresponding simulated sample. The correlations depend on the minimum value of the track-net output required for the tagging kaon candidates: the higher the value of the net output the lower the probability to use kaons from primary vertices that could introduce correlations due to hemisphere correlations during the process of evolution of primary quarks to the final parton level. For the minimum values of the track-net output above 0.8, the values of $\rho(\text{K})$ for the measured and for simulated data are determined to be around 5 %.

The hemisphere correlation coefficient $\rho(\text{K})$ is an average of the two coefficients: one for double-tagged events with the two kaons of the opposite charge and the other for events where

		Source of uncertainty				
Year	$\sqrt{s}$ [GeV]	$\eta_{\mathrm{b}}(\theta)$	$\delta^{\mathrm{b}}_{\mathrm{QCD}}$	Backgr. normalisation	$A^{c\bar{c}}_{FB}$	Total
1992	91.28	13.6	1.8	2.6	0.4	14.0
	89.43	16.5	1.8	2.7	0.3	16.8
1993	91.22	19.5	1.8	2.7	0.3	19.8
	93.02	21.4	1.8	2.7	0.3	21.6
1994	91.20	6.6	1.8	2.6	0.4	7.3
	89.44	14.5	1.8	1.5	0.3	14.7
1995	91.30	9.4	1.8	1.5	0.3	9.7
	92.97	22.9	1.8	1.5	0.3	23.0

Table 5.3 : Sources of systematic uncertainties on $A^{b\bar{b}}_{FB}$ with the estimated relative values (in %). To obtain the overall systematic uncertainties for individual measurement, the different sources were assumed to be uncorrelated.

the both tagged kaons are of the same charge. Since both correlation coefficients are very similar, also their impact on η_{b} would be about the same. Therefore, to check for a possible bias due to the neglected correlations, several samples of simulated events were made subject to the same procedure as were the real data. The samples that correspond to the data taken at the Z^0 peak during different years of LEP1 operation, were generated with the b-quark asymmetry set to the values that slightly differ from one year to another. Table 5.5 shows that within the expected statistical fluctuations the input asymmetries were always correctly reproduced. Since the finite simulated sample limits the precision of the reproduction, a systematic uncertainty of 3.6 % was added to the statistical uncertainties on $\eta_{\mathrm{b,0}}$ (see Table 5.1) in order to obtain the overall systematic uncertainty on $\eta_{\mathrm{b}}(\theta)$. For the cross-check, the uncertainty introduced by the choice of the fitting function $p_4(\theta)$ accounting for the shape of $\eta_{\mathrm{b}}^2(\theta)$ (see Equation (5.6)), was also estimated. According to the errors of coefficients, $a_0 = 0.096 \pm 0.009$, $a_1 = 0.244 \pm 0.119$ and $a_2 = -0.324 \pm 0.287$, and their correlation matrix (see Table 5.4), the shape of the function

	a_0	a_1	a_2
a_0	1.00	-0.806	0.667
a_1	-0.806	1.00	-0.958
a_2	0.667	-0.958	1.00

Table 5.4 : Correlation matrix for the coefficients of the function $p_4(\cos\theta)$ (5.6) used for the angular-dependence description of $\eta_{\mathrm{b}}^2(\theta)$.
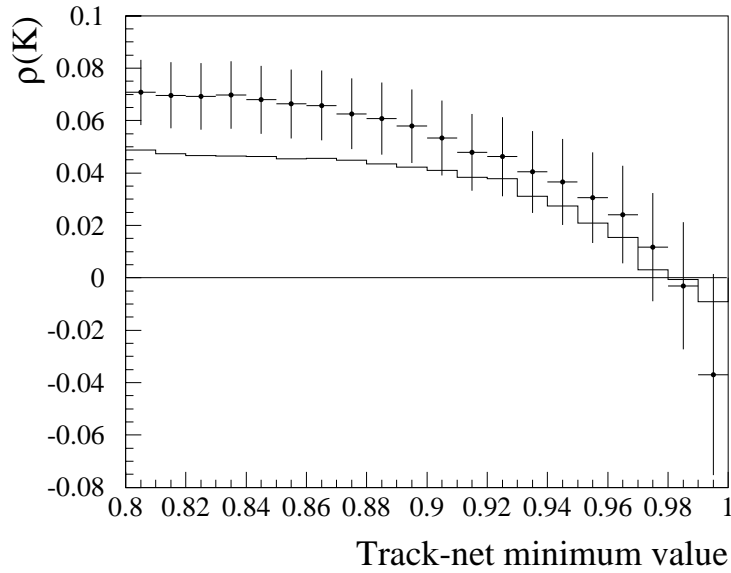
Figure 5.8 : Hemisphere correlations for kaon-tagging for the 1994 $b\overline{b}$-enriched sample (dots with error-bars) and for the corresponding simulation (histogram) with respect to the cut-value of the track-net output for the tagging kaon candidates. The statistical uncertainties shown are strongly correlated since a sample obtained with a milder cut on the track-net output contains all subsamples selected with tighter cuts.

was varied, resulting in relative variations of the measured $A_{FB}^{b\overline{b}}$ consistent with the previous estimate of 3.6 %.

The QCD correction factor, $\delta_{\text{QCD}}^{\text{b}}$, that accounts for smearing of the asymmetry during the process of evolution of primary b-quarks to the final parton level and during the following hadronisation, was determined by using simulated samples of events. The uncertainty on $\delta_{\text{QCD}}^{\text{b}}$ is a consequence of a finite Monte Carlo sample.

Inadequate normalization of simulated samples, used to subtract non-$b\overline{b}$ contributions from

Year	$A_{FB}^{b\overline{b}}(\text{input})$	$A_{FB}^{b\overline{b}}$
1992	0.108 ± 0.001	0.105 ± 0.008
1993	0.110 ± 0.001	0.110 ± 0.009
1994	0.111 ± 0.001	0.112 ± 0.006
1995	0.113 ± 0.002	0.124 ± 0.015

Table 5.5 : Generated $A_{FB}^{b\overline{b}}(\text{input})$ and extracted $A_{FB}^{b\overline{b}}$ b-quark asymmetry for the samples of Z^0 decays, simulated according to the conditions of the DELPHI detector during different years of LEP1 operation.

the measured distributions, could be an additional source of a systematic error. Its significance was estimated again by using measured samples of events. Assuming branching ratio for the decay $Z^0 \to b\bar{b}$ to be fixed at the value, given in [13], b-tag efficiencies for $b\bar{b}$ and for non-$b\bar{b}$ events, $\epsilon_b(b)$ and $\epsilon_{\not b}(b)$, can be determined by comparing the number $N_H^T(b)$ of b-tagged hemispheres to the number $N_E^T(b)$ of measured events with both hemispheres being tagged as candidates for a $Z^0 \to b\bar{b}$ decay [45]. The two efficiencies can be obtained by solving a system of equations:

$$
\begin{aligned}
N_H^T(b) &= N_H^b \, \epsilon_b(b) + N_H^{\not b} \, \epsilon_{\not b}(b) \, , \\
N_E^T(b) &= N_E^b \, \epsilon_b(b)^2 \, (1 + \rho_b(b)) + N_E^{\not b} \, \epsilon_{\not b}(b)^2 \, (1 + \rho_{\not b}(b)) \, ,
\end{aligned}
\tag{5.13}
$$

where N_E^b ($N_E^{\not b}$) is the overall number of the considered $b\bar{b}$ (non-$b\bar{b}$) decays of Z^0, while N_H^b ($N_H^{\not b}$) is the corresponding number of hemispheres. The correlation coefficients $\rho_b(b)$ and $\rho_{\not b}(b)$ for b and non-b decays are of the order of a percent and are determined by using a simulated sample. A very similar procedure can be used to extract also $K^\pm$-tagging efficiencies. Taking into account only b-tagged hemispheres, the number of hemispheres $N_H^T(b, K)$ with charged kaons that can be used for tagging charge of primary quarks was compared to the number of events $N_E^T(b, K)$ with at least one tagging $K^\pm$ in each of the two event hemispheres. Explicitly, the two numbers read:

$$
\begin{aligned}
N_H^T(b, K) &= N_H^b \, \epsilon_b(b)\epsilon_b(K) + N_H^{\not b} \, \epsilon_{\not b}(b)\epsilon_{\not b}(K) \, , \\
N_E^T(b, K) &= N_E^b \, \epsilon_b(b)^2\epsilon_b(K)^2 \, (1 + \rho_b(b))(1 + \rho_b(K)) \\
&\quad + N_E^{\not b} \, \epsilon_{\not b}(b)^2\epsilon_{\not b}(K)^2 \, (1 + \rho_{\not b}(b))(1 + \rho_{\not b}(K)) \, .
\end{aligned}
\tag{5.14}
$$

As for the b-tagging, $\epsilon_b(K)$ and $\epsilon_{\not b}(K)$ are the kaon-tagging efficiencies for b and non-b hemispheres, respectively. The values of the kaon-tagging correlation coefficients $\rho_b(K)$ and $\rho_{\not b}(K)$ were also obtained from the Monte Carlo simulation. Having $\epsilon_b(b)$ and $\epsilon_{\not b}(b)$ determined from (5.13), $\epsilon_b(K)$ and $\epsilon_{\not b}(K)$ can be extracted by solving equations (5.14).

Figure 5.9 shows fractions of non-$b\bar{b}$ measured hemispheres that met the requirements for both, b-tagging and $K^\pm$-tagging, with respect to the $\cos\theta$ of the event thrust axis. The values deduced from the data are compared to the simulated values and the ratios of the two were used as factors for a correction of the background normalisation. The value of A_{FB}^K obtained with the rescaled background contribution differed for not more than 2.7 % from the value, obtained with the uncorrected background normalisation. As expected, variations of the background normalisation by 15 - 20 % have only a small impact on the measured b-quark asymmetries since the total fraction of the background events in the selected b- and $K^\pm$- tagged data never exceeded 10 % (see Table 4.5).

The background is dominated by decays $Z^0 \to c\bar{c}$ tagged as b-decay candidates. The distribution of c-quark momenta itself is also forward-backward asymmetric and the dominant decay chain $c \to s$ implies an asymmetry of kaons in the background, too. According to the measured value of $A_{FB}^{0,c\bar{c}} = 0.0701 \pm 0.0045$ [13], the $c\bar{c}$-asymmetry in simulated samples was varied within 6.5 % causing relative variations of the measured $A_{FB}^{b\bar{b}}$ within 0.4 %.

When combined, the four sources of possible systematic uncertainties were considered as being uncorrelated. On the other hand, a correlation between the systematic uncertainty on η_b
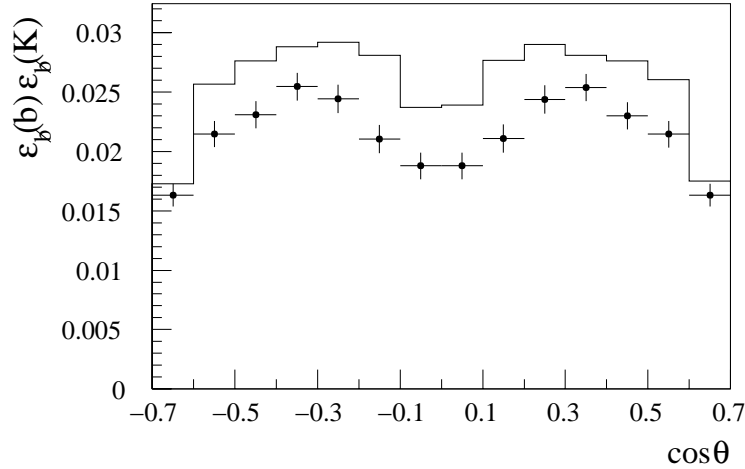
Figure 5.9 : Fraction of non-$b\overline{b}$ measured hemispheres that met the requirements for both, b-tagging and $K^{\pm}$-tagging, with respect to $\cos\theta$ of the event thrust axis. Simulated values (full histogram) are compared to the values, deduced from the measured data (points with error bars).

and the statistical uncertainty on A_K^{corr} could be expected due to a partial overlap of samples, used for the determination of the two quantities. However, the effect of the overlap was found to be of the order of less than a percent of the total error and thus negligible.

Considering the overall systematic uncertainties on $A_{FB}^{b\overline{b}}$ extracted from the data that were taken in four different years, the most important contributions originate from possible statistical fluctuations of the corresponding dilution factors and can be combined as uncorrelated. Contrary to these, a 3.6 % contribution to the uncertainty on η_b due to unknown hemisphere correlation effects (see above), uncertainties on the QCD corrections and uncertainties on the c-quark forward-backward asymmetry were treated as completely correlated for all the quoted asymmetries.

6

Results and discussion

When the results of measurements taken at similar centre-of-mass energies (see Table 5.2) are combined, the following values are obtained:

$$A_{FB}^{b\overline{b}}(89.43 \text{ GeV}) = 0.0427 \pm 0.0330_{\text{stat}} \pm 0.0048_{\text{syst}} ,$$
$$A_{FB}^{b\overline{b}}(91.24 \text{ GeV}) = 0.1084 \pm 0.0096_{\text{stat}} \pm 0.0070_{\text{syst}} , \qquad (6.1)$$
$$A_{FB}^{b\overline{b}}(92.99 \text{ GeV}) = 0.1017 \pm 0.0353_{\text{stat}} \pm 0.0169_{\text{syst}} .$$

Figure 6.1 shows the comparison of the measured values of the forward-backward asymmetry of bottom quarks to the Standard Model prediction as calculated by ZFITTER, with the parameters of the model set to their world average values [13, 17].

In order to combine the asymmetries (6.1) with other LEP measurements, the results have to be expressed in terms of the asymmetries at the following centre-of-mass energies: 89.55 GeV, 91.26 GeV and 92.94 GeV. The three values were obtained as average energies of the four LEP experiments. The shift of measured asymmetries to the quoted energies was performed by ZFITTER, yielding:

$$A_{FB}^{b\overline{b}}(89.55 \text{ GeV}) = 0.0456 \pm 0.0330_{\text{stat}} \pm 0.0048_{\text{syst}} ,$$
$$A_{FB}^{b\overline{b}}(91.26 \text{ GeV}) = 0.1088 \pm 0.0096_{\text{stat}} \pm 0.0070_{\text{syst}} , \qquad (6.2)$$
$$A_{FB}^{b\overline{b}}(92.94 \text{ GeV}) = 0.1012 \pm 0.0353_{\text{stat}} \pm 0.0169_{\text{syst}} .$$

These values are then used for the combined fit to all measured LEP results.

6.1   Forward-backward pole asymmetry

For a direct comparison of our results to other measurements, the forward-backward pole asymmetry, $A_{FB}^{0,b\overline{b}}$, has to be extracted. For this purpose, the three measured asymmetries are combined into a single value at the common centre-of-mass energy of 91.26 Gev. The two off-peak measurements are again corrected for the energy shift using the prediction from ZFITTER. The
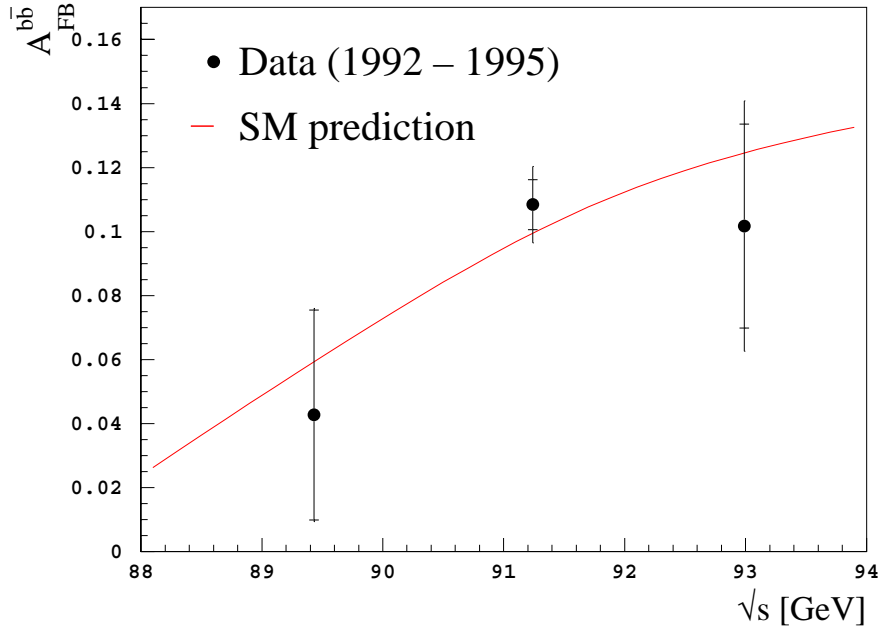
Figure 6.1 : $A_{FB}^{\mathrm{b\overline{b}}}$ as a function of the centre-of-mass energy. The results of the measurement (points with error bars) are compared to the expectations, based on the Standard Model and calculated by the ZFITTER programme package [17]. Ticks on the error bars indicate the fraction of the statistical error in the quadratic sum of both errors, statistical and systematic. The parameters of the Standard Model were set to their world average values [13], while the used value for the mass of the Higgs boson was $m_{\mathrm{H}} = 115 \ \mathrm{GeV}/c^2$.

procedure yields the following value for the average of the three measured asymmetries:

$$A_{FB}^{\mathrm{b\overline{b}}}(91.26 \ \mathrm{GeV}) = 0.1043 \pm 0.0089_{\mathrm{stat}} \pm 0.0064_{\mathrm{syst}} \ . \tag{6.3}$$

The forward-backward pole asymmetry is defined for the pure Z^0-exchange process, with the effective couplings due to the radiative weak corrections (cf. Equation (2.59)). In order to extract the pole value, corrections to the combined measured asymmetry (6.3) have to be

Source of corrections	$\delta A_{FB}^{\mathrm{b\overline{b}}}$
$\sqrt{s} \neq m_{\mathrm{Z}}$	-0.0013
ISR, γ, $\gamma\mathrm{Z}^0$, $\mathrm{m_b}$	$+0.0038$

Table 6.1 : The correction to the $A_{FB}^{\mathrm{b\overline{b}}}$ due to the initial state radiation, the finite mass of the b quark, the γ-exchange and the $\gamma\mathrm{Z}^0$-interference, δ_{QED}, and the correction $\delta_{\sqrt{s}}$ due to shift in the centre-of-mass energy from 91.26 GeV to the Z^0 peak at 91.188 GeV. Values for corrections are taken from [5].
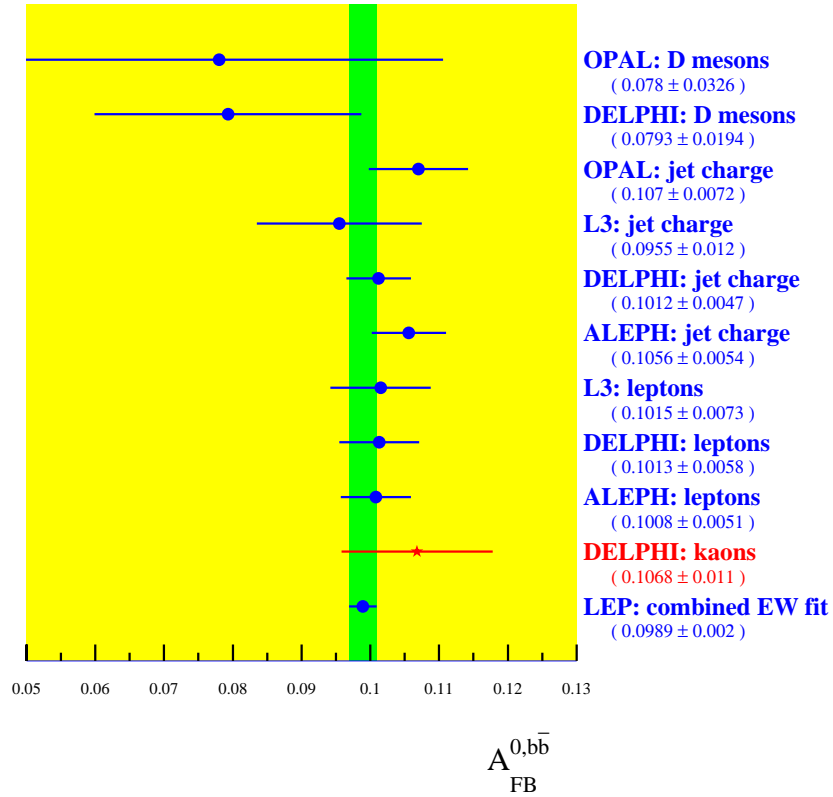
Figure 6.2 : Comparison of values for $A_{FB}^{0,b\overline{b}}$ as determined by different techniques and by all four LEP experiments. The result of the combined fit to different electroweak parameters, determined with the entire LEP data [5] is also shown.

applied:

$$A_{FB}^{0,b\overline{b}} = A_{FB}^{b\overline{b}} + \delta_{\text{QED}} + \delta_{\sqrt{s}} \,. \tag{6.4}$$

The first correction, δ_{QED}, accounts for the fact that the effects of the initial state radiation as well as those of the γ-exchange and of the γZ^0-interference are *not* included in the definition of the effective couplings and angles, and must therefore be subtracted from the measured asymmetry. A very small correction due to the non-zero mass of the b quarks is also included in this term. In addition, the asymmetries are expected to be slightly shifted, because the measurements were performed at centre-of-mass energies different from the Z^0 nominal mass at 91.188 GeV. This shift of the asymmetries is taken into account by the second correction factor, $\delta_{\sqrt{s}}$. Both corrections for the $A_{FB}^{b\overline{b}}$ were again calculated by the ZFITTER programme package and are listed in Table 6.1. Applying the correction values quoted in Table 6.1, yields:

$$A_{FB}^{0,b\overline{b}} = 0.1068 \pm 0.0089_{\text{stat}} \pm 0.0064_{\text{syst}} \,. \tag{6.5}$$

After combining the statistical and the systematic error into a single value, the pole asymmetry
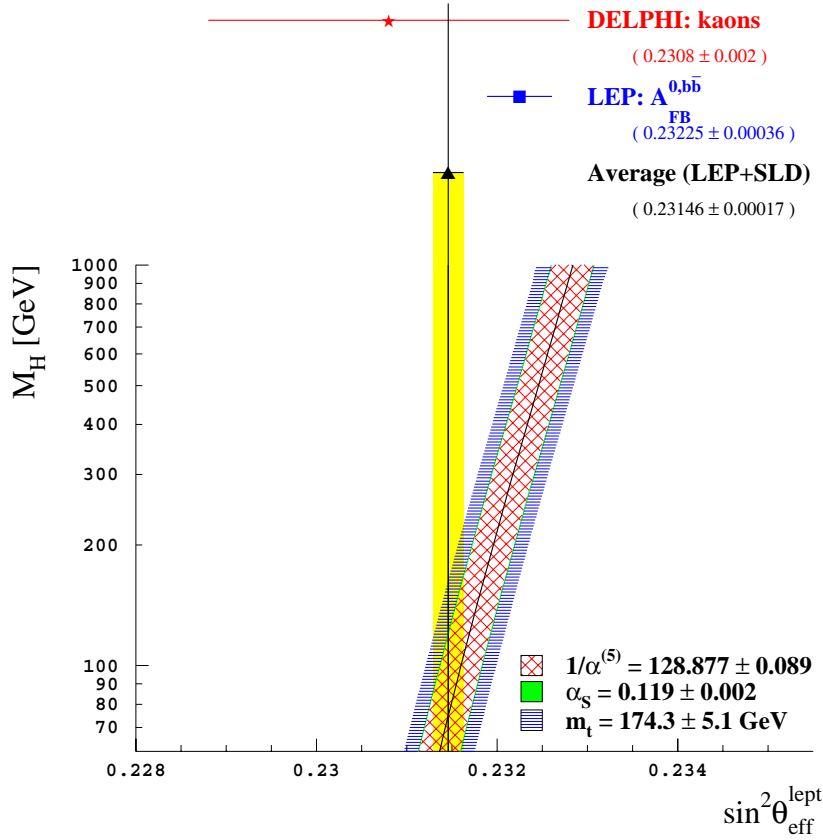
Figure 6.3 : Comparison of the value for $\sin^2\theta_{\mathrm{eff}}^{\mathrm{lept}}$ as quoted in eq. (6.7) to the average value obtained by combining all LEP and SLD data. The value of the mixing angle as determined only from measurements of bottom-quark forward-backward asymmetry at LEP is also shown. Both averages are taken from ref. [5].

reads:

$$A_{FB}^{0,\mathrm{b\overline{b}}} = 0.1068 \pm 0.0110 \,. \tag{6.6}$$

The two errors were treated as uncorrelated since corrections due to correlation between statistical errors of measured asymmetry and dilution factor were found to be of the order of 10^{-4} and thus negligible (see Section 5.5). The obtained value (6.6) coincides within the quoted uncertainties with the results of previous measurements of the LEP experiments, using charged leptons [46–48], jet charge [49–52] or reconstructed D mesons [53, 54] for the quark-tagging purposes. The comparison is shown in Figure 6.2.

6.2 Effective electroweak mixing angle

Using the procedure, described in Section 2.2.4, the pole asymmetry (6.6) can be converted to the effective electroweak mixing angle for leptons:

$$\sin^2\theta_{\mathrm{eff}}^{\mathrm{lept}} = 0.2308 \pm 0.0020 \,. \tag{6.7}$$

The determined value of the effective mixing angle (6.7) is also in good agreement with results from other measurements (cf. Figures 1.1 and 6.3).

Unfortunately, the uncertainty on the measured asymmetry, and consequently the uncertainty on the extracted value of $\sin^2 \theta_{\text{eff}}^{\text{lept}}$ do not allow for setting a stringent upper limit on the Higgs boson mass. It turns out this is an impossible task also for any other individual measurement of $A_{FB}^{b\overline{b}}$, including the ones with the highest precision. Results from all asymmetry measurements have to be combined for this purpose. In this way, the value of $M_{\text{H}} \lesssim 300$ GeV is obtained at 95 % confidence level from the combined results for the LEP and SLD experiments (see Figure 6.3).

6.3   Conclusions

The bottom-quark forward-backward asymmetry was measured, exploiting for the first time the technique of tagging the charge of a b quark with charged kaons. The use of the technique was possible due to hadron identification capability of the DELPHI detector based on the use of the Barrel RICH detectors. The DELPHI Collaboration thus measured $A_{FB}^{b\overline{b}}$ with altogether four quark-charge tagging techniques: using charged leptons, jet charge, reconstructed D mesons and charged kaons.

Although the uncertainty of the measurement is worse as for measurements of $A_{FB}^{b\overline{b}}$ with charged leptons, it is still comparable to some jet charge measurements and better than the measurements with reconstructed D mesons (see Figure 6.2). In addition to this, because of different quark-charge tagging technique we do not expect significant correlations due to overlaps of the selected sample with samples used in other DELPHI measurements. For this reason, the measurement provides a complementary information to the one obtained from other measurements and the measured results can be easily combined with previously determined values.

7

Povzetek doktorske disertacije

7.1 Motivacija in teoretsko ozadje

Tri generacije kvarkov in tri generacije leptonov predstavljajo osnovne gradnike snovi, katerih skupna značilnost je spin $\frac{1}{2}$. Interakcijo med osnovnimi gradniki posredujejo kvanti polj: šibki bozoni W^+, W^- in Z^0 so nosilci šibke sile, brezmasni fotoni elektromagnetne, prav tako brezmasne gluone pa pripišemo močni sili. Tudi omenjeni delci polja imajo nekaj skupnega: spin 1. Opisani delci nastopajo v teoriji, imenovani *standardni model* (SM) [1–3]. Njegova značilnost je invariantnost na lokalne umeritvene transformacije, preko katerih so v teorijo vgrajene interakcije med gradniki snovi in nosilci polj. Izkaže se, da je za generacijo mas šibkih bozonov potreben zlom umeritvene simetrije in vpeljava Higgsovega polja [7]. Isto polje se sklaplja tudi s fermioni, leptoni in kvarki, in tako po drugi strani poskrbi še za njihovo maso. Kršitev parnosti, ki je ena od osnovnih lastnosti šibke interakcije, je v model vgrajena z vpeljavo različnih sklopitev šibkih bozonov z levoročnimi in desnoročnimi fermioni. Kljub temu da standardni model zaradi svojih 18 prostih parametrov ni idealen, vendarle presenetljivo dobro ustreza dosedanjim merskim rezultatom. Skoraj vsi delci, ki nastopajo v tej teoriji, so znani. Edina izjema je Higgsov bozon, vzbujeno stanje Higgsovega polja, o katerem je zaenkrat le nekaj posrednih merskih podatkov. Največ namigov o masi tega delca dobimo trenutno iz meritve asimetrije naprej-nazaj pri reakciji $e^+e^- \to (Z^0, \gamma) \to f\bar{f}$ (tu sta f in $\bar{f}$ fermion in antifermion). V nadaljevanju je na kratko razložena odvisnost asimetrije od parametrov standardnega modela.

Asimetrijo naprej-nazaj v procesu $e^+e^- \to f\bar{f}$ definiramo kot:

$$A_{FB}^{f\bar{f}} = \frac{\sigma_F^f - \sigma_B^f}{\sigma_F^f + \sigma_B^f} \,, \tag{7.1}$$

pri čemer sta preseka v smeri naprej in v smeri nazaj podana z integraloma:

$$\sigma_F^f = \int\limits_0^1 \frac{d\sigma_f}{d(\cos\theta)}\, d(\cos\theta) \quad \text{in} \quad \sigma_B^f = \int\limits_{-1}^0 \frac{d\sigma_f}{d(\cos\theta)}\, d(\cos\theta)\,. \tag{7.2}$$

Polarni kot θ označuje kot med smerjo fermiona in smerjo osi žarka elektronov (glej sliko 2.3).

Če zanemarimo maso nastalih fermionov, lahko potem diferencialni presek zapišemo kot:

$$\frac{d\sigma_{\mathrm{f}}}{d\cos\theta} \propto 1 + \cos^2\theta + \frac{8}{3}A_{FB}^{\mathrm{f\bar{f}}}\cos\theta \ . \tag{7.3}$$

V splošnem je asimetrija posledica izmenjave bozona Z^0, ki jo izmenjava fotona in interferenca med fotonom in Z^0 dodatno zapleteta. Na srečo pri težiščni energiji, ki ustreza masi Z^0, interferenčni prispevek skoraj popolnoma izgine, tako da lahko asimetrijo v Bornovem približku zapišemo v naslednji obliki:

$$A_{FB}^{\mathrm{f\bar{f}}}(M_{\mathrm{Z}}^2;\mathrm{Born}) = \frac{3}{4}\frac{2v_{\mathrm{e}}a_{\mathrm{e}}\cdot 2v_{\mathrm{f}}a_{\mathrm{f}}\sqrt{1-4\mu_{\mathrm{f}}}}{(v_{\mathrm{e}}^2+a_{\mathrm{e}}^2)(v_{\mathrm{f}}^2+a_{\mathrm{f}}^2) + \mu_{\mathrm{f}}(v_{\mathrm{e}}^2+a_{\mathrm{e}}^2)(2v_{\mathrm{f}}^2-4a_{\mathrm{f}}^2) + \left(\frac{\Gamma_{\mathrm{Z}}^0}{M_{\mathrm{Z}}}\right)^2 q_{\mathrm{e}}^2 q_{\mathrm{f}}^2(1+2\mu_{\mathrm{f}})} \ . \tag{7.4}$$

Tu je μ_{f} razmerje kvadratov mas fermiona m_{f} in nevtralnega šibkega bozona M_{Z}, medtem ko je Γ_{Z}^0 širina resonance Z^0. *Vektorsko* in *aksialno* sklopitveno konstanto, v_{f} in a_{f}, definiramo kot:

$$v_{\mathrm{f}} = \frac{I_{W,\mathrm{f}}^3 - 2q_{\mathrm{f}}\sin^2\theta_W}{2\sin\theta_W\cos\theta_W} \ , \quad a_{\mathrm{f}} = \frac{I_{W,\mathrm{f}}^3}{2\sin\theta_W\cos\theta_W} \ , \tag{7.5}$$

pri čemer $I_{W,\mathrm{f}}^3$ označuje tretjo komponento šibkega izospina, q_{f} pa naboj fermiona. Ker sta člena μ_{f} in $(\Gamma_{\mathrm{Z}}^0/M_{\mathrm{Z}})^2$ kvečjemu reda velikosti 10^{-3}, lahko v izrazu za asimetrijo zanemarimo člene, ki so posledica mas fermionov in izmenjave fotona. Tedaj je mogoče izraz za Bornov približek (7.4) faktorizirati tako, da v enem faktorju nastopa le par začetnih fermionov, v drugem pa par končnih:

$$A_{FB}^{\mathrm{f\bar{f}}}(M_{\mathrm{Z}}^2;\mathrm{Born}) = \frac{3}{4}\mathcal{A}_{\mathrm{e}}\mathcal{A}_{\mathrm{f}} \ . \tag{7.6}$$

Delni asimetriji v gornjem izrazu sta potem definirani kot:

$$\mathcal{A}_{\mathrm{f}} = \frac{2a_{\mathrm{f}}v_{\mathrm{f}}}{a_{\mathrm{f}}^2+v_{\mathrm{f}}^2} = \frac{2(1-4|q_{\mathrm{f}}|\sin^2\theta_W)}{1+\left(1-4|q_{\mathrm{f}}|\sin^2\theta_W\right)^2} \ , \tag{7.7}$$

kjer se f nanaša tako na fermione v začetnem stanju – elektrone – kot na fermione v končnem stanju. Vidimo, da je asimetrija odvisna od naboja fermionov in sinusa Weinbergovega kota. Hitro je moč ugotoviti, da je delna asimetrija $\mathcal{A}_{\mathrm{f}}$ največja pri spodnjih kvarkih (d, s, b), katerih naboj je enak tretjini naboja elektrona, in da je odvisnost $\mathcal{A}_{\mathrm{f}}$ od $\sin^2\theta_W$ največja pri nabitih leptonih (glej tudi sliko 7.1). Zato je pri meritvi asimetrije naprej-nazaj izbira, pri kateri imamo v začetnem stanju par e^+e^- in v končnem $b\bar{b}$, primerna za natančno določitev $\sin^2\theta_W$. Lahko bi rekli, da je meritev $A_{FB}^{b\bar{b}}$ občutljiva na vrednost Weinbergovega kota, saj nam končno stanje $b\bar{b}$ služi kot ojačevalec močne odvisnosti $\mathcal{A}_{\mathrm{e}}$ od $\sin^2\theta_W$.

Enačba (7.4) je le približek v najnižjem redu k asimetriji naprej-nazaj. Upoštevati je treba vrsto popravkov višjega reda. Smiselno jih je razvrstiti v tri skupine:
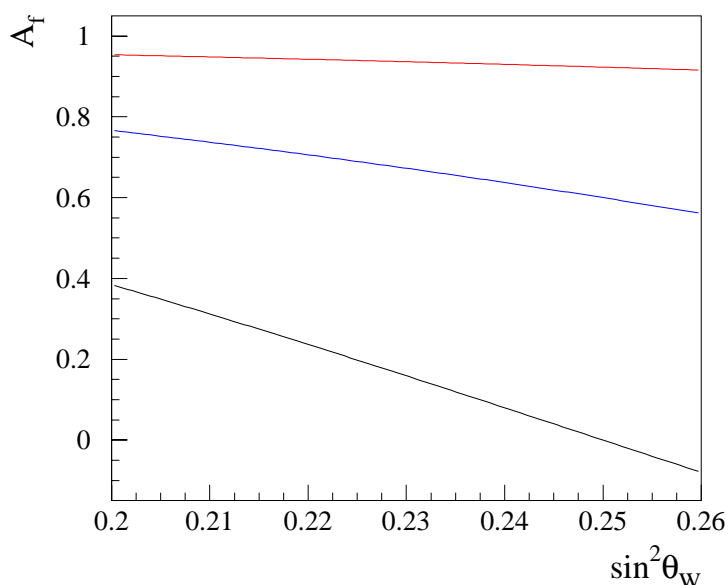
Slika 7.1 : Odvisnost delne asimetrije $\mathcal{A}_\mathrm{f}$ od $\sin^2 \theta_W$. Rdeča krivulja velja za spodnje kvarke, modra za zgornje in črna za nabite leptone.

1. **Popravki zaradi močne interakcije (QCD popravki)**: V končnem stanju nastane par $b\bar{b}$. Ker kvarki močno interagirajo, lahko pri fragmentaciji izsevajo gluone s precejšnjo energijo. Zaradi tega lahko smer kvarkov odstopa od njihove prvotne smeri. K sreči je sklopitvena konstanta močne interakcije α_s v energijskem območju okoli vrha resonance Z^0 le okoli 0,12, tako da so QCD popravki asimetrije tipično veliki le nekaj odstotkov. Seveda je velikost popravkov močno odvisna od tega, v kolikšni meri pri obdelavi podatkov zavržemo pare $b\bar{b}$, pri katerih je prišlo do izsevanja gluonov. QCD popravke moramo zato oceniti za vsako merilno metodo posebej.

2. **Kvantno elektrodinamski popravki (QED popravki)**: Tipi popravkov so prikazani na sliki 2.8, njihov vpliv na asimetrijo pa na sliki 2.9. Glavni prispevek predstavlja sevanje v začetnem stanju, zaradi katerega pride do zmanjšanja asimetrije. Prispevki sevanja v končnem stanju in deleži različnih škatlastih diagramov s propagatorji γZ^0 in $\gamma\gamma$ pa so majhni. Tudi velikost QED popravkov je močno odvisna od zahtev, postavljenih pri izbiri vzorcev, na katerih merimo asimetrijo.

3. **Šibki popravki**: To so popravki, ki še ostanejo po vključitvi QCD in QED popravkov in so posebej zanimivi zato, ker so med drugim odvisni tudi od Higgsovega bozona in nudijo možnost za posredno oceno njegove mase.

   Šibke popravke lahko v grobem razdelimo na popravke k propagatorjem za Z^0 in γ (glej sliko 2.5.a), popravke k vozliščem (slika 2.5.b) ter prispevke škatlastih diagramov (prikazani so na sliki 2.5.c). Nekaj popravkov odpade, če se omejimo na težiščno energijo

pola Z^0. Podatke, izmerjene v bližini pola Z^0, lahko s programskim paketom ZFITTER popravimo tako, da ustrezajo polu Z^0. Nekaj popravkov odpade tudi zato, ker je asimetrija definirana kot razmerje presekov. Večina popravkov, ki kljub temu preostanejo, je mogoče vključiti tako, da v izrazu za $\mathcal{A}_f$ (7.7) spremenimo Weinbergov kot $\sin^2 \theta_W$ v efektivnega, $\sin^2 \theta_{\mathrm{eff}}^{\mathrm{f}}$. V to spremembo so med drugim vključeni členi, odvisni od mase kvarka t in mase Higgsovega bozona. Odkar poznamo maso kvarka t, lahko tako iz meritve asimetrije naprej-nazaj ocenimo velikost šibkih popravkov, odtod pa dobimo oceno za maso Higgsovega bozona. Žal je odvisnost asimetrije in efektivnega kota od m_H logaritmična (slika 2.11), nekateri parametri standardnega modela pa precej nenatančno izmerjeni, kar otežuje natančnejšo določitev mase Higgsovega bozona.

7.2 Merilna metoda

Ker v Naravi ni prostih kvarkov, moramo pri meritvi asimetrije za proces $e^+ e^- \rightarrow b\overline{b}$ določiti identiteto nastalih kvarkov z meritvijo delcev, ki jih detektor zazna. Metoda, opisana v tem delu, temelji na označevanju naboja kvarkov b z nabitimi kaoni, ki so nastali v razpadni verigi[†] $b \rightarrow c \rightarrow s$. Zaradi take razpadne verige nastane več negativnih kaonov v pljuskih b in več pozitivnih kaonov v pljuskih $\overline{b}$. Tako pričakujemo, da bomo zaradi kvarkovske asimetrije izmerili tudi kaonsko:

$$A_{FB}^{\mathrm{K}} = \eta_{\mathrm{b}} A_{FB}^{b\overline{b}} \,. \tag{7.8}$$

Sorazmernostni koeficient med obema asimetrijama je slabilni faktor:

$$\eta_{\mathrm{b}} = 2c_{\mathrm{b}} - 1 \,, \tag{7.9}$$

ki je preprosta funkcija verjetnosti c_{b} za pravilno določitev naboja kvarkov b. Verjetnost je seveda manjša od 1, ker poleg negativnih kaonov v verigi razpadov kvarkov b (slika 2.12.a) dobimo tudi pozitivne kaone, ki lahko napačno označijo naboj kvarka (primerjaj sliko 2.12.b).

7.3 Eksperimentalna postavitev

Meritve so potekale na trkalniku LEP v Evropskem centru za fiziko delcev CERN v Ženevi. Trkalnik LEP (slika 3.1) z obsegom 26,7 km je bil nameščen okrog 100 m pod zemljo. Med letoma 1989 in 1995 (obdobje LEP1) je obratoval pri težiščni energiji okoli 91 GeV, ki je zanimiva za opisano meritev. Postopek, uporabljen za nastanek in pospeševanje elektronov in pozitronov do končne energije, je razviden s slike 3.2. V obroč trkalnika je bilo nameščenih osem pospeševalnih elementov, ki so skrbeli za nadomeščanje izgub, nastalih zaradi sinhrotronskega sevanja. Frekvenca kroženja gruč delcev je znašala 11,25 kHz. Število gruč v žarku je bilo v letih delovanja različno, med 4, 8 in 12. V vsaki gruči je bilo 10^{11} do $1,5 \cdot 10^{11}$ elektronov ali pozitronov.

[†]Vsakič ko zapišemo izraz za delce, imamo v mislih tudi njihove antidelce, razen če drugačna uporaba ni posebej poudarjena.

Ob trkalnem obroču so bili postavljeni štirje detektorji: ALEPH, DELPHI, L3 in OPAL, ki so se med sabo nekoliko razlikovali. Sistem žarkovne optike je poskrbel za to, da v je središču vsakega od detektorjev prihajalo do trkov med elektroni in pozitroni. Luminoznost so merili s sipanjem Bhabha, katerega presek je dobro poznan. Tipična dosežena luminoznost v obdobju LEP1 je bila $1,5 \cdot 10^{31}$ cm^{-2}s^{-1}, kar je na posameznem reakcijskem mestu ustrezalo nastanku enega Z^0 vsaki dve sekundi. Celotna integrirana luminoznost na detektor je znašala 200 pb^{-1}, tako da so vsi detektorji skupaj lahko zabeležili približno 20 milijonov razpadov bozona Z^0.

Podatki, obravnavani v tem delu, so bili izmerjeni z detektorjem DELPHI, ki je shematsko predstavljen na sliki 3.3. Detektor je tehtal okrog 3500 ton, v dolžino in širino pa je meril približno 10 m. Sestavljali so ga centralni cilindrični del in po en končni pokrov na vsakem koncu. Pokrova sta bila nameščena na tračnicah, tako da ju je bilo moč odmakniti in priti do notranjih delov. Centralni del detektorja je bil sestavljen iz več cilindričnih podenot, katerih simetrijska os je sovpadala z elektronsko-pozitronskim snopom. Znotraj detektorja je bilo solenoidalno magnetno polje z jakostjo 1,2 T, ki je služilo za ukrivljanje sledi nabitih delcev. Os z koordinatnega sistema detektorja je bila določena s smerjo snopa elektronov, radij R in azimutalni kot ϕ pa sta opisovala ravnino, pravokotno na os z. V grobem je bil prostorski kot, ki ga je pokrival centralni cilindrični del detektorja, podan z območjem polarnega kota $|\cos\theta| \leq 0,7$. V nadaljevanju je podan kratek opis tistih delov detektorja, ki so pomembni za meritev $A_{FB}^{b\bar{b}}$. Natančnejši opis detektorja in njegovih lastnosti pa je moč najti drugje [22,23]. Zaradi pomanjkanja ustreznih slovenskih izrazov bomo v opisu dele detektorja večinoma poimenovali kar z originalnimi, angleškimi imeni.

Žarkovno cev je obkrožal *Vertex Detector* (VD) [24], sestavljen iz treh slojev koncentričnih silicijevih mikropasovnih detektorjev. Detektor je namenjen določanju primarne interakcijske točke in točk šibkih razpadov hadronov. V začetku leta 1994 je bil obnovljen, tako da je omogočal tudi meritev koordinate z. Pokrival je območje polarnega kota θ med $25°$ in $155°$.

Naslednji v smeri od znotraj navzven je bil *Inner Detector* (ID), ki je pokrival območje polmerov med 12 cm in 28 cm. Sestavljen je bil iz dveh delov. Notranja plast je bila potovalna komora, ki je zasedala prostor do radija 23 cm. Zunanja, prožilna plast je omogočala meritev vseh treh koordinat, R, ϕ in z. Pred letom 1995 so jo sestavljale večžične proporcionalne komore, v začetku leta 1995 pa so jih zamenjali cevnimi detektorji (*straw tubes*). ID je pokrival območje polarnih kotov $29° \leq \theta \leq 151°$, v letu 1995 pa celo kote $15° \leq \theta \leq 165°$.

Time Projection Chamber (TPC) je ležala zunaj ID in pokrivala polmere med 30 cm in 122 cm in območje polarnih kotov $39° \leq \theta \leq 141°$. Predstavljala je najpomembnejši del sistema za detekcijo nabitih sledi. Naboj, ki so ga ustvarili delci na poti skozi plin, s katerim je bila TPC napolnjena, je potoval proti končnim ploskvam, kjer so ga zaznale proporcionalne komore. Z merjenjem specifične ionizacije v plinu je TPC služila tudi za identifikacijo delcev.

Območje polmerov med 198 cm in 206 cm ter polarnih kotov θ med $42°$ in $138°$ je pokrival *Outer detector* (OD), sestavljen iz petih plasti potovalnih komor.

Opisani detektorji so sestavljali sledilni sistem v centralnem cilindričnem delu detektorja DELPHI. Z določanjem ukrivljenosti delcev v magnetnem polju je sledilni sistem omogočal merjenje gibalnih količin z ločljivostmi med $\sigma_p/p \simeq p \cdot 0,001$ GeV^{-1}[‡] in $\sigma_p/p \simeq p \cdot 0,005$ GeV^{-1}.

[‡]V povzetku uporabljene enote so v skladu z dogovorom $\hbar = c = 1$.

Prostor med TPC in OD je pokrival centralni detektor obročev Čerenkova (Barrel RICH) [26], ki je predstavljal najpomembnejši del sistema za identifikacijo delcev. Sestavljala sta ga tekoči in plinski del, pokrival pa je območje polarnih kotov med $42°$ in $138°$. Nabiti delci so pri preletu tega detektorja povzročili sevanje Čerenkova v detektorju. Detektor je sevanje zaznal kot kroge, katerih radij je bil odvisen od vrste delca, ki je sevanje povzročil. Prag za detekcijo nabitih kaonov je bil v tekočem sevalcu Čerenkovih fotonov pri gibalni količini 0,6 GeV, v plinskem pa pri 8 GeV.

High density Projection Chamber (HPC) je bil elektromagnetni kalorimeter v centralnem delu detektorja, sestavljen iz svinčenih plasti, med katerimi so bile vrzeli, napolnjene s plinom. Vsaka vrzel je opravlja podobno funkcijo kot TPC. HPC je bil namenjen sledenju elektronov in fotonov in je pokrival območje polarnih kotov $42° \leq \theta \leq 138°$.

Hadronski kalorimeter (HCAL) je služil predvsem za detekcijo sledi nevtralnih hadronov. Pokrival je polarne kote med $11°$ in $169°$, nameščen pa je bil kar v jarmu superprevodnega magneta.

Za označevanje kvarkov b pridejo v poštev predvsem nabiti kaoni z gibalnimi količinami med 2 GeV in 15 GeV. Pri identifikaciji takih kaonov so najpomembnejši podatki iz detektorja Barrel RICH. V kombinaciji s podatki o specifični ionizaciji v TPC služijo za določitev posebnega parametra, s katerim lahko izbiramo med čistostjo in izkoristkom vzorca dogodkov. Tipično je bil identifikacijski parameter izbran tako, da je bila čistost izbranega vzorca kaonov okrog 60 %, izkoristek identifikacije pa okoli 70 %.

7.4　Izbira dogodkov

V analizo so bili vključeni podatki, ki izhajajo iz meritev, opravljenih v letih od 1992 do 1995. Postopek selekcije je bil naravnan na razpade tipa $Z^0 \to q\overline{q}$, pri čemer so morali dogodki in sledi delcev zadoščati zahtevam v razpredelnici 7.1.

S tem postopkom je bilo izbranih okrog 3 milijone hadronskih razpadov Z^0 z območja težiščnih energij, ki približno ustrezajo $M_Z \pm 2$ GeV. Simulacija pokaže 86-odstotni izkoristek pri izbiri hadronskih razpadov Z^0 in zanemarljiv delež ozadja v izbranem vzorcu: pod 0,5 %. V simulacijo je bilo vključenih 12,4 milijona hadronskih dogodkov, pri čemer so bili parametri simulacije nastavljeni tako, da so se generirani vzorci kar najbolje ujemali z izmerjenimi [34, 35].

Nadaljnja omejitev pri izbiri vzorca se je nanašala na os dogodka (*thrust* os), ki je definirana s težiščem gibalnih količin v pljusku in se precej dobro ujema s smerjo začetnega kvarka. Zahteva za polarni kot θ_T osi dogodka, $|\cos\theta_T| < 0.7$, je bila pri izbiri vzorca potrebna zaradi omejene kotne sprejemnosti detektorja VD, ki je igral odločilno vlogo pri izbiri razpadov $Z^0 \to b\overline{b}$.

Razpade $Z^0 \to b\overline{b}$ je moč ločiti od ostalih hadronskih razpadov Z^0 na osnovi nekaterih posebnih lastnosti hadronov B, kot sta njihova sorazmerno velika masa in življenjski čas okoli 1,6 ps. Posledica teh lastnosti so sorazmerno velike gibalne količine delcev, ki nastanejo pri razpadih hadronov B ter znaten kot med smerjo gibalne količine in smerjo pljuska kvarka b. Najbolj značilni za delce, ki nastanejo pri razpadih hadronov B, pa so veliki vpadni parametri. Ti so definirani kot najmanjša razdalja med sledjo delca in točko interakcije elektrona in pozi-

trona. S kombinacijo opisanih lastnosti lahko sestavimo ločevalno spremenljivko b_{conf}, ki nam služi pri izbiri razpadov $Z^0 \rightarrow b\overline{b}$ [37]. Porazdelitev po omenjeni spremenljivki je prikazana na sliki 4.3. V tej analizi je bila minimalna vrednost spremenljivke b_{conf} za vsak dogodek izbrana tako, da je izkoristek označevanja znašal okrog 60 % in čistost okrog 90 %. Zveza med izkoristkom in čistostjo izbire razpadov $Z^0 \rightarrow b\overline{b}$ je razvidna s slike 4.4. Deleže dogodkov, ki ne izvirajo iz razpada $Z^0 \rightarrow b\overline{b}$ in so po izbiri glede na b_{conf} kljub vsemu ostali v vzorcu, smo ocenili s simuliranimi podatki. Tako dobljena število dogodkov ozadja ne-$b\overline{b}$ smo nato odšteli od vseh merjenih porazdelitev.

7.5 Asimetrija nabitih kaonov

V analizi smo se omejili le na nabite kaone, ki so leteli skozi centralni del detektorja in katerih gibalna količina je presegala 2 GeV. Identifikacija delcev z detektorjem RICH je bila namreč v centralnem delu detektorja DELPHI veliko bolj zanesljiva kot v obeh pokrovih.

Pri hadronizaciji kvarka B nastane več nabitih kaonov. Zanimali so nas predvsem tisti, ki so nastali pri šibkih razpadih hadronov B, saj so preostali kaoni, ki nastanejo na primer pri fragmentaciji kvarkov b iz razpadov $Z^0 \rightarrow b\overline{b}$, veliko manj učinkoviti pri označevanju naboja začetnih kvarkov. Nabite kaone iz šibkih razpadov hadronov B je mogoče se od ostalih spet ločiti, na primer zaradi že prej omenjenih večjih vpadnih parametrov, večje absolutne vrednosti gibalne količine ter njene transverzalne komponente glede na os pljuska. Te in še številne druge spremenljivke so bile vključene v nevronsko mrežo, ki se je učila na simuliranih dogodkih. Kot rezultat učenja dobimo ločevalno spremenljivko, s katero zmanjšamo delež kaonov iz fragmentacije. Učinkovitost ločevanja kaonov na osnovi te spremenljivke je razvidna iz slike 4.7.

število nabitih delcev	$\geq$	5
vsota energij vseh nabitih delcev	$>$	30 GeV
gibalna količina nabitega delca	$>$	0,4 GeV
napaka pri meritvi gibalne količine	$\leq$	10 GeV
relativna napaka gibalne količine	$\leq$	150 %
dolžina sledi, izmerjene v TPC	$\geq$	30 cm
polarni kot nabitih delcev	med	$15°$ in $165°$
vpadni parameter delcev glede na točko interakcije:		
projekcija v ravnini $R\phi$	$\leq$	10 cm
projekcija v smeri z	$\leq$	20 cm

Tabela 7.1 : Omejitvi pri izbiri dogodkov sta zapisani v prvih dveh vrsticah tabele, v preostalih so naštete zahteve, ki jim mora zadoščati vsak od nabitih delcev.

Minimalno vrednost izhodne spremenljivke nevronske mreže za identificirane nabite kaone izberemo skupaj z že prej omenjeno spremenljivko b_{conf} tako, da je signifikanca izmerjene asimetrije največja (glej sliko 4.8). Celotno število dogodkov, ki so zadoščali zgoraj opisanim zahtevam in pri tem vsebovali še vsaj en kaon, izbran na prej omenjeni način, je bilo okoli 150000. Primerjava porazdelitev po gibalni količini za simulirani in merjeni vzorec izbranih kaonov je prikazana na sliki 4.9.

Za označevanje naboja kvarka b smo izbrali tisti nabiti kaon, ki ima med vsemi izbranimi v posameznem dogodku največjo vrednost izhodne spremenljivke nevronske mreže. Simulacija je pokazala, da sta os dogodka in smer kvarka b dovolj blizu, da ju lahko izenačimo: $\theta = \theta_T$. Za polarni kot dogodka imamo še vedno na voljo dve možnosti, ki se med sabo razlikujeta za $180°$. Kot potem izberemo tako, da smer osi dogodka oklepa s smerjo izbranega nabitega kaona kot, ki je manjši od $90°$. Z nabojem izbranega kaona, pripisanim tako določenemu polarnemu kotu θ, potem označimo naboj kvarka, ki je nastal pod tem kotom. Merjeno kotno odvisno asimetrijo naprej-nazaj za nabite kaone definiramo kot:

$$A_K^{\mathrm{obs}}(\theta) = \frac{N_{K^-}(\theta) - N_{K^+}(\theta)}{N_{K^-}(\theta) + N_{K^+}(\theta)} \,, \tag{7.10}$$

kjer sta $N_{K^-}(\theta)$ in $N_{K^+}(\theta)$ števili K^- in K^+, pripisanih kotu osi θ. Kotne porazdelitvi kaonov in merjeno odvisnost asimetrije $A_K^{\mathrm{obs}}(\theta)$ od polarnega kota θ vidimo na sliki 5.2.

Ker je presek za interakcijo negativnih kaonov s snovjo v detektorju večji od preseka za interakcijo pozitivnih kaonov, se merjena asimetrija razlikuje od asimetrije pri nastanku kaonov. Razliko imenujemo snovna asimetrija in jo lahko izračunamo kar iz meritev samih, če predpostavimo, da je detektor simetričen na zamenjavo polarnega kota θ s $\pi - \theta$. V ta namen definiramo razmerje:

$$A_K^{\mathrm{mat}}(\theta) = A_K^{\mathrm{mat}}(\pi - \theta) = \frac{(N_{K^+}(\theta) + N_{K^+}(\pi - \theta)) - (N_{K^-}(\theta) + N_{K^-}(\pi - \theta))}{N_{K^+}(\theta) + N_{K^+}(\pi - \theta) + N_{K^-}(\theta) + N_{K^-}(\pi - \theta)} \,. \tag{7.11}$$

Primer kotne odvisnosti definiranega razmerja je predstavljen na sliki 5.3. Merjeno asimetrijo za nabite kaone potem popravimo tako, da ji dodamo snovno asimetrijo:

$$A_K^{\mathrm{corr}}(\theta) = \frac{A_K^{\mathrm{obs}}(\theta) + A_K^{\mathrm{mat}}(\theta)}{\Lambda(\theta)} \,, \tag{7.12}$$

vsoto pa delimo še s korekcijskim faktorjem:

$$\Lambda(\theta) = 1 - \frac{4\,\{N_{K^+}(\theta) + N_{K^+}(\pi - \theta)\}\,\{N_{K^-}(\theta) + N_{K^-}(\pi - \theta)\}}{\{N_{K^+}(\theta) + N_{K^+}(\pi - \theta) + N_{K^-}(\theta) + N_{K^-}(\pi - \theta)\}^2} \cdot$$
$$\cdot \frac{\sqrt{N_{K^-}(\theta)N_{K^+}(\theta)} - \sqrt{N_{K^-}(\pi - \theta)N_{K^+}(\pi - \theta)}}{\sqrt{N_{K^-}(\theta)N_{K^+}(\theta)} + \sqrt{N_{K^-}(\pi - \theta)N_{K^+}(\pi - \theta)}} \,, \tag{7.13}$$

ki popravi morebitno razliko v izkoristku za detekcijo kaonov v smeri naprej in smeri nazaj.

7.6   Asimetrija kvarkov b

Merjena asimetrija kaonov je merilo za asimetrijo pri razpadu $Z^0 \to b\overline{b}$, vendar se del informacije o asimetriji kvarkov izgubi, saj na primer med nabojem kaonov, ki izhajajo iz fragmentacije, in med nabojem kvarkov b ni znatne korelacije. Podobno se tudi iz pionov ali protonov, napačno identificiranih kot kaoni, ni mogoče sklepati na naboj prvotnega kvarka b. Prvotni kvark je napačno označen z nabitimi kaoni tudi zaradi mešanja $B^0 \leftrightarrow \overline{B}^0$ in $B_s^0 \leftrightarrow \overline{B}_s^0$, saj se takrat nastali kvark b pred razpadom spremeni v antikvark in obratno. Tudi brez mešanja pa se lahko zgodi, da imamo namesto razpadne verige $b \to c \to s$ razpad tipa $b \to c\overline{c}s$, kjer zaznamo nabiti kaon iz razpada delca z „napačnim" čarom: antikvarka $\overline{c}$.

Slabilni faktor $\eta_b(\theta)$ (definiran v enačbi (7.8)), ki pove, kako učinkovito je določanje $A_{FB}^{b\overline{b}}$ iz kaonske asimetrije, je moč eksperimentalno določiti z dvojnim označevanjem dogodkov. Pri tem nabite kaone izberemo na enak način kot pri merjenju asimetrije, le da tokrat zahtevamo dva, vsakega v eni polovici detektorja. Polovici ali hemisferi razmejuje ravnina, ki je pravokotna na smeri žarkov in poteka skozi interakcijsko točko elektrona in pozitrona. Za tako izbrane dogodke velja naslednja zveza:

$$\eta_b^2(\theta) = \eta_b^2(\pi - \theta) = \frac{N_K^{\mathrm{opp}}(\theta) - N_K^{\mathrm{same}}(\theta)}{N_K^{\mathrm{opp}}(\theta) + N_K^{\mathrm{same}}(\theta)}, \qquad (7.14)$$

pri čemer sta $N_K^{\mathrm{opp}}(\theta)$ in $N_K^{\mathrm{same}}(\theta)$ števili dogodkov, pri katerih imata naboja izbranih kaonov v prvem primeru nasproten predznak, v drugem pa enakega. Tudi tukaj velja, da števili $N_K^{\mathrm{opp}}(\theta)$ in $N_K^{\mathrm{same}}(\theta)$ ne vsebujeta več ozadja, saj je bilo predhodno odšteto. Simulacija pokaže, da je moč odvisnost $\eta_b^2(\theta)$ od $\cos^2 \theta$ aproksimirati s polinomom druge stopnje (glej sliko 5.6), ki smo ga zato uporabili v končni analizi podatkov.

Kvarkovsko asimetrijo $A_{FB}^{b\overline{b}}$ dobimo tako, da poiščemo minimum funkcije χ^2 z naslednjo obliko:

$$\chi^2 = \sum_{i=1}^{N_{\mathrm{bins}}} \left(\frac{\frac{A_K^{\mathrm{corr}}(\theta_i)}{\eta_b(\theta_i)} - A_{FB}^{b\overline{b}}(1 - \delta_{\mathrm{QCD}}^b)f(\theta_i)}{\sigma_i} \right)^2, \qquad (7.15)$$

kjer funkcija

$$f(\theta_i) = \frac{8}{3} \frac{\cos \theta_i}{1 + \cos^2 \theta_i} \qquad (7.16)$$

izhaja iz enačbe (7.3) in povezuje $A_{FB}^{b\overline{b}}$ ter ustrezno kotno odvisno asimetrijo. σ_i je statistična napaka količine $A_K^{\mathrm{corr}}(\theta_i)$, deljena z η_b, in se nanaša na posamezne kotne intervale θ_i. Za popravek razmazanosti kvarkovske asimetrije zaradi fragmentacije in končne hadronizacije kvarka b skrbi δ_{QCD}^b, ki ga ocenimo iz simulacije in znaša $(1.4 \pm 1.8)\%$. Analiza pokriva polarne kote v območju $0.05 \leq \cos \theta \leq 0.7$, saj sta prilagajani asimetriji pri kotih θ in $\pi - \theta$ popolnoma korelirani, kar je razvidno tudi iz enačb (7.10)-(7.13) in s slike 5.7, ki prikazuje rezultat meritve kvarkovske asimetrije za merske podatke iz leta 1994.

leto	$\sqrt{s}\,[\mathrm{GeV}]$	Izvor napake				
		η_{b}	$\delta^{\mathrm{b}}_{\mathrm{QCD}}$	normiranje ozadja	$A^{\mathrm{c\bar{c}}}_{FB}$	skupaj
1992	91,28	13,6	1,8	2,6	0,4	14,0
	89,43	16,5	1,8	2,7	0,3	16,8
1993	91,22	19,5	1,8	2,7	0,3	19,8
	93,02	21,4	1,8	2,7	0,3	21,6
1994	91,20	6,6	1,8	2,6	0,4	7,3
	89,44	14,5	1,8	1,5	0,3	14,7
1995	91,30	9,4	1,8	1,5	0,3	9,7
	92,97	22,9	1,8	1,5	0,3	23,0

Tabela 7.2 : Izvori sistematskih napak in njihove relativne vrednosti v odstotkih. Zadnja kolona predstavlja skupno napako vseh izvorov.

Z združitvijo rezultatov, izmerjenih pri podobnih težiščnih energijah, dobimo končne rezultate meritve asimetrije:

$$A^{\mathrm{b\bar{b}}}_{FB}(89,43\ \mathrm{GeV}) = 0,0427 \pm 0,0330_{\mathrm{stat}} \pm 0,0050_{\mathrm{sist}}\,,$$
$$A^{\mathrm{b\bar{b}}}_{FB}(91,24\ \mathrm{GeV}) = 0,1084 \pm 0,0096_{\mathrm{stat}} \pm 0,0077_{\mathrm{sist}}\,, \qquad (7.17)$$
$$A^{\mathrm{b\bar{b}}}_{FB}(92,99\ \mathrm{GeV}) = 0,1017 \pm 0,0353_{\mathrm{stat}} \pm 0,0171_{\mathrm{sist}}\,.$$

Sistematske napake meritev, ki so tukaj zapisane ločeno od statističnih, so obravnavane v naslednjem razdelku.

7.7　Sistematske napake

V tabeli 7.2 so zbrani prispevki k celotnim sistematskim napakam meritve $A^{\mathrm{b\bar{b}}}_{FB}$ iz vseh izvorov, upoštevanih pri oceni.

Prva sistematska napaka v tabeli je posledica statistične napake slabilnega faktorja η_{b}, ki povezuje kaonsko asimetrijo z asimetrijo kvarkov b. Ker je faktor določen na precej omejenem vzorcu izmerjenih dvojno označenih dogodkov, je prispevek te negotovosti k celotni sistematski napaki prevladujoč. Da bi se prepričali o zanesljivosti metode določanja $A^{\mathrm{b\bar{b}}}_{FB}$, smo ponovili analizo na vzorcih simuliranih dogodkov s popolnoma enakim postopkom obdelave kot pri merjenih podatkih. Vzorci so bili izbrani tako, da so se med sabo razlikovali po vhodnih vrednostih asimetrije. V vseh primerih so bili rezultati teh meritev v skladu z vhodnimi podatki.

Že prej smo omenili, da vrednost za $\delta^{\mathrm{b}}_{\mathrm{QCD}}$ izhaja iz simulacije. Njena napaka je posledica omejenega števila simuliranih dogodkov, ki smo jih imeli na voljo za oceno.

Napaka zaradi ocene deleža ozadja, ki ga predstavljajo dogodki, ki ne izhajajo iz razpadov $Z^0 \to b\overline{b}$, je majhna v primerjavi s prevladujočo napako zaradi η_b. Grobo jo zato lahko ocenimo kar iz merskih podatkov. Primerjamo število hemisfer, označenih s kvarki b, s številom merjenih dogodkov, pri katerih sta obe hemisferi označeni kot kandidatki za razpad $Z^0 \to b\overline{b}$. Pri tem sta hemisferi določeni glede na os dogodka. Dobljene številke so, ob upoštevanju vrednosti korelacije med obema hemisferama, ki jo ocenimo iz simulacije, osnova za oceno izkoristka označevanja pravih in napačnih dogodkov $Z^0 \to b\overline{b}$. S podobnim postopkom dobimo še oceno za izkoristek označevanja z nabitimi kaoni. S primerjavo tako dobljenih izmerjenih izkoristkov in ustreznih izkoristkov iz simulacije dobimo normalizacijski faktor za ozadje, ki ga dá simulacija. Ker je ozadja malo, med 5 % in 10 %, se tudi morebitne napake pri normalizaciji ne poznajo preveč. Normalizacija tako prinese 15- do 20-odstotni popravek k ozadju, kar potem vpliva na velikost $A_{FB}^{b\overline{b}}$ za največ popravek k ozadju, kar potem vpliva na velikost $A_{FB}^{b\overline{b}}$ za največ 2,7 %. V ozadju prevladujejo dogodki iz razpadov $Z^0 \to c\overline{c}$, ki jih napačno pripišemo razpadom $Z^0 \to b\overline{b}$. Tudi zanje velja asimetrija naprej-nazaj, $A_{FB}^{c\overline{c}}$. Ta asimetrija je sicer vključena v generirane vzorce, vendar pa nenatančno poznavanje njene vrednosti prinese dodatno, kvečjemu 0,4-sistematsko napako k asimetriji $A_{FB}^{b\overline{b}}$.

Deloma se vzorci, na katerih smo izmerili asimetrijo A_K^{corr} in slabilni faktor η_b, med sabo prekrivajo, zaradi česar pričakujemo korelacijo med obema vrednostima. Ocena pokaže, da je vpliv korelacije tako majhen, da spremeni celotno ocenjeno napako meritev – statistično in sistematsko skupaj – le za okoli 10^{-4}, tako da lahko ta popravek zanemarimo.

7.8 Efektivni kot elektrošibkega mešanja

Izmerjene vrednosti asimetrije (7.17) so prvi rezultati meritve. Za primerjavo z ostalimi eksperimenti moramo iz teh rezultatov izluščiti asimetrijo na polu in efektivni Weinbergov kot. Pri tem ravnamo na način, dogovorjen med štirimi eksperimenti, ki so zajemali podatke ob trkalniku LEP.

Različne meritve asimetrije v skladu z dogovori najprej preračunamo na težiščno energijo 91,26 GeV. Pri tem si pomagamo z napovedmi programskega paketa ZFITTER [17]. Različne vrednosti asimetrije pri omenjeni težiščni energiji nato združimo v eno samo povprečje:

$$A_{FB}^{b\overline{b}}(91, 26 \text{ GeV}) = 0,1043 \pm 0,0089_{\text{stat}} \pm 0,0064_{\text{sist}} . \tag{7.18}$$

Kot smo že omenili, do asimetrije na polu pridemo tako, da popravimo osnovno kvarkovsko asimetrijo:

$$A_{FB}^{0,b\overline{b}} = A_{FB}^{b\overline{b}} + \delta_{\text{QED}} + \delta_{\sqrt{s}} . \tag{7.19}$$

V člen δ_{QED} pospravimo popravke zaradi izsevanja fotonov v začetnem stanju kot tudi prispevke k asimetriji, ki so posledica izmenjave fotona ter interference med γ in Z^0, vključen pa je še zelo majhen popravek zaradi tega, ker kvarki niso brez mase. Z drugim popravkom, $\delta_{\sqrt{s}}$, poskrbimo za premik merjene asimetrije v pol Z^0. Vsi našteti popravki, prav tako kot prej izračunani s programskim paketom ZFITTER, so navedeni v tabeli 7.3. Z navedenimi popravki

Izvor popravkov	$\delta A_{FB}^{b\overline{b}}$
$\sqrt{s} \neq m_{\mathrm{Z}}$	$-0,0013$
ISR, γ, $\gamma \mathrm{Z}^0$, $\mathrm{m_b}$	$+0,0038$

Tabela 7.3 : Popravki k $A_{FB}^{b\overline{b}}$. Popravki zaradi sevanja v začetnem stanju (ISR), izmenjave γ ter interference med γ in Z^0, ki so skupaj z majhnim popravkom zaradi končne mase kvarkov b vključeni v δ_{QED}, so skupaj podani v drugi vrsti tabele. S popravkom iz prve vrste poskrbimo, da asimetrijo $A_{FB}^{b\overline{b}}$ premaknemo s težiščne energije 91,26 GeV v pol Z^0 pri težiščni energiji 91,188 GeV [13]. Vrednosti popravkov, izračunanih s paketom ZFITTER, sicer vzamemo kar iz [5].

povprečno asimetrijo (7.18) kaj hitro spremenimo v asimetrijo na polu:

$$A_{FB}^{0,b\overline{b}} = 0,1068 \pm 0,0089_{\mathrm{stat}} \pm 0,0064_{\mathrm{sist}} \,. \tag{7.20}$$

Zadnji korak je določitev $\sin^2 \theta_{\mathrm{eff}}^{\mathrm{e}}$ iz asimetrije v polu. Podobno kot smo približek k Bornovi aproksimaciji za asimetrijo v enačbi (7.6) izrazili z dvema delnima asimetrijama, tudi oblečeno asimetrijo na polu, $A_{FB}^{0,f\overline{f}}$, najprej zapišemo kot produkt oblečenih delnih asimetrij $\bar{\mathcal{A}}_{\mathrm{e}}$ in $\bar{\mathcal{A}}_{\mathrm{b}}$:

$$A_{FB}^{0,b\overline{b}} = \bar{\mathcal{A}}_{\mathrm{e}}\bar{\mathcal{A}}_{\mathrm{b}} = \frac{2(1 - 4|q_{\mathrm{f}}|\sin^2\theta_{\mathrm{eff}}^{\mathrm{e}})}{1 + \left(1 - 4|q_{\mathrm{f}}|\sin^2\theta_{\mathrm{eff}}^{\mathrm{e}}\right)^2} \cdot \frac{2(1 - 4|q_{\mathrm{f}}|\sin^2\theta_{\mathrm{eff}}^{\mathrm{b}})}{1 + \left(1 - 4|q_{\mathrm{f}}|\sin^2\theta_{\mathrm{eff}}^{\mathrm{b}}\right)^2} \,. \tag{7.21}$$
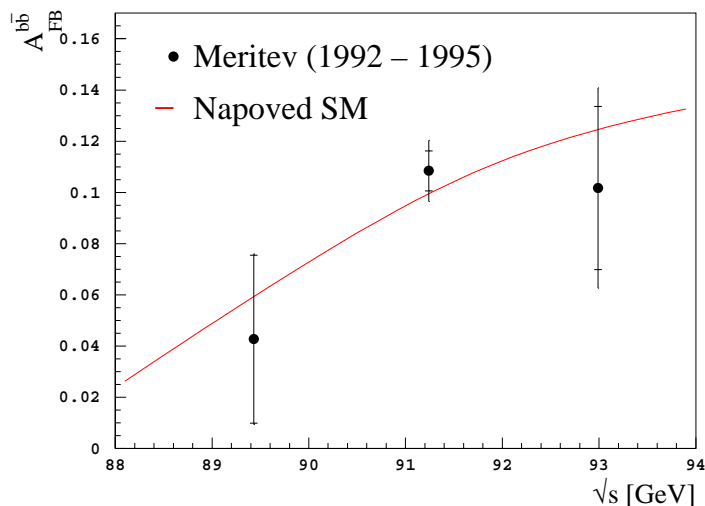
Slika 7.2 : $A_{FB}^{b\overline{b}}$ kot funkcija težiščne energije. Rezultati meritev so označeni s točkami in opremljeni z napakami. Za primerjavo je vrisana krivulja, dobljena iz standardnega modela s pomočjo programskega paketa ZFITTER. Za parametre standardnega modela je uporabljeno svetovno poprečje [13] in za maso Higgsovega bozona vrednost $M_{\mathrm{H}} = 115$ GeV.

V skladu z dogovorom med LEP-ovimi eksperimenti člen $\bar{\mathcal{A}}_{\rm b}$ izračunamo v okviru standardnega modela. Pri izračunu uporabimo nabor parametrov, ki ustrezajo povprečju vseh predhodnih meritev [13]. Korak upravičimo s šibko odvisnostjo $\bar{\mathcal{A}}_{\rm b}$ od vrednosti $\sin^2 \theta_{\rm eff}^{\rm b}$ (primerjaj odvisnost $\mathcal{A}_{\rm b}$ od $\sin^2 \theta_W$ na sliki 7.1). Z izračunano vrednostjo $\bar{\mathcal{A}}_{\rm b} = 0,934607$ [17] lahko iz izmerjene vrednosti (7.20) preko zveze (7.21) določimo $\bar{\mathcal{A}}_{\rm e}$. Iz slednje lahko potem ob upoštevanju leptonske univerzalnosti izluščimo efektivni kot elektrošibkega mešanja za leptone:

$$\sin^2 \theta_{\rm eff}^{\rm lept} = 0,2308 \pm 0,0020 \,. \tag{7.22}$$
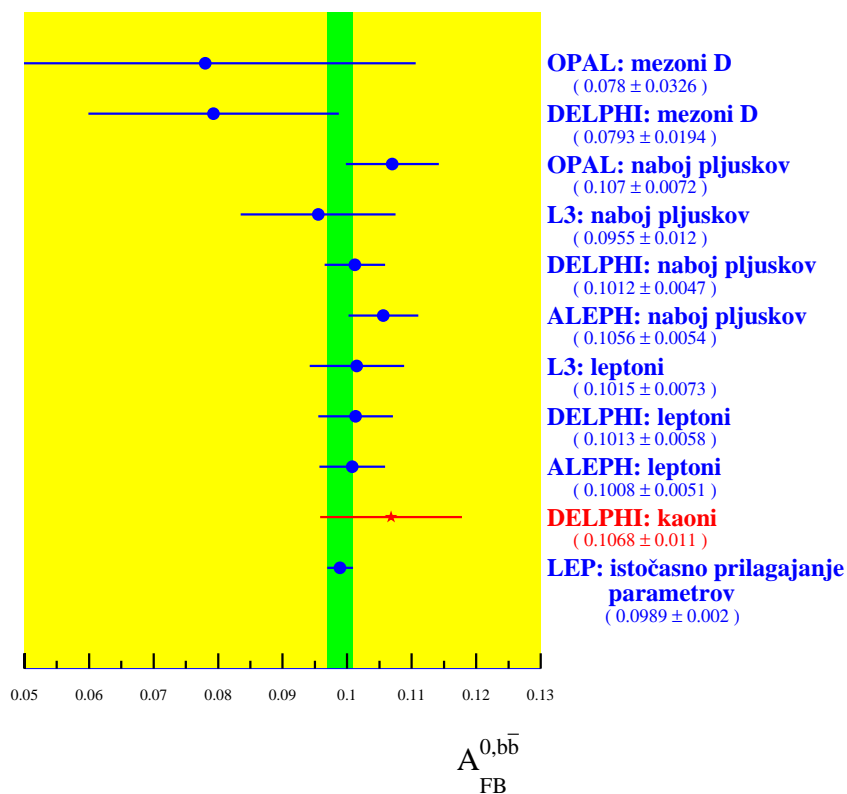
Slika 7.3 : Primerjava vrednosti asimetrije na polu, $A_{FB}^{0,\rm b\overline{b}}$, ki so jih z raznimi tehnikami označevanja naboja kvarka b izmerili različni LEP-ovi eksperimenti. Prikazana je tudi primerjava z vrednostjo, dobljeno z istočasnim prilagajanjem različnih elektrošibkih parametrov celotnim podatkom, zajetim z detektorji ob trkalniku LEP [5].

7.9 Zaključek

V disertaciji je opisana prva meritev asimetrije $A_{FB}^{\rm b\overline{b}}$ z detektorjem DELPHI, pri kateri so bili za označevanje naboja kvarkov b uporabljeni nabiti kaoni. Meritev je omogočila dobra hadronska identifikacija, pri kateri je pomembno vlogo igral detektor Čerenkovih obročev RICH. Na

sliki 7.2 vidimo primerjavo izmerjenih vrednosti za $A_{FB}^{b\overline{b}}$ pri treh težiščnih energijah s pred-videvanji standardnega modela, pri čemer so parametri modela postavljeni v svetovno po-prečje [13, 17]. Rezultati izmerjene asimetrije na polu se v okviru napak ujemajo z drugimi meritvami LEP-ovih eksperimentov, ki na naboj kvarka b sklepajo iz naboja nabitih lepto-nov [46–48], naboja pljuskov [49–52] ali pa rekonstruiranih mezonov D [53, 54]. Primer-java rezultatov je prikazana na sliki 7.3. Tudi izmerjena vrednost efektivnega elektrošibkega mešalnega kota za leptone, $\sin^2 \theta_{\text{eff}}^{\text{lept}} = 0,2308 \pm 0,0020$, se dobro ujema z dosedanjimi meri-tvami [5] (glej sliki 1.1 in 6.3).

Žal je opisana meritev premalo natačna, da bi lahko iz vrednosti efektivnega kota (7.22) po-stavili zgornjo mejo za maso Higgsovega bozona. Izkaže pa se, da je tako z vsemi posameznimi meritvami asimetrije, tudi s tistimi najbolj natančnimi. Zadovoljivo oceno zgornje meje za M_{H} je potemtakem mogoče dobiti šele z združitvijo vseh meritev asimetrij fermionskih parov (glej sliko 1.1).

Opisana meritev je zanimiva iz dveh razlogov. Prvi je ta, da je bila pri meritvi asimetrije $A_{FB}^{b\overline{b}}$ tokrat prvič uporabljena tehnika označevanja naboja kvarkov b z nabitimi kaoni. Metodo je omogočila dobra hadronska identifikacija, ki jo je pri detektorju DELPHI zagotavljala upo-raba detektorjev sevanja Čerenkova. Skupina DELPHI je tako uspela izmeriti asimetrijo $A_{FB}^{b\overline{b}}$ s štirimi različnimi načini označevanja naboja kvarka b: z nabitimi leptoni, z nabojem pljuskov, z rekonstruiranimi mezoni D in z nabitimi kaoni. Kar se tiče natančnosti izmerjenih vrednosti, je opisana metoda sicer manj natančna od metode označevanja naboja kvarkov b z nabitimi lep-toni, vendar pa primerljiva z nekaterimi rezultati metod z nabojem pljuska in boljša od tistih, dobljenih z rekonstruiranimi mezoni D (glej sliko 7.3). Drugi razlog za zanimivost meritve pa je predvsem v tem, da je metoda označevanja naboja drugačna od metod, uporabljenih pri osta-lih meritvah asimetrije z detektorjem DELPHI, zaradi česar ne pričakujemo znatnih korelacij zaradi prekrivanja izbranih vzorcev. Meritev je tako praktično v celoti neodvisna in dobljene rezultate lahko enostavno kombiniramo z rezultati ostalih meritev.

Appendix A

Extraction of $A_{FB}^{b\overline{b}}$ from the charged kaon asymmetry

A.1 From kaons to decaying quarks

The purpose of the measurement is to determine the quark asymmetry $A_{FB}^{b\overline{b}}$ by measuring the forward-backward angular dependent asymmetry for the selected charged kaons, defined as:

$$A_{K}^{\text{obs}}(\theta) \equiv \frac{N_{K^-}(\theta) - N_{K^+}(\theta)}{N_{K^-}(\theta) + N_{K^+}(\theta)} , \tag{A.1}$$

where θ is the thrust polar angle, chosen in such way that the thrust axis is pointing in the same hemisphere as the kaon momentum, with the two hemispheres in an event being defined with a plane perpendicular to the thrust axis. The thrust axis coincides to a very good approximation with the momentum direction of the original quark pair and can thus be used to define the quark direction (see also Section 5).

The measured sample of selected charged kaons contains also the contribution from the processes other than $Z^0 \to b\overline{b}$, referred to as the *background*. In order to obtain only the distributions of kaons coming from b quarks, this contribution has to be subtracted from the total number of selected kaons:

$$N_{K^\pm}(\theta) = N_{K^\pm, all}(\theta) - N_{K^\pm, bg}(\theta) . \tag{A.2}$$

Even after this subtraction the obtained distributions are still not pure in the sense that they still include contribution due to pions and protons misidentified as kaons. Since these particles are not true kaons originating from a decay chain (2.63), their charge has no significant correlation with the charge of the original quark and it should have roughly the same probability to be "wrong" or "right". For this reason, all particles passing the selection will be referred to as kaons and their charge will also be used for tagging.

The obtained number of charged kaons (A.2) used for tagging the quark charge, first has to
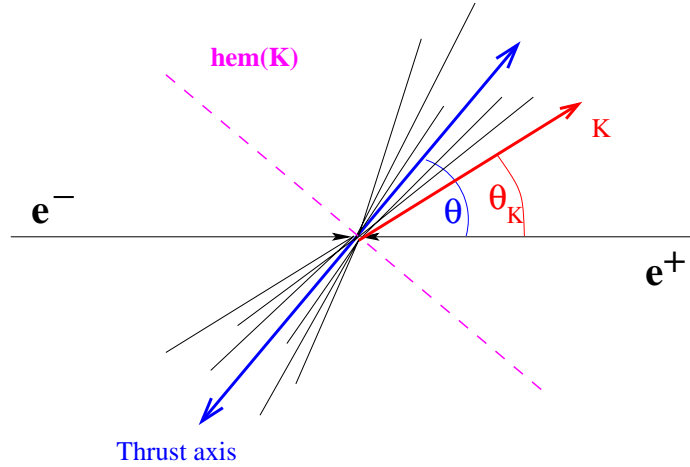
Figure A.1 : The charge of the tagging charged kaon at θ_K is attributed to the nearby thrust angle θ: the momentum of the charged kaon and the thrust axis have to point to the same hemisphere, hem(K).

be expressed with the number of quarks: $\tilde{N}_b(\theta)$ and $\tilde{N}_{\overline{b}}(\theta)$[a]. This is done in the following form:

$$
\begin{aligned}
N_{K^-}(\theta) &= \tilde{c}^-(\theta)\tilde{N}_b(\theta) + \tilde{w}^-(\theta)\tilde{N}_{\overline{b}}(\theta) \,, \\
N_{K^+}(\theta) &= \tilde{c}^+(\theta)\tilde{N}_{\overline{b}}(\theta) + \tilde{w}^+(\theta)\tilde{N}_b(\theta) \,.
\end{aligned}
\tag{A.3}
$$

Here, $\tilde{c}^-(\theta)$ is a probability for a detection of K^- belonging to a jet, originating from the b quark which was produced at the polar angle θ (see Figure A.1). Similarly, $\tilde{w}^-(\theta_K, \theta)$ is a probability that a negatively charged tagging kaon is attributed to the jet, originating from a fragmentation of an antiquark $\overline{b}$. It should be stressed that $\tilde{c}^-(\theta) \neq \tilde{c}^+(\theta)$ and $\tilde{w}^-(\theta) \neq \tilde{w}^+(\theta)$ due to the material asymmetry (see below).

In order to get to the final result, one also needs to know the numbers of *decaying* b quarks and $\overline{b}$ antiquarks at the certain polar angle:

$$
\tilde{N}_{b,\overline{b}}(\theta) = \frac{3}{8}N^{b\overline{b}}(1 + \cos^2\theta \pm \frac{8}{3}\tilde{A}^{b\overline{b}}_{FB}\cos\theta) \,.
\tag{A.4}
$$

These two angular distributions are parameterised with the asymmetry $\tilde{A}^{b\overline{b}}_{FB}$, differing from the one for *produced* quarks due to mixing. Plugging equations (A.3) – (A.4) into equation (A.1) yields the following expression for the angular dependent charged kaon asymmetry:

$$
A^{\text{obs}}_K(\theta) = \frac{\frac{8}{3}\tilde{\eta}_b(\theta)\tilde{A}^{b\overline{b}}_{FB}\frac{\cos\theta}{1+\cos^2\theta} - \tilde{r}_K(\theta)}{1 - \tilde{r}_K(\theta) \cdot \frac{8}{3}\tilde{A}^{b\overline{b}}_{FB}\frac{\cos\theta}{1+\cos^2\theta}} \,,
\tag{A.5}
$$

---

[a]Quantities marked with ˜ refer to the quarks at their decay. These quarks can be different as the produced ones due to the mixing of neutral B-mesons. This issue is treated in the Subsection A.2.

where the two quantities have been introduced:

$$\tilde{\eta}_{\mathrm{b}}(\theta) \equiv \frac{\left[\tilde{c}^-(\theta) + \tilde{c}^+(\theta)\right] - \left[\tilde{w}^-(\theta) + \tilde{w}^+(\theta)\right]}{\left[\tilde{c}^-(\theta) + \tilde{c}^+(\theta)\right] + \left[\tilde{w}^-(\theta) + \tilde{w}^+(\theta)\right]} \tag{A.6}$$

and

$$\tilde{r}_{\mathrm{K}}(\theta) \equiv \frac{\left[\tilde{c}^+(\theta) + \tilde{w}^+(\theta)\right] - \left[\tilde{c}^-(\theta) + \tilde{w}^-(\theta)\right]}{\left[\tilde{c}^+(\theta) + \tilde{w}^+(\theta)\right] + \left[\tilde{c}^-(\theta) + \tilde{w}^-(\theta)\right]} \,. \tag{A.7}$$

Coefficient (A.6), called the *dilution factor*, determines the quality of the tagging method, while the contribution (A.7) is the consequence of the fact that positive and negative kaons interact differently in the detector, i.e. this contribution is due to the so called *material asymmetry*.

The expression for the kaon asymmetry (A.5) can be further simplified, taking into account that the material asymmetry is of the order of 1 % (see Chapter 5) and $A_{FB}^{\mathrm{b\overline{b}}}$ is about 0.1. This assures that the second term in the denominator is of the order of 10^{-3} and can be safely neglected, leading to the final expression for the observed kaon asymmetry:

$$A_{\mathrm{K}}^{\mathrm{obs}}(\theta) = \frac{8}{3}\tilde{\eta}_{\mathrm{b}}(\theta)\tilde{A}_{FB}^{\mathrm{b\overline{b}}}\frac{\cos\theta}{1 + \cos^2\theta} - \tilde{r}_{\mathrm{K}}(\theta) \,. \tag{A.8}$$

A.2   Mixing of neutral B mesons

So far, the asymmetry expressions have been written for the b quarks and $\overline{\mathrm{b}}$ antiquarks according to their charge at the decay. However, the decaying $\mathrm{b}(\overline{\mathrm{b}})$ was not necessarily an (anti)quark at the production, if the mixing has occurred. For the decaying $\mathrm{b}(\overline{\mathrm{b}})$ there are thus two possibilities:

1. $\mathrm{b}(\overline{\mathrm{b}})$ was indeed produced as $\mathrm{b}(\overline{\mathrm{b}})$ or

2. $\overline{\mathrm{b}}(\mathrm{b})$ was in fact produced, but after the hadronisation to a neutral B meson and a subsequent mixing the particle decayed as $\mathrm{b}(\overline{\mathrm{b}})$.

The described case of mixing is usually parameterised by χ_{B}, the weighted time-integrated mixing parameter, which represents the total probability that a produced b decays as a $\overline{\mathrm{b}}$ and vice versa. The quoted experimental value for this quantity is [13]:

$$\chi_{\mathrm{B}} = 0.118 \pm 0.005 \,.$$

Using χ_{B}, various quantities referring to the quarks at their decay can be related to the appropriate quantities at their production. For example:

$$\tilde{N}_{\mathrm{b}}(\theta) = (1 - \chi_{\mathrm{B}})\, N_{\mathrm{b}}(\theta) + \chi_{\mathrm{B}}\, N_{\overline{\mathrm{b}}}(\theta) \,,$$
$$\tilde{N}_{\overline{\mathrm{b}}}(\theta) = (1 - \chi_{\mathrm{B}})\, N_{\overline{\mathrm{b}}}(\theta) + \chi_{\mathrm{B}}\, N_{\mathrm{b}}(\theta)$$

and

$$c^{\pm}(\theta) = (1 - \chi_{\mathrm{B}}) \, \tilde{c}^{\pm}(\theta) + \chi_{\mathrm{B}} \, \tilde{w}^{\pm}(\theta) \,,$$
$$w^{\pm}(\theta) = (1 - \chi_{\mathrm{B}}) \, \tilde{w}^{\pm}(\theta) + \chi_{\mathrm{B}} \, \tilde{c}^{\pm}(\theta) \,.$$

In this way, equations (A.3) can also be written only in terms of quantities referring to the quarks at their production:

$$N_{\mathrm{K^-}}(\theta) = c^-(\theta)N_{\mathrm{b}}(\theta) + w^-(\theta)N_{\overline{\mathrm{b}}}(\theta) \,,$$
$$N_{\mathrm{K^+}}(\theta) = c^+(\theta)N_{\overline{\mathrm{b}}}(\theta) + w^+(\theta)N_{\mathrm{b}}(\theta) \,. \tag{A.9}$$

Also the angular distributions for quarks at the production:

$$N_{\mathrm{b},\overline{\mathrm{b}}}(\theta) = \frac{3}{8}N^{\mathrm{b}\overline{\mathrm{b}}}(1 + \cos^2\theta \pm \frac{8}{3}A_{FB}^{\mathrm{b}\overline{\mathrm{b}}}\cos\theta) \tag{A.10}$$

can be parameterised with the desired asymmetry $A_{FB}^{\mathrm{b}\overline{\mathrm{b}}}$:

$$A_{FB}^{\mathrm{b}\overline{\mathrm{b}}} = \frac{\tilde{A}_{FB}^{\mathrm{b}\overline{\mathrm{b}}}}{1 - 2\chi_{\mathrm{B}}} \,. \tag{A.11}$$

Since the mixing factor can now be absorbed into the dilution factor:

$$\eta_{\mathrm{b}}(\theta) \equiv \frac{\left[c^-(\theta) + c^+(\theta)\right] - \left[w^-(\theta) + w^+(\theta)\right]}{\left[c^-(\theta) + c^+(\theta)\right] + \left[w^-(\theta) + w^+(\theta)\right]} = \tilde{\eta}_{\mathrm{b}}(\theta)(1 - 2\chi_{\mathrm{B}}) \,, \tag{A.12}$$

while the contribution due to the material asymmetry (A.7) stays the same:

$$r_{\mathrm{K}}(\theta) \equiv \frac{\left[c^+(\theta) + w^+(\theta)\right] - \left[c^-(\theta) + w^-(\theta)\right]}{\left[c^+(\theta) + w^+(\theta)\right] + \left[c^-(\theta) + w^-(\theta)\right]} = \tilde{r}_{\mathrm{K}}(\theta) \,, \tag{A.13}$$

the observed kaon asymmetry (A.8) can be simply related to the forward-backward asymmetry $A_{FB}^{\mathrm{b}\overline{\mathrm{b}}}$ of the produced b quarks:

$$A_{\mathrm{K}}^{\mathrm{obs}}(\theta) = \frac{8}{3}\eta_{\mathrm{b}}(\theta)A_{FB}^{\mathrm{b}\overline{\mathrm{b}}}\frac{\cos\theta}{1 + \cos^2\theta} - r_{\mathrm{K}}(\theta) \,. \tag{A.14}$$

By measuring the charged kaon forward-backward asymmetry, one could therefore determine $A_{FB}^{\mathrm{b}\overline{\mathrm{b}}}$ according to (A.14). However, in order to do this, both coefficients, $\eta_{\mathrm{b}}(\theta)$ and $r_{\mathrm{K}}(\theta)$, should be known. It turns out (see below) that they can both be extracted from the measured data.

An additional remark should be made here. From equations (A.11) and (A.13) one can argue that the asymmetry would have been impossible to measure in case of *complete mixing*, with $\chi_{\mathrm{B}} = 1/2$. In such case the produced b($\overline{\mathrm{b}}$) would have had exactly the same probability to decay as b or $\overline{\mathrm{b}}$ and all information about the primary quark charge would have been lost. Fortunately, this is not the case, since χ_{B} is far from the critical value.

A.3 Asymmetries of single-tagged and double-tagged events

For the most convenient derivation of the final equations used for extraction of the $A_{FB}^{b\overline{b}}$ the tagging coefficients c and w are further parameterised, taking into account the underlying physics. Namely, the tagging efficiencies comprise probabilities for the production of tagging kaons, interactions of the kaons in the detector, and efficiencies for the kaon identification. The three effects can be factorized in the following expressions:

$$
\begin{aligned}
c^{\pm}(\theta) &= c_0(\theta)\, \epsilon(\theta) \left[1 \pm r_{\mathrm{K}}(\theta)\right] , \\
w^{\pm}(\theta) &= w_0(\theta)\, \epsilon(\theta) \left[1 \pm r_{\mathrm{K}}(\theta)\right] ,
\end{aligned}
\tag{A.15}
$$

where $\epsilon(\theta)$ indicates the efficiency for the identification of tagging kaons, while $r_{\mathrm{K}}(\theta)$ is the material asymmetry already defined in (A.13). The so-called *sample probability* for kaons that correctly (falsely) tag the charge of the primary b-quarks, $c_0(\theta)$ ($w_0(\theta)$), is also a function of the polar angle θ. This is a consequence of a fact that, apart from true kaons, the samples of tagging kaons contain also fractions of misidentified pions and protons that dilute the tagging information. As the purity of the tagging kaon sample varies with $\cos\theta$, the coefficients $c_0(\theta)$ and $w_0(\theta)$ become functions of $\cos\theta$, too.

Plugging relations (A.10) and (A.15) into equations (A.9) yields the following set of expressions:

$$
N_{\mathrm{K}^-}(\theta) = \frac{3}{8} N^{b\overline{b}}\, \epsilon(\theta) \left[1 - r_{\mathrm{K}}(\theta)\right] \left[(c_0 + w_0)(1 + \cos^2\theta) + (c_0 - w_0)\frac{8}{3} A_{FB}^{b\overline{b}} \cos\theta\right] , \tag{A.16}
$$

$$
N_{\mathrm{K}^+}(\theta) = \frac{3}{8} N^{b\overline{b}}\, \epsilon(\theta) \left[1 + r_{\mathrm{K}}(\theta)\right] \left[(c_0 + w_0)(1 + \cos^2\theta) - (c_0 - w_0)\frac{8}{3} A_{FB}^{b\overline{b}} \cos\theta\right] . \tag{A.17}
$$

Also the expressions for the opposite polar angles will be needed:

$$
\begin{aligned}
N_{\mathrm{K}^-}(\pi - \theta) = &\frac{3}{8} N^{b\overline{b}}\, \epsilon(\pi - \theta) \left[1 - r_{\mathrm{K}}(\pi - \theta)\right] \\
&\cdot \left[(c_0 + w_0)(1 + \cos^2\theta) - (c_0 - w_0)\frac{8}{3} A_{FB}^{b\overline{b}} \cos\theta\right] ,
\end{aligned}
\tag{A.18}
$$

$$
\begin{aligned}
N_{\mathrm{K}^+}(\pi - \theta) = &\frac{3}{8} N^{b\overline{b}}\, \epsilon(\pi - \theta) \left[1 + r_{\mathrm{K}}(\pi - \theta)\right] \\
&\cdot \left[(c_0 + w_0)(1 + \cos^2\theta) + (c_0 - w_0)\frac{8}{3} A_{FB}^{b\overline{b}} \cos\theta\right] .
\end{aligned}
\tag{A.19}
$$

These expressions can then be used to obtain the following equations one is interested in.

First, the dilution factor can be given in a new form:

$$
\eta_{\mathrm{b}}(\theta) = \frac{c_0(\theta) - w_0(\theta)}{c_0(\theta) + w_0(\theta)} , \tag{A.20}
$$

where the angular dependence is due to the purity of the tagging sample. On the other hand, the observed asymmetry stays the same as in (A.14):

$$A_{\mathrm{K}}^{\mathrm{obs}}(\theta) = \frac{8}{3}\eta_{\mathrm{b}}(\theta)A_{FB}^{\mathrm{b\bar{b}}}\frac{\cos\theta}{1+\cos^2\theta} - r_{\mathrm{K}}(\theta) \,.$$

As already mentioned, the two coefficients in (A.14) can be extracted from the measured data. In order to express the material asymmetry, $r_{\mathrm{K}}(\theta)$, the following ratio is introduced:

$$R(\theta) = \frac{N_{\mathrm{K}^+}(\theta) + N_{\mathrm{K}^+}(\pi - \theta)}{N_{\mathrm{K}^-}(\theta) + N_{\mathrm{K}^-}(\pi - \theta)} \,. \tag{A.21}$$

Using equations (A.16)–(A.19) and assuming the material asymmetry to be forward-backward symmetric ($r_{\mathrm{K}}(\theta) = r_{\mathrm{K}}(\pi - \theta)$), $R(\theta)$ and $r_{\mathrm{K}}(\theta)$ can be related as

$$R(\theta) = \frac{1 + r_{\mathrm{K}}(\theta)}{1 - r_{\mathrm{K}}(\theta)}\left[1 - \lambda(\theta)\right] \,, \tag{A.22}$$

where the symbol $\lambda(\theta)$ denotes

$$\lambda(\theta) = \frac{16}{3}\,\eta_{\mathrm{b}}(\theta)\,A_{FB}^{\mathrm{b\bar{b}}}\frac{\cos\theta}{1+\cos^2\theta}\frac{1-\Omega(\theta)}{1+\Omega(\theta)} \,, \tag{A.23}$$

with $\Omega(\theta)$ being a ratio of efficiencies at the opposite polar angles:

$$\Omega(\theta) = \frac{\epsilon(\pi - \theta)}{\epsilon(\theta)} = \sqrt{\frac{N_{\mathrm{K}^-}(\pi - \theta)N_{\mathrm{K}^+}(\pi - \theta)}{N_{\mathrm{K}^-}(\theta)N_{\mathrm{K}^+}(\theta)}} \,. \tag{A.24}$$

Expression for $R(\theta)$ contains also terms of higher order in $\lambda(\theta)$. However, these can be neglected, since $\eta_{\mathrm{b}}(\theta)$ and $A_{FB}^{\mathrm{b\bar{b}}}$ are of the order of 0.3 and 0.1, respectively (see, for example, Figures 5.6 and 5.7). In addition to this, both according to the measured and simulated kaon distributions, the ratio

$$\frac{1 - \Omega(\theta)}{1 + \Omega(\theta)} = \frac{\sqrt{N_{\mathrm{K}^-}(\theta)N_{\mathrm{K}^+}(\theta)} - \sqrt{N_{\mathrm{K}^-}(\pi - \theta)N_{\mathrm{K}^+}(\pi - \theta)}}{\sqrt{N_{\mathrm{K}^-}(\theta)N_{\mathrm{K}^+}(\theta)} + \sqrt{N_{\mathrm{K}^-}(\pi - \theta)N_{\mathrm{K}^+}(\pi - \theta)}} \tag{A.25}$$

is of the order of 1 %.

Having $R(\theta)$ and $\lambda(\theta)$ defined, the ratio $A_{\mathrm{K}}^{\mathrm{mat}}(\theta)$

$$A_{\mathrm{K}}^{\mathrm{mat}}(\theta) = A_{\mathrm{K}}^{\mathrm{mat}}(\pi - \theta) = \frac{(N_{\mathrm{K}^+}(\theta) + N_{\mathrm{K}^+}(\pi - \theta)) - (N_{\mathrm{K}^-}(\theta) + N_{\mathrm{K}^-}(\pi - \theta))}{N_{\mathrm{K}^+}(\theta) + N_{\mathrm{K}^+}(\pi - \theta) + N_{\mathrm{K}^-}(\theta) + N_{\mathrm{K}^-}(\pi - \theta)} \,. \tag{5.2}$$

can be used in the expression for material asymmetry:

$$r_{\mathrm{K}}(\theta) = A_{\mathrm{K}}^{\mathrm{mat}}(\theta) + \frac{2\,\lambda(\theta)R(\theta)}{(R(\theta) + 1)^2} \,. \tag{A.26}$$

Replacing $r_K(\theta)$ in (A.14) with the right-hand side of the above equation then yields:

$$
\begin{aligned}
A_K^{\text{obs}} + A_K^{\text{mat}} &= \frac{8}{3} \, \eta_b(\theta) \, A_{FB}^{b\bar{b}} \frac{\cos\theta}{1 + \cos^2\theta} - \frac{2 \, \lambda(\theta) R(\theta)}{(R(\theta) + 1)^2} \\
&= \frac{8}{3} \, \eta_b(\theta) \, A_{FB}^{b\bar{b}} \frac{\cos\theta}{1 + \cos^2\theta} \left(1 - \frac{4R(\theta)}{(R(\theta) + 1)^2} \frac{1 - \Omega(\theta)}{1 + \Omega(\theta)} \right) \qquad \text{(A.27)} \\
&= \frac{8}{3} \, \eta_b(\theta) \, A_{FB}^{b\bar{b}} \frac{\cos\theta}{1 + \cos^2\theta} \, \Lambda(\theta) \, .
\end{aligned}
$$

By combining equations (A.21)–(A.25) with $\Lambda(\theta)$ as it is introduced in (A.27),

$$
\Lambda(\theta) = 1 - \frac{4R(\theta)}{(R(\theta) + 1)^2} \frac{1 - \Omega(\theta)}{1 + \Omega(\theta)} \, , \qquad \text{(A.28)}
$$

it is easy to see that the definition (A.28) coincides with the one in equation (5.4). Equation (A.27) also implies that the ratio of the corrected kaon asymmetry,

$$
A_K^{\text{corr}}(\theta) = \frac{A_K^{\text{obs}}(\theta) + A_K^{\text{mat}}(\theta)}{\Lambda(\theta)} \, ,
$$

which can be expressed only by numbers of selected tagging kaons, and of the dilution factor $\eta_b(\theta)$ is directly proportional to

$$
A_{FB}^{b\bar{b}} \, f(\theta) = \frac{8}{3} A_{FB}^{b\bar{b}} \frac{\cos\theta}{1 + \cos^2\theta} \, ,
$$

as it is assumed in the construction of the χ^2-function, given in equation (5.8). Assuming the dilution factor is forward-backward symmetric (see below), the fact that $f(\theta)$ is an odd function of $\cos\theta$, implies the same behaviour also for $A_K^{\text{corr}}(\theta)$:

$$
A_K^{\text{corr}}(\pi - \theta) = -A_K^{\text{corr}}(\theta) \, . \qquad \text{(A.29)}
$$

This is a direct consequence of the described procedure where all statistical fluctuations of A_K^{obs} that could result in breaking the rule (A.29), are absorbed by a material asymmetry or by a difference in efficiencies.

The dilution factor η_b in equation (A.20) can be expressed by an asymmetry of double-tagged events

$$
A_{\text{double}}(\theta) = A_{\text{double}}(\pi - \theta) = \frac{N_K^{\text{opp}}(\theta) - N_K^{\text{same}}(\theta)}{N_K^{\text{opp}}(\theta) + N_K^{\text{same}}(\theta)} \, , \qquad \text{(A.30)}
$$

where $N_K^{\text{opp}}(\theta)$ ($N_K^{\text{same}}(\theta)$) stands for the number of events where the two tagging kaons in the opposite hemispheres have opposite (same) charge. The ratio is forward-backward symmetric since events at θ and $\pi - \theta$ (the angle is referring to the first tagging kaon) are attributed to the same thrust angle.

To connect the dilution factor to the asymmetry of double-tagged events (A.30), the number of latter has to be written in terms of probabilities for correct and wrong kaon tagging of the b-quark charge:

$$
\begin{aligned}
N_{\mathrm{K^-K^-}}(\theta) &= w^-(\pi - \theta)\, c^-(\theta)\, N_{\mathrm{b}}(\theta) + c^-(\pi - \theta)\, w^-(\theta)\, N_{\overline{\mathrm{b}}}(\theta)\,, \\
N_{\mathrm{K^+K^+}}(\theta) &= c^+(\pi - \theta)\, w^+(\theta)\, N_{\mathrm{b}}(\theta) + w^+(\pi - \theta)\, c^+(\theta)\, N_{\overline{\mathrm{b}}}(\theta)\,, \\
N_{\mathrm{K^-K^+}}(\theta) &= c^+(\pi - \theta)\, c^-(\theta)\, N_{\mathrm{b}}(\theta) + w^+(\pi - \theta)\, w^-(\theta)\, N_{\overline{\mathrm{b}}}(\theta)\,, \\
N_{\mathrm{K^+K^-}}(\theta) &= w^-(\pi - \theta)\, w^+(\theta)\, N_{\mathrm{b}}(\theta) + c^-(\pi - \theta)\, c^+(\theta)\, N_{\overline{\mathrm{b}}}(\theta)\,.
\end{aligned}
\tag{A.31}
$$

Here θ is the polar angle corresponding to the first tagging particle indicated in the subscripts of symbols on the left-hand side of the relations. Having factorizations (A.15) in mind, it is easy to prove the following equations for the products of tagging probabilities:

$$
\begin{aligned}
c^+(\pi - \theta)\, c^-(\theta) &= c^-(\pi - \theta)\, c^+(\theta)\,, \\
w^+(\pi - \theta)\, w^-(\theta) &= w^-(\pi - \theta)\, w^+(\theta)\,, \\
c^+(\pi - \theta)\, w^-(\theta) &= w^-(\pi - \theta)\, c^+(\theta)\,, \\
c^-(\pi - \theta)\, w^+(\theta) &= w^+(\pi - \theta)\, c^-(\theta)\,, \\
c^+(\pi - \theta)\, w^+(\theta) &= w^+(\pi - \theta)\, c^+(\theta)\,, \\
c^-(\pi - \theta)\, w^-(\theta) &= w^-(\pi - \theta)\, c^-(\theta)\,, \\
c^+(\pi - \theta)\, w^+(\theta) &= w^+(\pi - \theta)\, c^+(\theta)\,.
\end{aligned}
\tag{A.32}
$$

The first two relations in (A.31) determine the total number of same sign double-tagged events, while the last two relations define all double-tagged events with the opposite charge of the two tagging kaons:

$$
\begin{aligned}
N_{\mathrm{K}}^{\mathrm{same}}(\theta) &= N_{\mathrm{K}}^{\mathrm{same}}(\pi - \theta) = N_{\mathrm{K^-K^-}}(\theta) + N_{\mathrm{K^+K^+}}(\theta)\,, \\
N_{\mathrm{K}}^{\mathrm{opp}}(\theta) &= N_{\mathrm{K}}^{\mathrm{opp}}(\pi - \theta) = N_{\mathrm{K^-K^+}}(\theta) + N_{\mathrm{K^+K^-}}(\theta)\,.
\end{aligned}
\tag{A.33}
$$

The asymmetry of the two types of events defined above reads:

$$
\frac{N_{\mathrm{K}}^{\mathrm{opp}}(\theta) - N_{\mathrm{K}}^{\mathrm{same}}(\theta)}{N_{\mathrm{K}}^{\mathrm{opp}}(\theta) + N_{\mathrm{K}}^{\mathrm{same}}(\theta)} = \frac{c^-(\theta) - w^+(\theta)}{c^-(\theta) + w^+(\theta)} \cdot \frac{c^+(\pi - \theta) - w^-(\pi - \theta)}{c^+(\pi - \theta) + w^-(\pi - \theta)}\,,
\tag{A.34}
$$

where equations (A.32) were taken into account. The factorization of the tagging efficiencies (A.15) further simplifies the expression for the asymmetry of double-tagged events:

$$
\frac{N_{\mathrm{K}}^{\mathrm{opp}}(\theta) - N^{\mathrm{same}}(\theta)}{N_{\mathrm{K}}^{opp}(\theta) + N_{\mathrm{K}}^{like}(\theta)} = \eta_{\mathrm{b}}^2(\theta) + \mathcal{O}(r_{\mathrm{K}}^2)\,.
\tag{A.35}
$$

Note that the efficiencies for identification of tagging kaons cancel out completely, while for the material asymmetry there remain only the terms with $r_{\mathrm{K}}(\theta)$ to the power of at least two. Since the material asymmetry is of the order of 1 %, these terms can be safely neglected, yielding finally the expression (5.5):

$$
\eta_{\mathrm{b}}^2(\theta) = \eta_{\mathrm{b}}^2(\pi - \theta) = \frac{N_{\mathrm{K}}^{\mathrm{opp}}(\theta) - N_{\mathrm{K}}^{\mathrm{same}}(\theta)}{N_{\mathrm{K}}^{\mathrm{opp}}(\theta) + N_{\mathrm{K}}^{\mathrm{same}}(\theta)}\,.
$$

Appendix B

Figures of event distributions, asymmetries, etc.

B.1 Momentum spectrum of kaons

Momentum spectrum of selected kaons from measured and from simulated $b\bar{b}$-decay candidates passing the selection criteria described in the Section 4.4 are shown here for all years of data taking. All distributions are normalized and drawn after applying the cut on the minimum value of momentum at 2 GeV. Note that plots for 1993 and 1995 include off-peak data, too.
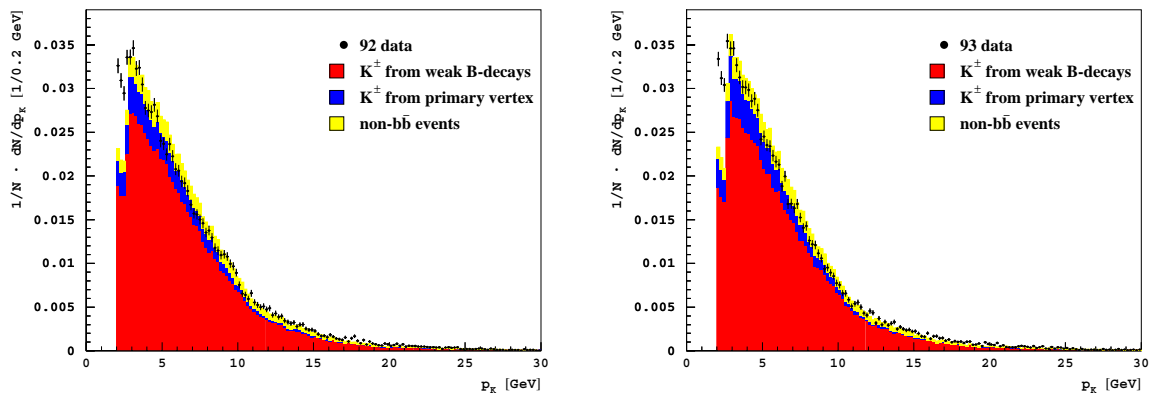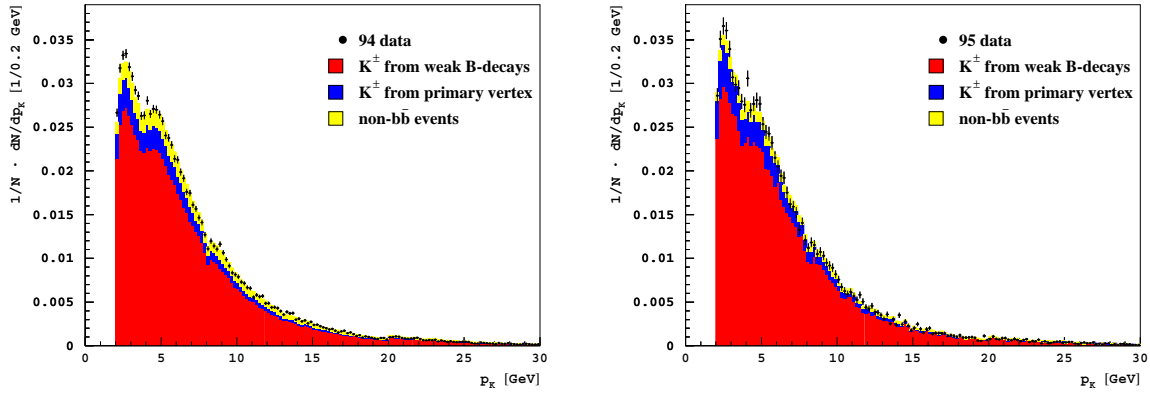
B.2   Angular distributions of kaons

Angular distribution of selected kaons from measured b$\bar{\text{b}}$-decay candidates, used already in Subsection B.1. Non-b$\bar{\text{b}}$ contribution to the selected samples was estimated using the simulated data. The central region of the polar angle interval $-0.05 \leq \cos\theta \leq 0.05$ is excluded from all plots and calculations to avoid additional effects due to interactions in the central high voltage TPC plate. Shapes of the simulated distributions (MC normalized to the number of measured events) are also shown in comparison to the measured ones.

Data taken at the Z^0 peak
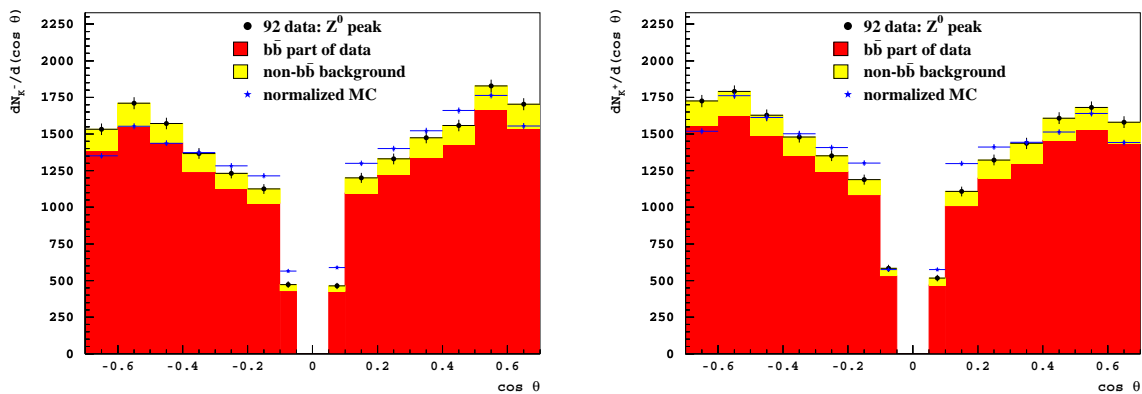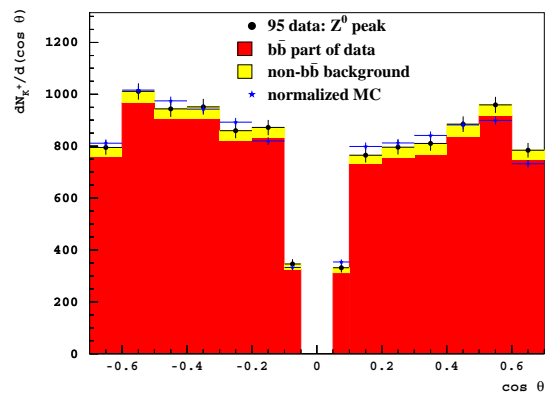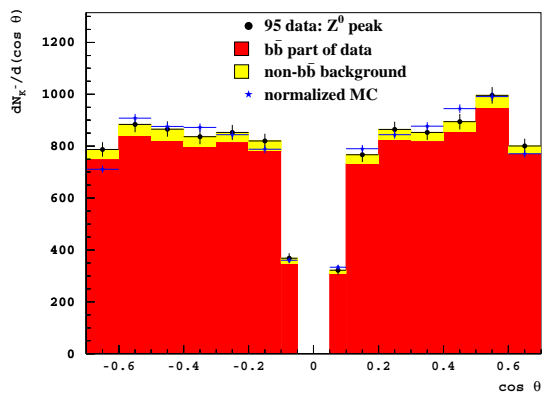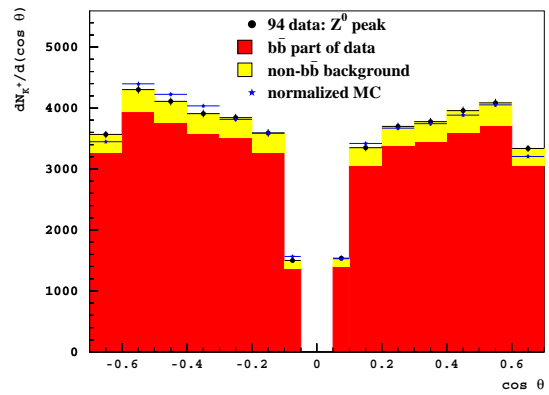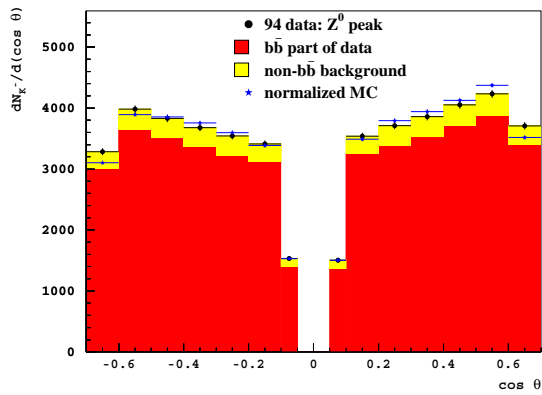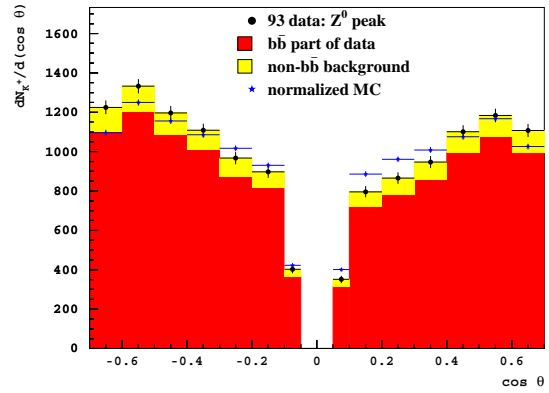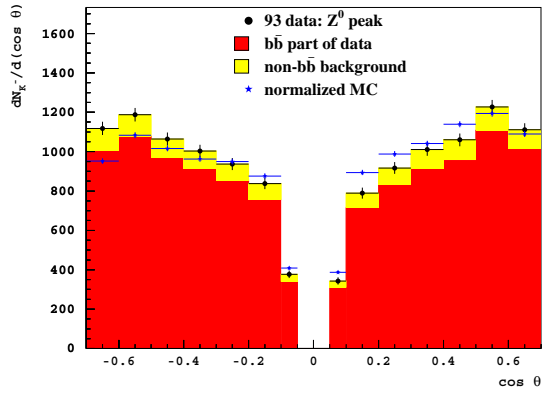
Data taken below the Z^0 peak
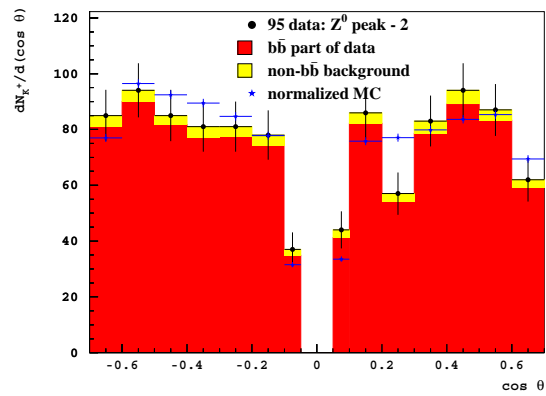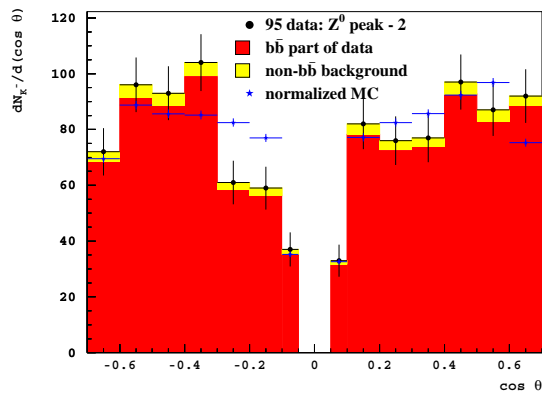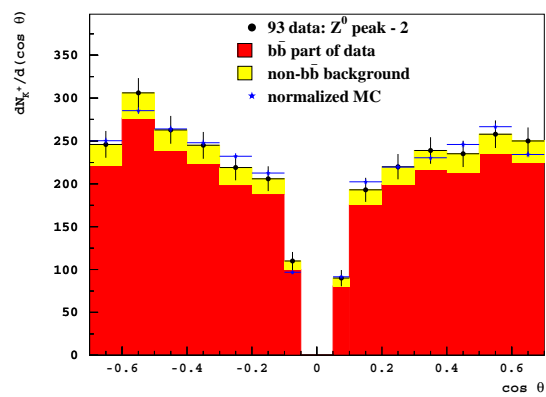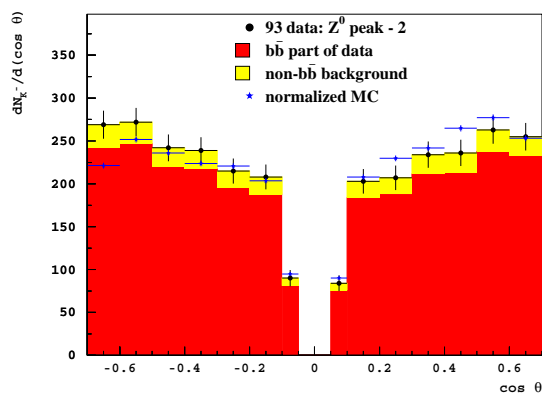
Data taken above the Z^0 peak
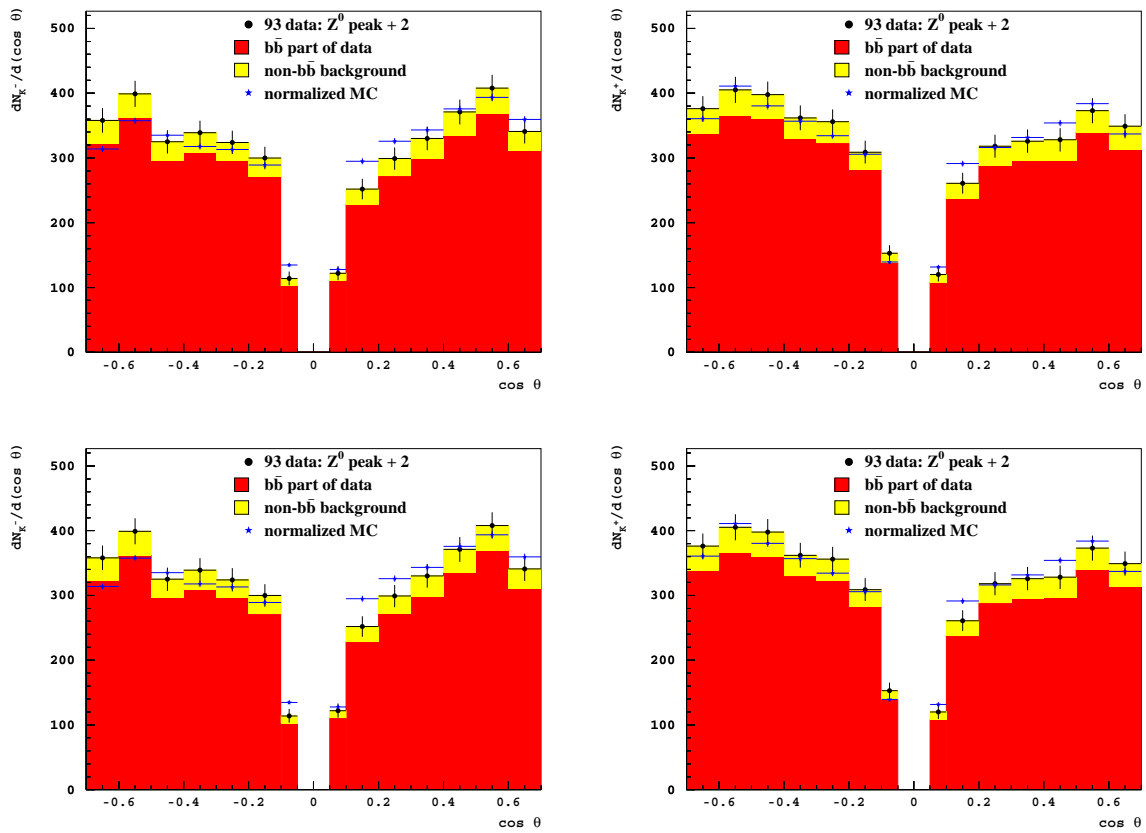
B.3 Observed kaon asymmetries

The observed kaon asymmetries for selected charged kaons as defined in (5.1). Non-$b\bar{b}$ contribution was estimated using the simulated data and subtracted from the measured kaon distributions before asymmetries were calculated.

Data taken at the Z^0 peak
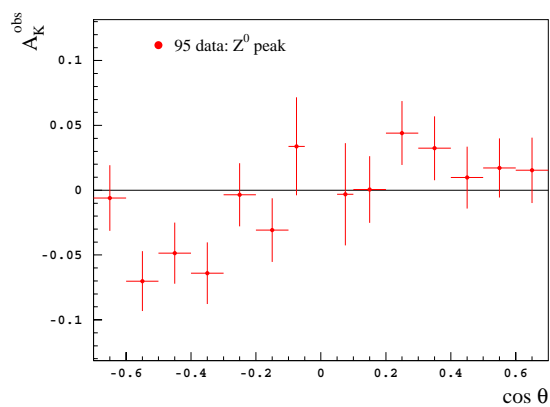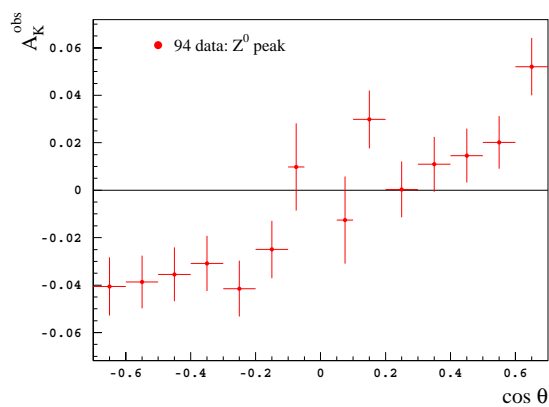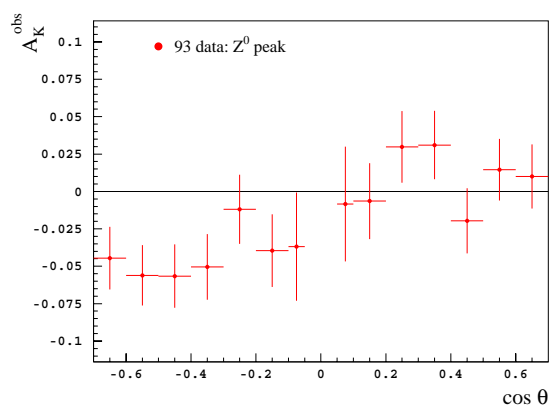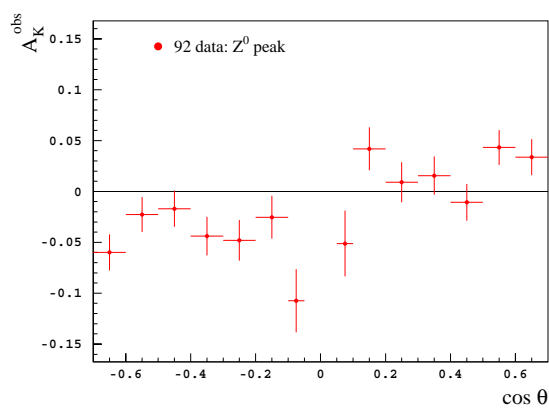
Data taken below the Z^0 peak
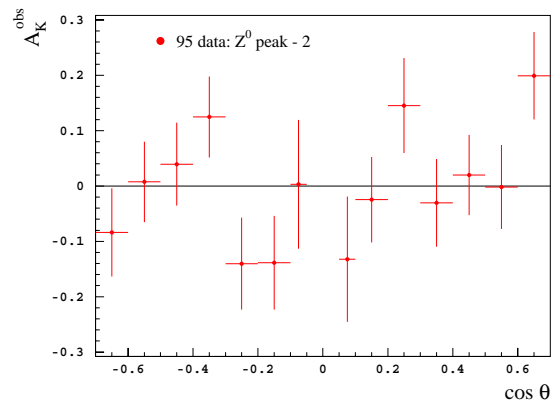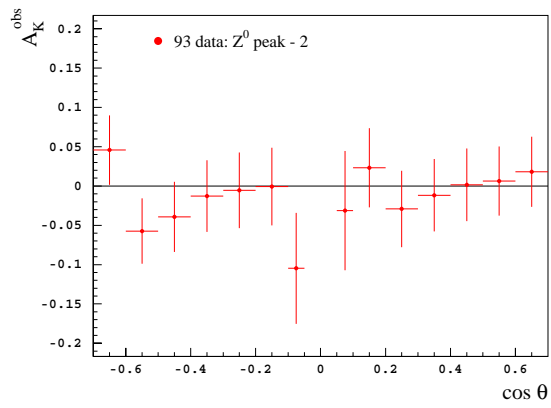
Data taken above the Z^0 peak
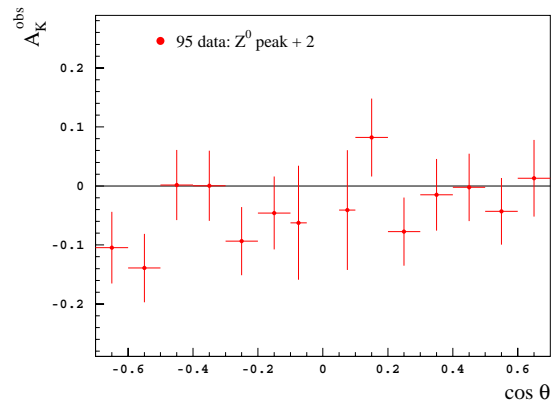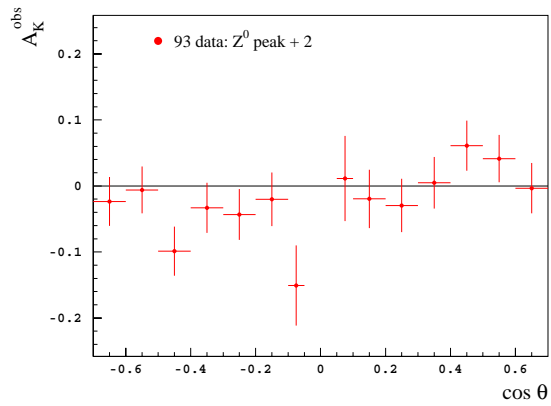
B.4   Material kaon asymmetries

Material kaon asymmetries estimated on the measured samples using the ratio (5.2) is shown below for all measured data subsets. Note that the opposite bins are completely correlated, since the ratio (5.2) is defined to be forward-backward *symmetric*.

Data taken at the Z^0 peak
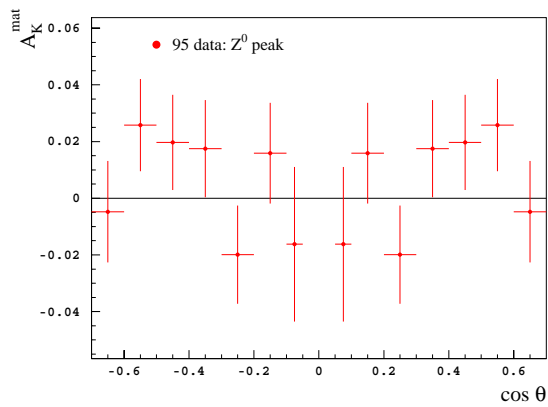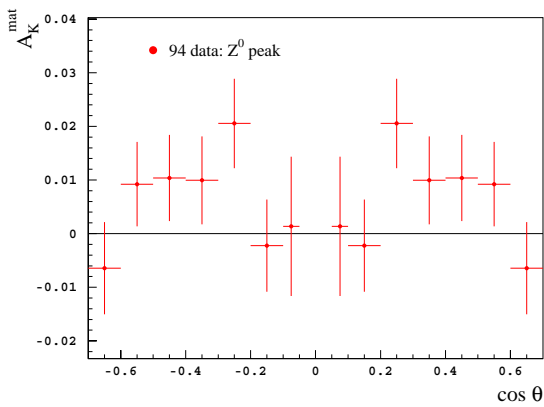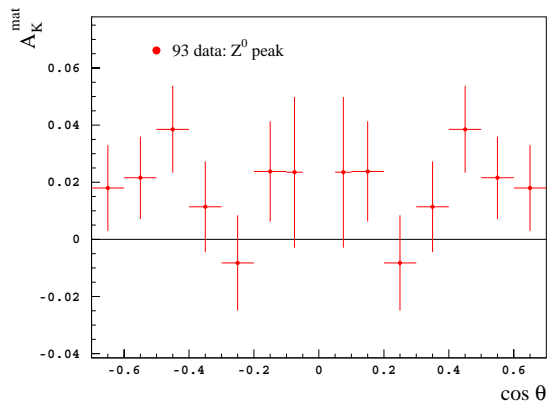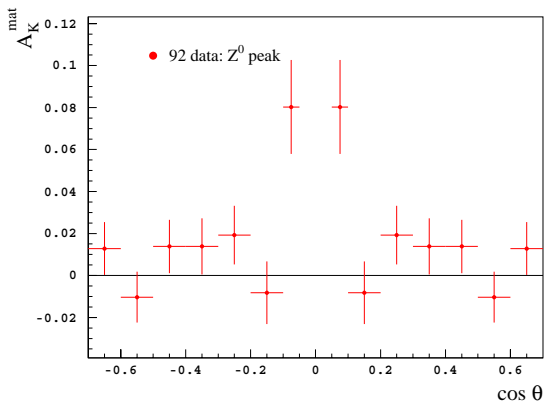
Data taken below the Z^0 peak
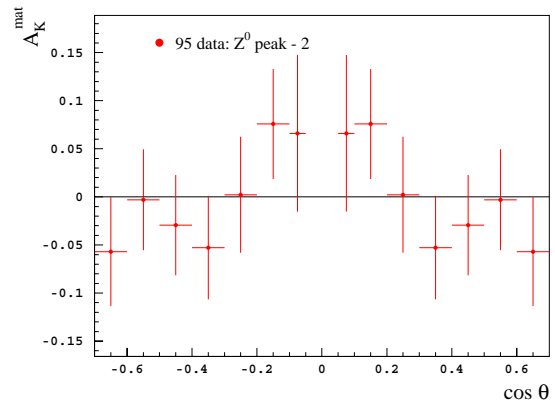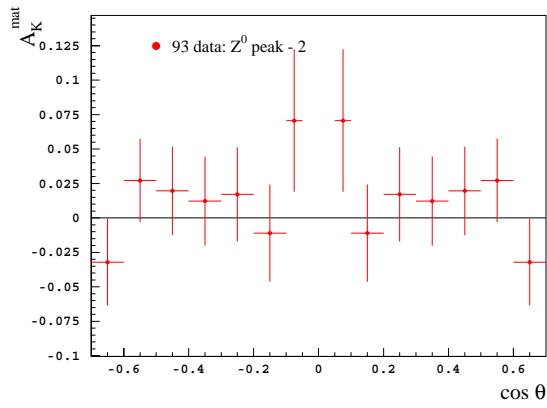
Data taken above the Z^0 peak
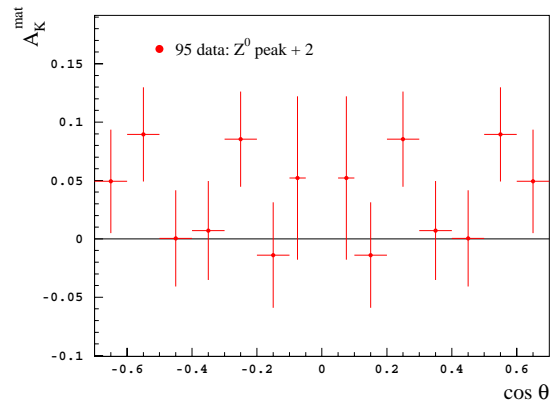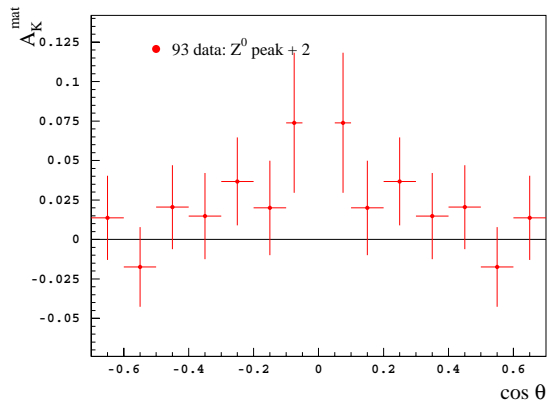
B.5   Corrected kaon asymmetries

Final shape of corrected kaon asymmetries calculated according to Equation (5.3). The absolute values of the asymmetry are the same for the two opposite bins in $\cos\theta$ due to the applied correction procedure.

Data taken at the Z^0 peak
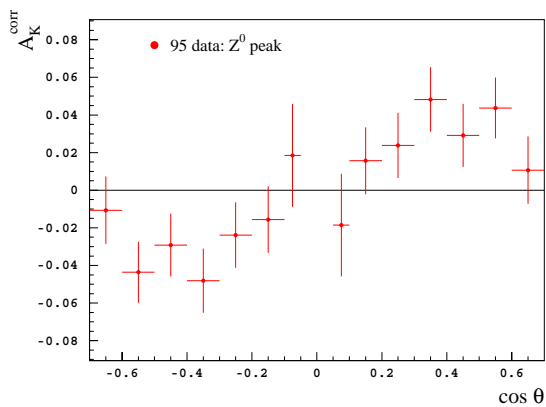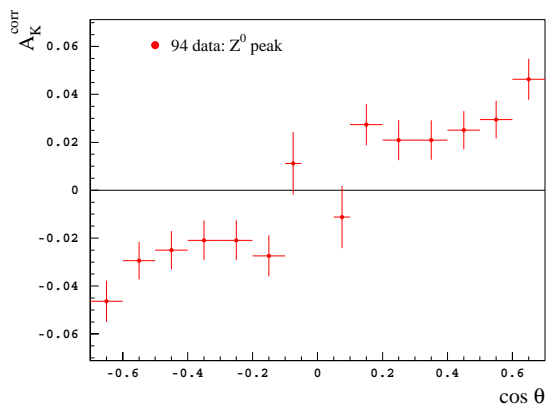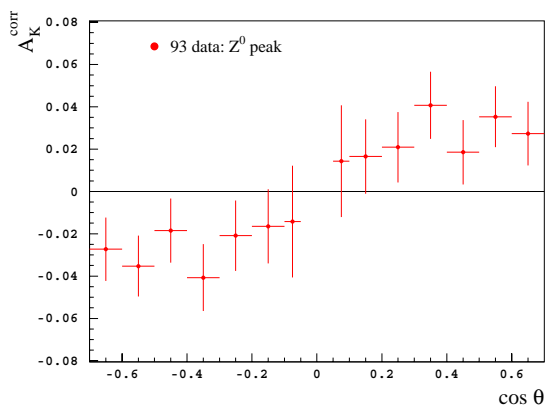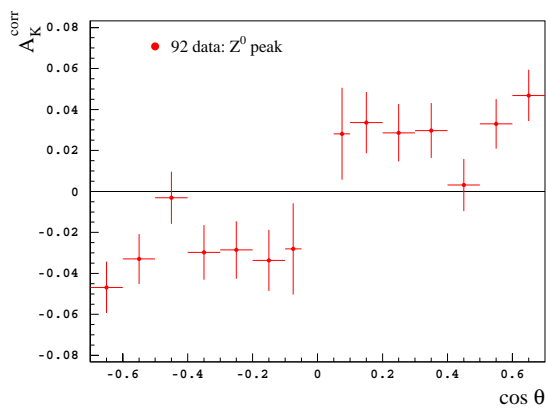
Data taken below the Z^0 peak
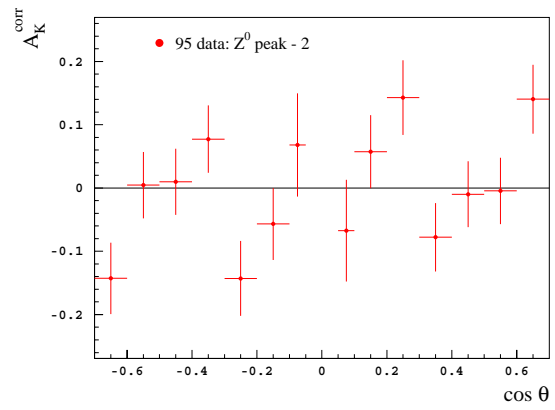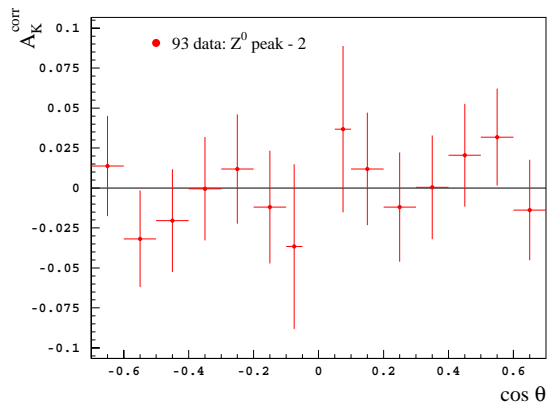
Data taken above the Z^0 peak
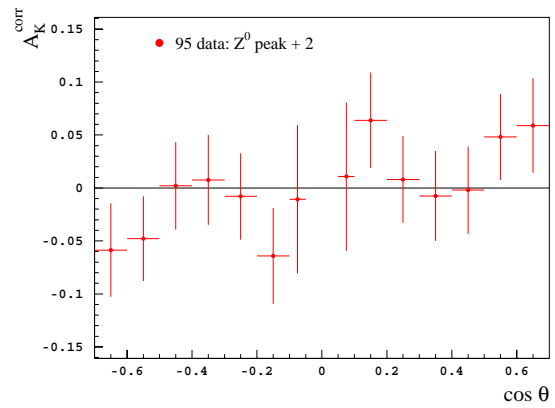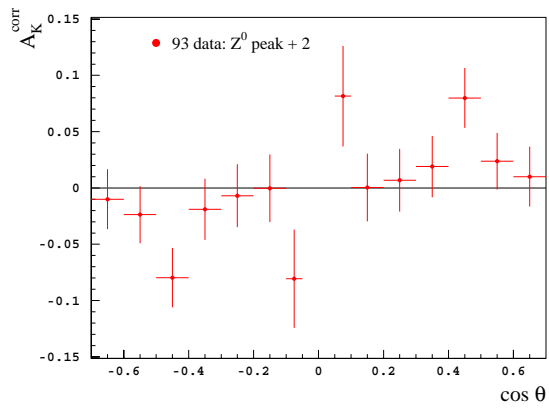
B.6   Angular distributions of double-tagged events

Number of double-tagged events as a function of $\cos\theta$, where θ is the polar angle corresponding to the first tagging particle in an event. The comments about the shown histograms are the same as already given in B.2.

Data taken at the Z^0 peak
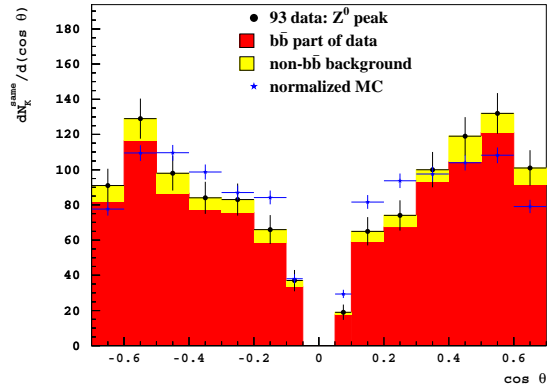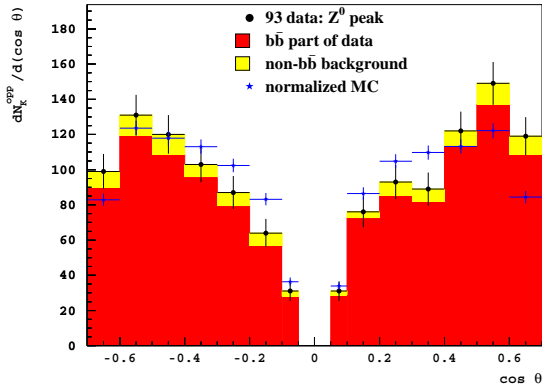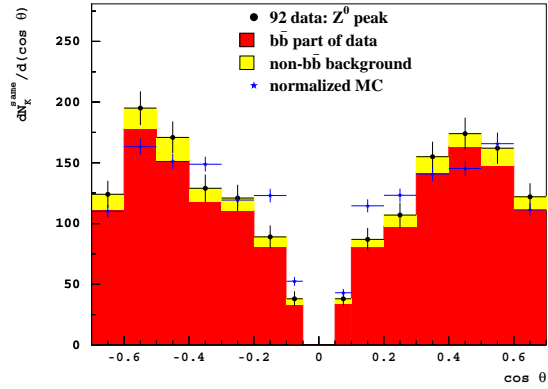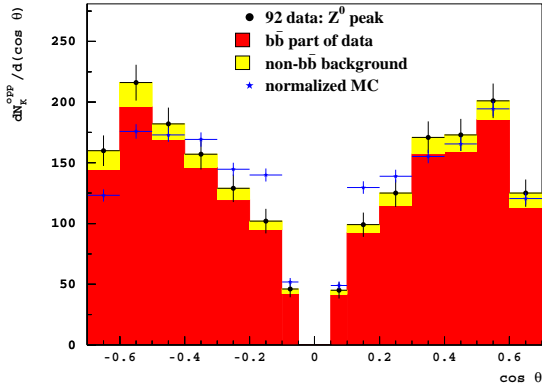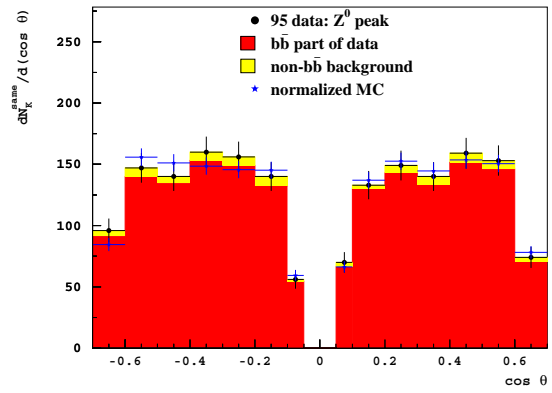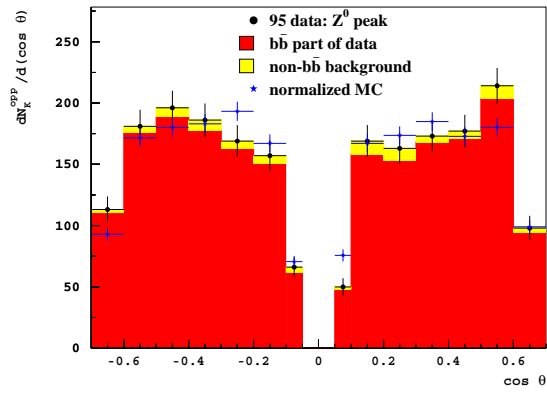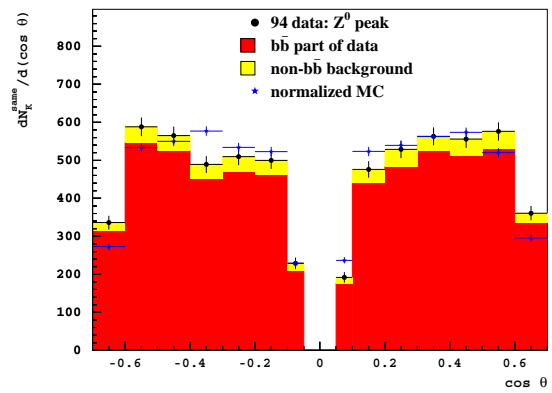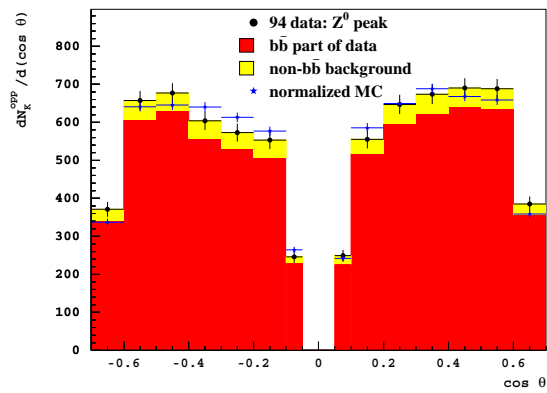
Data taken below the Z^0 **peak**
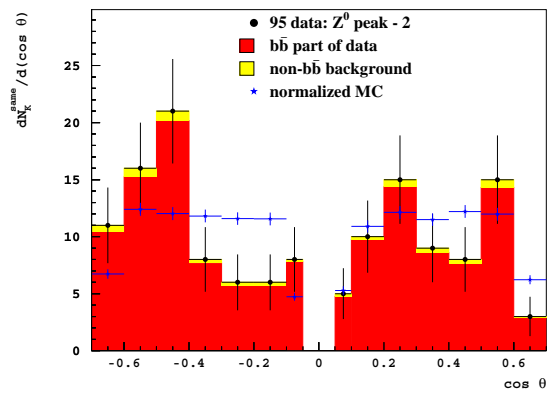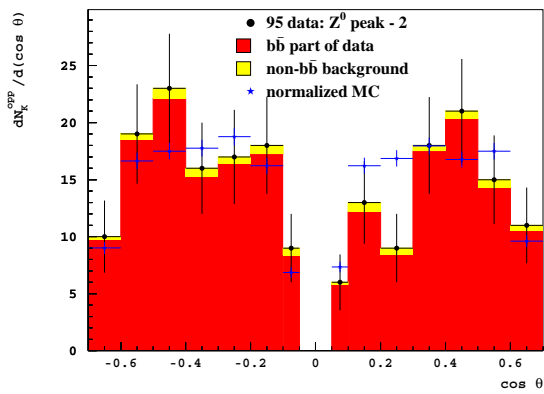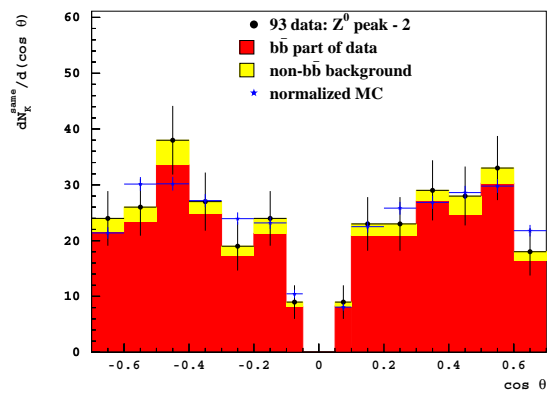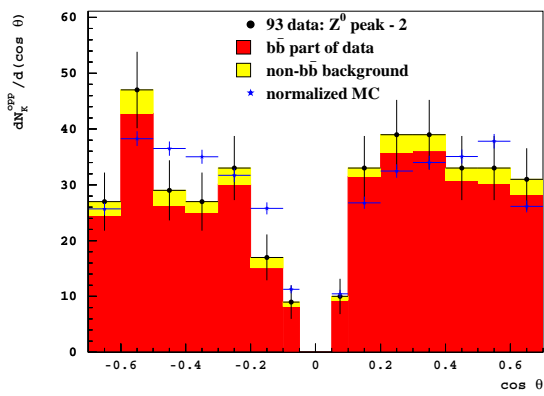
Data taken above the Z^0 peak
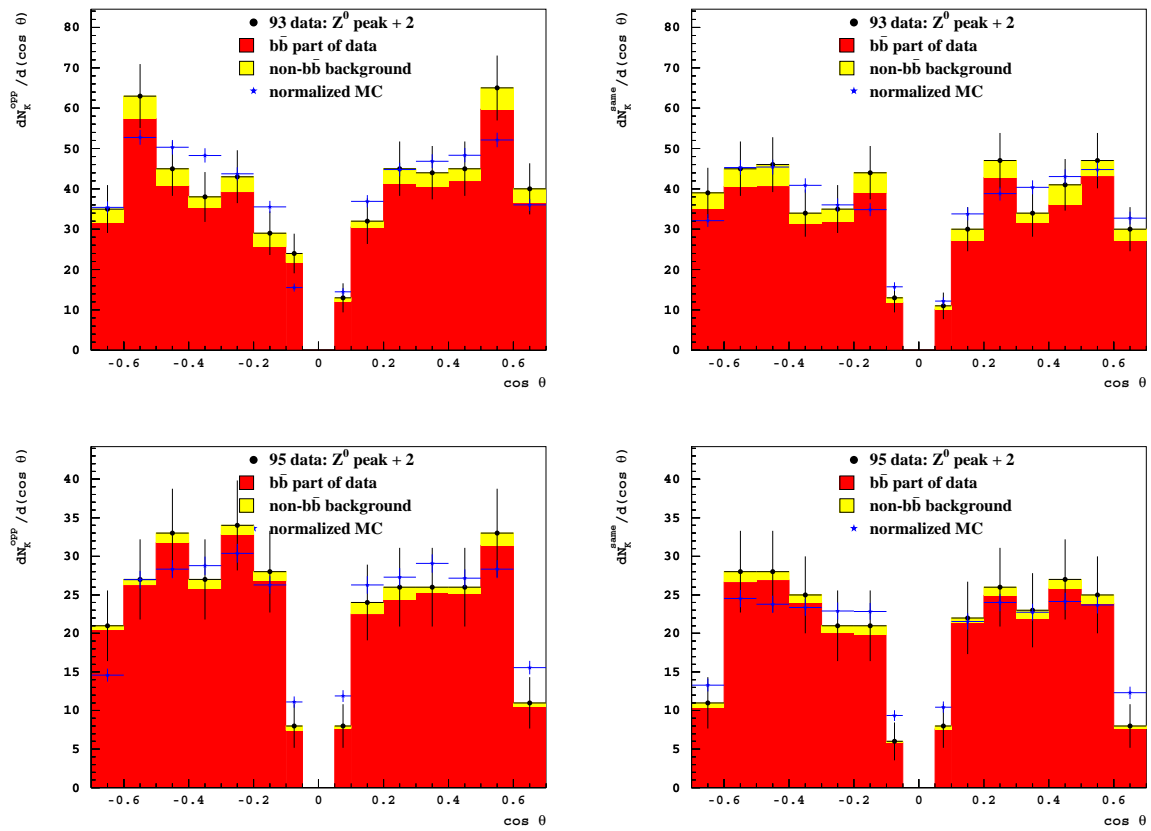
B.7 Dilution factors

Asymmetry of double-tagged events (5.5) for different measured data sets, shown together with the best fit function (5.6) and the extracted value of $\eta_{b,0}$ with its statistical error.

Data taken at the Z^0 peak
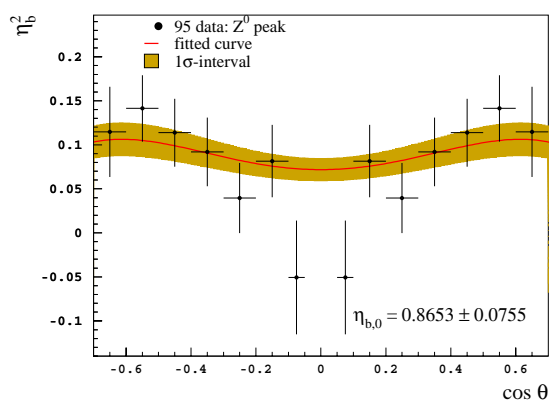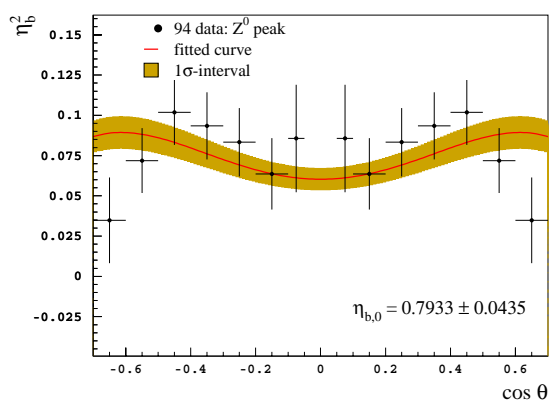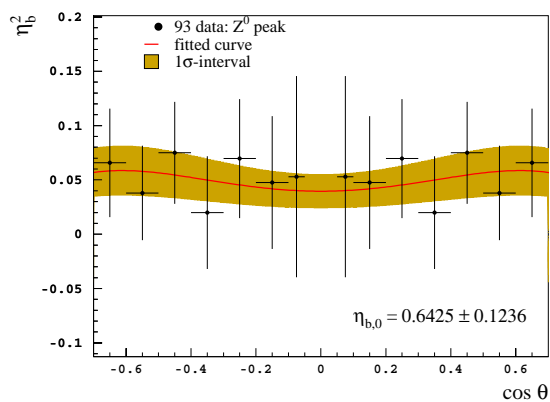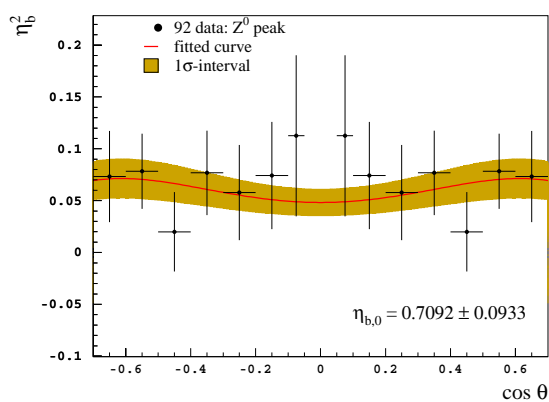
Data taken below the Z^0 peak
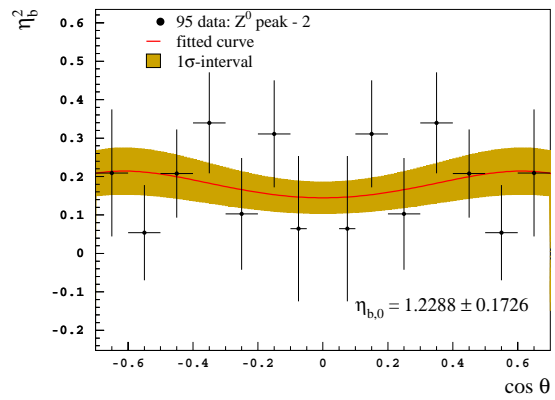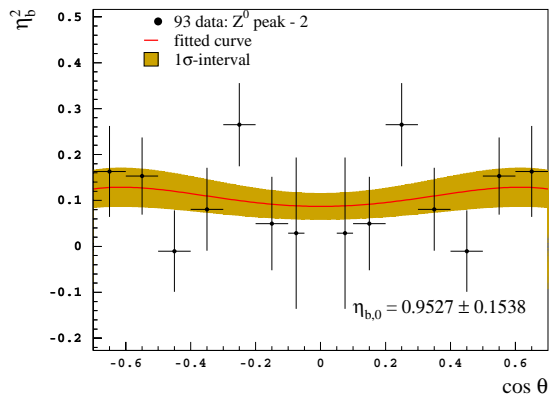
Data taken above the Z^0 peak
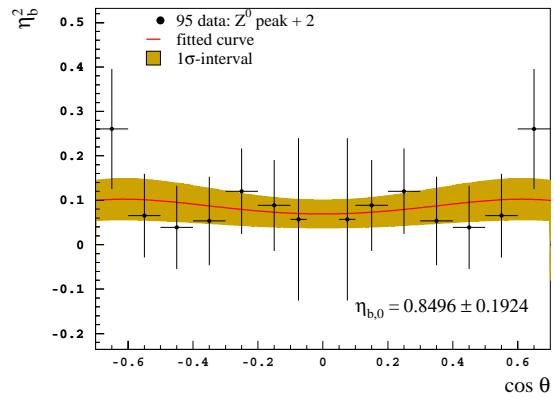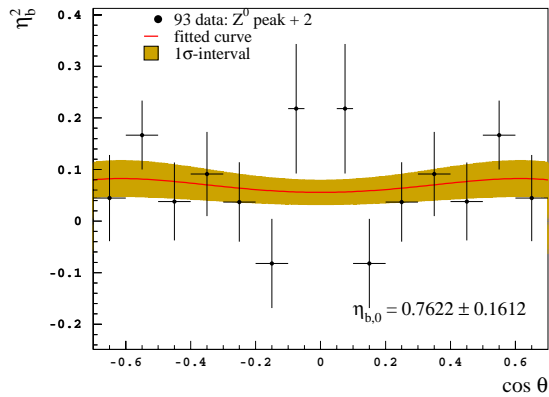
B.8   Fitted b-quark asymmetries

Forward-backward asymmetry for bottom quarks as measured for different years of data taking is shown together with the best fit function (5.7) obtained by the minimization of expression (5.8). Each figure is labeled by the extracted $A_{FB}^{b\bar{b}}$ and its statistical error. Note that only positive values of $\cos\theta$ were included in the fit.

Data taken at the Z^0 peak
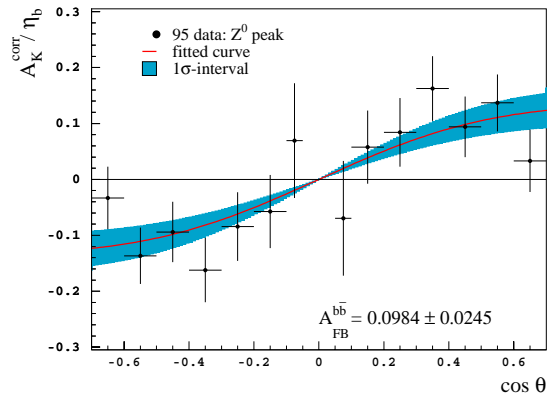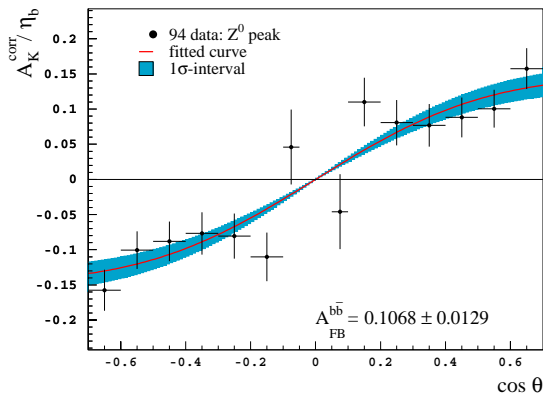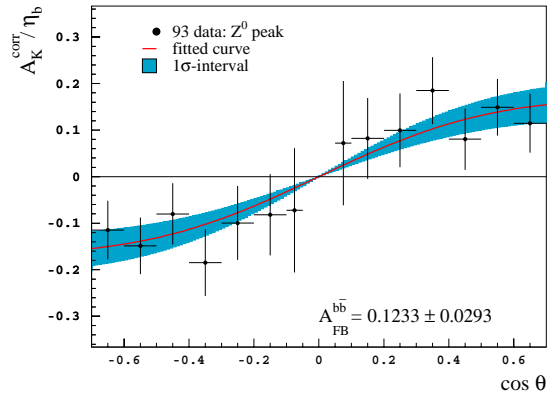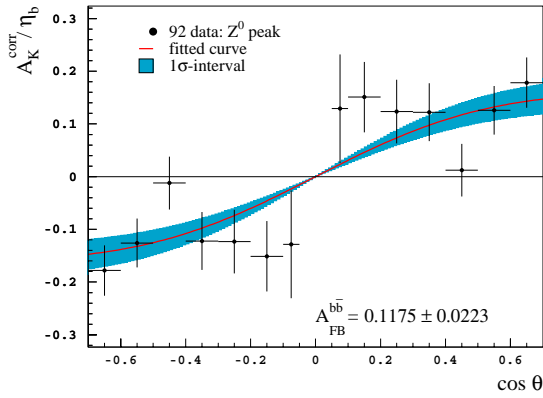
Data taken below the Z^0 peak
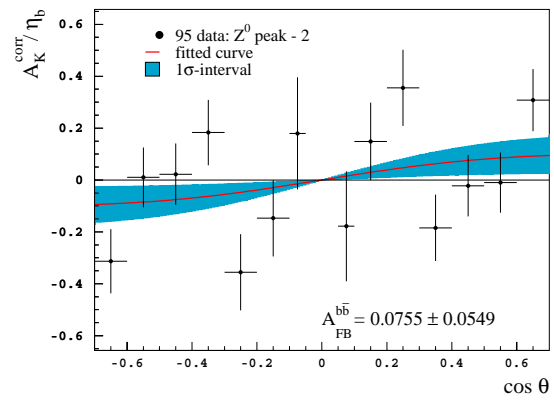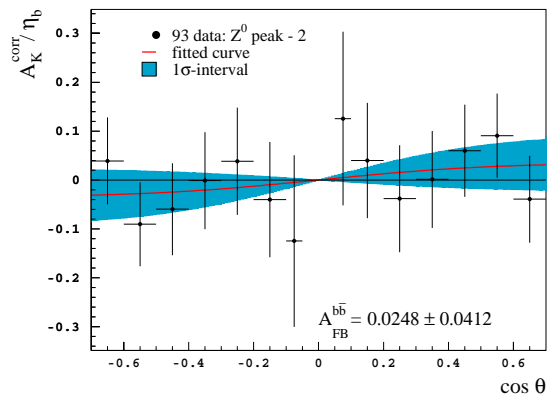
Data taken above the Z^0 peak
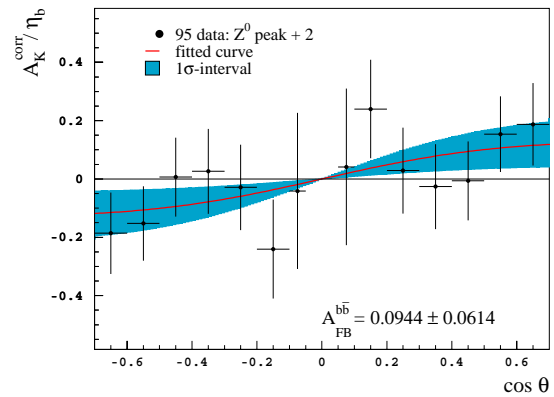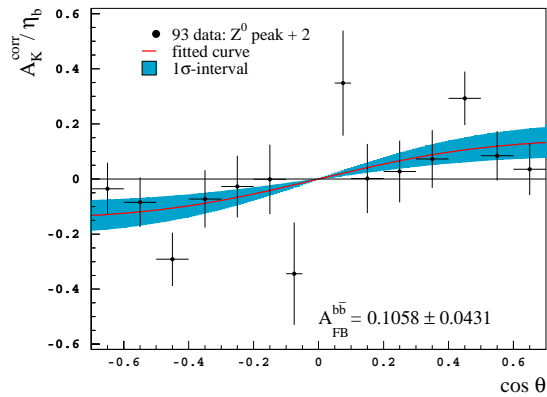
References

[1] S.L. Glashow, Nucl. Phys. **B 2** (1961) 579;
S. Weinberg, Phys. Rev. Lett. **19** (1967) 1264;
A. Salam, Proc. of the 8th Nobel Symp. at Lerum, Sweden, p. 367, Stockholm, 1968.

[2] S.L. Glashow, I. Iliopoulos, L. Maiani, Phys. Rev. **D 2** (1970) 1285.

[3] N. Cabibbo, Phys. Rev. Lett. **10** (1963) 531;
M. Kobayashi, K. Maskawa, Progr. Theor. Phys. **49** (1973) 652.

[4] C. S. Wu *et al.*, Phys. Rev. **105** (1956) 1413.

[5] The LEP Collaborations, the LEP Electroweak Working Group and the SLD Heavy Flavour and Electroweak Groups, *A Combination of Preliminary Electroweak Measurements and Constraints on the Standard Model*, prepared from Contributions of the LEP and SLD experiments to the 2000 Summer Conferences, to appear as CERN-EP Report in January 2001.

[6] G. 't Hooft, Nucl. Phys. **B 35** (1971) 167; G. 't Hooft, M. Veltman, Nucl. Phys. **B 44** (1972) 189.

[7] P. Higgs, Phys. Lett. **12** (1964) 132;
P. Higgs, Phys. Rev. Lett. **13** (1964) 508;
P. Higgs, Phys. Rev. **145** (1966) 1156.

[8] F. Halzen and A. D. Martin, *Quarks and Leptons*, John Wiley & Sons, 1984.

[9] E. Leader and E. Predazzi, *An Introduction to Gauge Theories and Modern Particle Physics*, Cambridge University Press, 1996.

[10] D. Bardin and G. Passarino, *The Standard Model in the Making: Precision Study of the Electroweak Interactions*, Oxford University Press, 1999.

[11] R.K. Ellis, J. Stirling and B.R. Webber, *QCD and Collider Physics*, Cambridge University Press, 1996.

[12] W. Greiner and A. Schäffer, *Quantum Chromodynamics*, Springer Verlag, 1995.

[13] D.E. Groom *et al.* (Particle Data Group), Eur. Phys. J. **C 15**, (2000) 1.

[14] B.P. Kerševan, *Measurement of Trilinear Gauge Boson* $\mathrm{W}^+\mathrm{W}^-\mathrm{Z}^0/\gamma$ *Couplings with the DELPHI Spectrometer*, doctoral thesis, University of Ljubljana, Ljubljana, 2000.

[15] M. Böhm and W. Hollik [conv.] *et al.*, *Forward-Backward Asymmetries* report in the Proc. Z *physics at LEP 1, Vol. 1*, edited by G.Altarelli, R. Kleiss and C. Verzegnassi, **CERN 89-08** (September 1989).

[16] D. Bardin, Proc. of the 1999 European School of High Energy Physics at Častá–Papiernička, Slovak Republic, **CERN 2000-007** (June 2000).

[17] D. Bardin *et al.*, Z. Phys **C 44** (1989) 493;
D. Bardin *et al.*, Comp. Phys. Comm. **59** (1990) 303;
D. Bardin *et al.*, Nucl. Phys. **B 351** (1991) 1;
D. Bardin *et al.*, Phys. Lett. **B 255** (1991) 290;
D. Bardin *et al.*, **CERN-TH 6443/92** (May 1992);
D. Bardin *et al.*, **DESY 99-070** (August 1999).

[18] S. Myers, *The LEP collider, from design to approval and commissioning*, **CERN 91-08** (October 1991).

[19] D. Brandt *et al.*, Rep. Prog. Phys. **63** (2000) 939.

[20] S. Jadach, *et al.*, Phys. Lett. **B 353** (1995) 362;
S. Jadach, *et al.*, Phys. Lett. **B 353** (1995) 349.

[21] G. Arduini *et al.*, *LEP1 operation, 1989-1995*, Proc. of the 5th European Particle Acceleration Conference (EPAC'96) at Sitges, Barcelona, Spain, p. 286., 1996.

[22] P. Aarnio *et al.* (DELPHI Collaboration), Nucl. Inst. and Meth. **A 303** (1991) 233.

[23] P. Abreu *et al.* (DELPHI Collaboration), Nucl. Inst. and Meth. **A 378** (1996) 57.

[24] N. Bingefors *et al.*, Nucl. Instr. Meth. **A 328** (1993) 447.

[25] Y. Sacquin, Nucl. Instr. Meth. **A 323** (1992) 209.

[26] E. G. Anassontzis *et al.*, Nucl. Instr. Meth. **A 323** (1992) 351.

[27] W. Adam *et al.*, Nucl. Instr. Meth. **A 338** (1994) 284.

[28] B. Eržen, *Measurement of the* $|V_{\mathrm{cs}}|$ *with the DELPHI Spectrometer*, doctoral thesis, University of Ljubljana, Ljubljana, 1999.

[29] V. Bocci *et al.*, *Architecture and Performance of the DELPHI Trigger System*, **CERN-PPE/94-141** (September 1994).

[30] DELPHI Collaboration, *DELPHI Data Analysis Program (DELANA) User's Guide*, **DELPHI 89-44** (May 1989).

[31] B. Golob and B. Eržen, *Offline Calibration of DELPHI Ring Imaging Cherenkov Detector Data*, **DELPHI 2000-008** (February 2000).

[32] P. Abreu *et al.*, *Delphi Event Generation and Detector Simulation User's guide*, **DELPHI 89-67** (September 1989).

[33] R. Kleiss and T. Sjöstrand [conv.] *et al.*, Proc. Z *physics at LEP 1, Vol. 3*, edited by G.Altarelli, R. Kleiss and C. Verzegnassi, **CERN 89-08** (September 1989).

[34] T. Sjöstrand, Comp. Phys. Comm. **82** (1994) 74.

[35] P. Abreu *et al.* (DELPHI Collaboration), Z. Phys. **C 73** (1996) 11.

[36] P. Abreu *et al.* (Delphi Collaboration), Nucl. Phys. **B 418** (1994) 403;
P. Abreu *et al.* (Delphi Collaboration), Eur. Phys. J. **C 16** (2000) 371.

[37] W. J. Murray, *Improved* B *tagging using Impact Parameters*, **DELPHI 95-167 PHYS 581** (November 1995).

[38] http://delphiwww.cern.ch/delfigs/export/pubdet4.html

[39] Z. Albrecht, M. Feindt and M. Moch, *MACRIB High efficiency - high purity hadron identification for DELPHI*, **DELPHI 99-150 RICH 95** (October 1999).

[40] M. Battaglia and P. M. Kluit, *Particle identification using the RICH detectors based on the RIBMEAN package*, **DELPHI 96-133 RICH 90** (September 1996).

[41] M. Feindt, C. Kreuter and O. Podobrin, *ELEPHANT Reference Manual*, **DELPHI 96-82 PROG 217** (June 1996).

[42] T. Allmendinger *et al.*, *BSAURUS – A Package For Inclusive* B-*Reconstruction in DELPHI*, **DELPHI 2000-069 PHYS 868** (June 2000).

[43] P. Abreu *et al.* (Delphi Collaboration), Eur. Phys. J. **C 14** (2000) 613.

[44] D. Abbaneo *et al.*, Eur. Phys. J. **C 4** 1998 185.

[45] P. Abreu *et al.* (DELPHI Collaboration), Eur. Phys. J. **C 10** (1999) 415.

[46] D. Buskulic *et al.* (Aleph Collaboration), Phys. Lett. **B 384** (1996) 414.

[47] P. Abreu *et al.* (Delphi Collaboration), Z. Phys. **C 65** (1995) 569; DELPHI Collaboration, *Masurement of the Forward-Backward Asymmetries of* $e^+e^- \to Z^0 \to b\overline{b}$ *and* $e^+e^- \to Z^0 \to c\overline{c}$ *using prompt leptons*, **DELPHI 2000-101 CONF 400**, contributed paper to ICHEP2000, Osaka.

[48] M. Acciarri *et al.* (L3 Collaboration), Phys. Lett. **B 448** (1999) 152.

[49] R. Barate *et al.* (Aleph Collaboration), Phys. Lett. **B 426** (1998) 217.

[50] P. Abreu *et al.* (Delphi Collaboration), Eur. Phys. J. **C 9** (1999) 367.

[51] M. Acciarri *et al.* (L3 Collaboration), Phys. Lett. **B 439** (1998) 225.

[52] K. Ackerstaff *et al.* (OPAL Collacoration), Z. Phys. **C 75** (1997) 385.

[53] P. Abreu *et al.* (Delphi Collaboration), Eur. Phys. J. **C 10** (1999) 219.

[54] G. Alexander *et al.* (Opal Collaboration), Z. Phys. **C 73** (1997) 379.

Izjavljam, da je disertacija nastala kot rezultat samostojnega raziskovalnega dela.

V Ljubljani, 22. decembra 2000   Marko Bračko